Astronomy Reports, Vol. 49, No. 3, 2005, pp. 167–178. Translated from Astronomicheskiĭ Zhurnal, Vol. 82, No. 3, 2005, pp. 195–206.

Sources of Radiation in the Early Universe: The Equation of Radiative Transfer and Optical Distances

D. I. Nagirner and S. L. Kirusheva

Sobolev Astronomical Institute, St. Petersburg State University, Bibliotechnaya pl. 2, Petrodvorets, 198904 Russia

Received May 15, 2004; in final form, September 20, 2004

Abstract—We have derived the radiative-transfer equation for a point source with a specified intensity and spectrum, originating in the early Universe between the epochs of annihilation and recombination, at redshifts $z_s = 10^8 - 10^4$. The direct radiation of the source is separated from the diffuse radiation it produces. Optical distances from the source for Thomson scattering and bremsstrahlung absorption at the maximum of the thermal background radiation are calculated as a function of the redshift z. The distances grow sharply with decreasing z, approaching asymptotic values, the absorption distance increasing more slowly and reaching their limiting values at lower z. For the adopted z values, the optical parameters of the Universe can be described in a flat model with dusty material and radiation, and radiative transfer can be treated in a grey approximation. © *2005 Pleiades Publishing, Inc.*

1. FORMULATION OF THE PROBLEM

Let the early Universe be described by the standard model, i.e. by the Friedmann equations (see, for example, [1]). Let us suppose that a source of radiation is switched on at some time between the epochs of annihilation and recombination, that this source has a specified geometry, spectrum, and total luminosity, and that it radiates during some time interval. The intensity and spectrum of the source may be time-dependent. Such sources could occur in a number of processes, for example, during the amplification or damping of fluctuations in the matter distribution, in the formation of primary black holes, etc.

The action of the source causes the thermodynamical equilibrium in its vicinity to be violated, since the source radiation is either nonequilibrium (for example, it has a power-law spectrum) or corresponds to a higher temperature. The radiation can experience bremsstrahlung absorption and Thomson scattering. In [2], it was suggested that such sources could affect the background radiation and hence be observed via perturbations of this background, contrary to the prevalent opinion that the energy of such sources is totally dissipated. Both possibilities require careful verification using the methods of radiative-transfer theory.

We assume that the source is pointlike. The point-source problem is also of independent interest: it is fundamental, since all other types of sources can be reduced to a set of point sources.

If the source radiation is intense, it affects the surrounding matter in several ways. First, the radiation creates an additional pressure, which affects the local expansion of space. Second, this same pressure gives rise to inhomogeneity of the expansion. Third, a shock and, in the case of a periodic source, matter oscillations may be formed. Fourth, the source can distort the metric of the surrounding space. In all these cases, the geometry of the source is the key factor.

Here, we will assume that the source radiation is moderately intense and does not affect the expansion of the surrounding space. To start with, we will present the model for the Universe at the considered epoch.

2. TWO-COMPONENT MODEL OF THE UNIVERSE: DUSTLIKE MATTER AND RADIATION

2.1. Basic Relations

We consider a model with a homogeneous and isotropic expanding Universe that contains equilibrium plasma and Planck radiation in the stage when the plasma is radiation-dominated; more exactly, between the epochs of annihilation ($z < 10^8$) and recombination ($z > 10^3$). In this stage of the evolution of the Universe, the cosmological term does not play a marked role.

At the temperatures corresponding to these redshifts, the matter can be assumed to be nonrelativistic, and the conditions of thermodynamical

balance with a common temperature for the matter and radiation are fulfilled [1]. The pressure of the matter may be neglected, i.e., the matter can be considered to be dustlike, in spite of its nearly total ionization.

Under these conditions, in the usual notation, the evolution of the expansion is described by the equation

$$\dot{R}^2 = \frac{8\pi G}{3}\rho_{\rm u}R^2 - kc^2, \qquad (1)$$

where a dot denotes a derivative with respect to the time t, the total mass density of the matter is equal to the sum of the matter and radiation densities, $\rho_{\rm u} = \rho_{\rm d} + \rho_{\rm r}$, and the parameter k assumes the values

$$k = \begin{cases} 1 & \text{for a closed model,} \\ 0 & \text{for a flat model,} \\ -1 & \text{for an open model.} \end{cases}$$

The matter density decreases in inverse proportion to the volume, while the expression for the radiation density contains another power of the radius of curvature in the denominator, resulting from the cosmological redshift:

$$\rho_{\rm d} = \rho_{\rm d}^0\frac{R_0^3}{R^3} = \frac{\rho_{\rm d}^0}{a^3}, \quad \rho_{\rm r} = \rho_{\rm r}^0\frac{R_0^4}{R^4} = \frac{\rho_{\rm r}^0}{a^4}.$$

Here and below, zero superscripts will denote cosmological values at the current epoch.

We will use the dimensionless time coordinate η and dimensionless radius of curvature (scale factor) $a(\eta)$:

$$R(t)d\eta = cdt, \quad a(\eta) = \frac{R(t)}{R_0}. \qquad (2)$$

With these variables, Eq. (1) can be transformed into

$$\left(\frac{da}{d\eta}\right)^2 = \frac{8\pi G}{3c^2}(\rho_{\rm d}^0 a + \rho_{\rm r}^0)R_0^2 - ka^2. \qquad (3)$$

This model was first considered by Chernin [3].

Let us also introduce the Hubble function and the critical density expressed in terms of this function:

$$H = \frac{\dot{R}}{R} = \frac{\dot{a}}{a} = \frac{c}{a}\frac{1}{R}\frac{da}{d\eta} = \frac{c}{R_0}\frac{a'(\eta)}{a^2(\eta)}, \quad \rho_{\rm c} = \frac{3H^2}{8\pi G}.$$

Along with the density itself, we will use the critical parameters

$$\Omega_{\rm d} = \frac{\rho_{\rm d}}{\rho_{\rm c}}, \quad \Omega_{\rm r} = \frac{\rho_{\rm r}}{\rho_{\rm c}}, \quad \Omega_{\rm u} = \Omega_{\rm d} + \Omega_{\rm r}, \qquad (4)$$

which can be used to rewrite (1) in another form:

$$R^2H^2(1 - \Omega_{\rm u}) = -kc^2. \qquad (5)$$

2.2. Auxiliary Functions

Let us define several mutually related functions, in terms of which the solutions and relations of the model will be written. The two main functions are $\mathrm{sn}_k(\eta)$ and $\mathrm{sc}_k(\eta)$, which are defined by the equalities

$$\mathrm{sn}_k(\eta) = \begin{cases} \sin\eta & \text{when } k = 1, \\ \eta & \text{when } k = 0, \\ \mathrm{sh}\,\eta & \text{when } k = -1, \end{cases} \qquad (6)$$

$$\mathrm{sc}_k(\eta) = \begin{cases} 1 - \cos\eta & \text{when } k = 1, \\ \eta^2/2 & \text{when } k = 0, \\ \mathrm{ch}\,\eta - 1 & \text{when } k = -1, \end{cases}$$

$$\mathrm{sc}_k'(\eta) = \mathrm{sn}_k(\eta).$$

Two functions are related to function (6). One of these,

$$\mathrm{cs}_k(\eta) = \mathrm{sn}'(\eta) = \begin{cases} \cos\eta & \text{when } k = 1, \\ 1 & \text{when } k = 0, \\ \mathrm{ch}\,\eta & \text{when } k = -1 \end{cases} \qquad (7)$$

is its derivative, while the other,

$$\mathrm{ar}_k(y) = \begin{cases} \arcsin y, & k = 1, \\ y, & k = 0, \\ \mathrm{arsh}\, y = \ln(y + \sqrt{1 + y^2}), & k = -1, \end{cases}$$

$$\frac{\mathrm{dar}_k(y)}{\mathrm{d}y} = \frac{1}{\sqrt{1 - ky^2}}$$

is the inverse of $\mathrm{sn}_k(\chi)$, i.e., $\mathrm{ar}_k(\mathrm{sn}_k(\eta)) = \eta$, $\mathrm{sn}_k(\mathrm{ar}_k(y)) = y$.

Another function,

$$\mathrm{cn}_k(\eta) = \begin{cases} \eta - \sin\eta & \text{when } k = 1, \\ \eta^3/6 & \text{when } k = 0, \\ \mathrm{sh}\,\eta - \eta & \text{when } k = -1, \end{cases}$$

is the integral of $\mathrm{sc}_k(\eta)$, i.e., $\mathrm{cn}_k'(\eta) = \mathrm{sc}_k(\eta)$.

It can easily be verified that the following relations between the introduced functions are satisfied:

$$\mathrm{cs}_k^2 + k\mathrm{sn}_k^2 = 1, \qquad (8)$$
$$\mathrm{sn}_k^2 + k\mathrm{sc}_k^2 = 2\mathrm{sc}_k, \quad \mathrm{cs}_k + k\mathrm{sc}_k = 1.$$

Let us consider the ratio

$$y(\eta) = \frac{\mathrm{sn}_k(\eta)}{\mathrm{sc}_k(\eta)} = \begin{cases} \cot\dfrac{\eta}{2} & \text{when } k = 1, \\ \dfrac{2}{\eta} & \text{when } k = 0, \\ \cot\dfrac{\eta}{2} & \text{when } k = -1. \end{cases} \qquad (9)$$

Its derivative with respect to η assumes a simple form if we use the relation between the derivatives and the functions and equalities (8):

$$y'(\eta) = \frac{\mathrm{sc}_k - k\mathrm{sc}_k^2 - 2\mathrm{sc}_k + k\mathrm{sc}_k^2}{\mathrm{sc}_k^2} = -\frac{1}{\mathrm{sc}_k}. \quad (10)$$

Using the second of the equalities, this ratio can, in turn, be expressed in terms of y:

$$\frac{dy}{d\eta} = -\frac{y^2 + k}{2}. \quad (11)$$

To obtain the correct solution, we must apply the appropriate initial condition: $y = \infty$ when $\eta = 0$. The arguments of the functions in relations (8), (10), and (11) have been omitted for brevity.

2.3. Solution of the Equation of Motion

It was shown in [3] that the solution of (3) in implicit form is

$$a(\eta) = a_\mathrm{r}\mathrm{sn}_k(\eta) + a_\mathrm{d}\mathrm{sc}_k(\eta), \quad (12)$$
$$t = \frac{R_0}{c}[a_\mathrm{r}\mathrm{sc}_k(\eta) + a_\mathrm{d}\mathrm{cn}_k(\eta)].$$

Indeed, we can easily verify using relations (8) that the function $a(\eta)$ satisfies (3) if we assume

$$a_\mathrm{r} = \sqrt{\frac{8\pi G}{3}\rho_\mathrm{r}^0}\frac{R_0}{c}, \quad a_\mathrm{d} = \frac{4\pi G}{3c^2}\rho_\mathrm{d}^0 R_0^2.$$

The obtained coefficients are expressed in terms of the critical parameters. Let us first derive an expression for the current radius of curvature [1]. To this end, we apply formula (5) to the current epoch:

$$H_0^2 R_0^2 = -\frac{kc^2}{1-\Omega_\mathrm{u}^0}, \quad \frac{H_0 R_0}{c} = \frac{1}{\sqrt{|1-\Omega_\mathrm{u}^0|}}.$$

We now have, in accordance with the definitions (4),

$$a_\mathrm{d} = \frac{4\pi G}{3c^2}\rho_\mathrm{c}^0\Omega_\mathrm{d}^0 R_0^2 = \frac{4\pi G}{3c^2}\frac{3H_0^2}{8\pi G}\Omega_\mathrm{d}^0 R_0^2$$
$$= -\frac{k}{2}\frac{\Omega_\mathrm{d}^0}{1-\Omega_\mathrm{u}^0} = \frac{\Omega_\mathrm{d}^0}{2|1-\Omega_\mathrm{u}^0|},$$
$$a_\mathrm{r}^2 = \frac{8\pi G}{3c^2}\rho_\mathrm{c}^0\Omega_\mathrm{r}^0 R_0^2 = \frac{8\pi G}{3c^2}\frac{3H_0^2}{8\pi G}\Omega_\mathrm{d}^0 R_0^2$$
$$= -\frac{k\Omega_\mathrm{r}^0}{1-\Omega_\mathrm{u}^0} = \frac{\Omega_\mathrm{r}^0}{|1-\Omega_\mathrm{u}^0|}.$$

The inverse formulas have the form:

$$\Omega_\mathrm{d}^0 = \frac{2a_\mathrm{d}}{2a_\mathrm{d} + a_\mathrm{r}^2 - k}, \quad \Omega_\mathrm{r}^0 = \frac{a_\mathrm{r}^2}{2a_\mathrm{d} + a_\mathrm{r}^2 - k},$$
$$\Omega_\mathrm{u}^0 = \frac{2a_\mathrm{d} + a_\mathrm{r}^2}{2a_\mathrm{d} + a_\mathrm{r}^2 - k}.$$

In the following subsections (to Subsection 9), we will assume that $k \neq 0$, although some functions are calculated using formulas that include the special case of a flat space.

2.4. Relation to the Redshift

Let us derive expressions for the quantities associated with the solution (12) in terms of the redshift z. By definition $a(\eta) = \frac{R(\eta)}{R_0} = \frac{1}{1+z}$. Successively substituting in (12) the expression for sn_k or sc_k in terms of the other, and also using the last relation in (8), we obtain

$$\mathrm{sn}_k(\eta) = \frac{Q - B(1-kA)}{1+kB^2},$$
$$\mathrm{sc}_k(\eta) = \frac{B^2 + A - BQ}{1+kB^2},$$
$$\mathrm{cs}_k(\eta) = \frac{1 - kA + kBQ}{1+kB^2}.$$

Here, we have introduced the notation

$$A = \frac{1}{a_\mathrm{d}}\frac{1}{1+z} = \frac{2|1-\Omega_\mathrm{u}^0|}{\Omega_\mathrm{d}^0}\frac{1}{1+z}, \quad (13)$$
$$B = \frac{a_\mathrm{r}}{a_\mathrm{d}} = \frac{2\sqrt{\Omega_\mathrm{r}^0|1-\Omega_\mathrm{u}^0|}}{\Omega_\mathrm{d}^0},$$
$$Q = \sqrt{B^2 + 2A - kA^2}.$$

The derivative $a'(\eta)$ and the Hubble function can be expressed in terms of the redshift in this same way:

$$a'(\eta) = a_\mathrm{r}\mathrm{cs}_k(\eta) + a_\mathrm{d}\mathrm{sc}_k(\eta),$$
$$\frac{H}{H_0} = \frac{c}{H_0 R_0}\frac{a'(\eta)}{a^2(\eta)} = \frac{a'(\eta)}{a^2(\eta)}\sqrt{|1-\Omega_\mathrm{u}^0|}.$$

The ratio (9) and the product of this ratio with B can also be expressed in terms of z:

$$y(\eta) = \frac{kAB - B + Q}{B^2 + A - BQ},$$
$$X = By = \frac{kAB - B + Q}{B + A/B - Q}.$$

The critical parameters at the current epoch (B is constant) can likewise be expressed in terms of the quantities in (14):

$$\Omega_\mathrm{d}^0 = \frac{2A_0}{Q_0^2}, \quad \Omega_\mathrm{r}^0 = \frac{B^2}{Q_0^2},$$
$$\Omega_\mathrm{u}^0 = \frac{2A_0 + B^2}{Q_0^2}, \quad 1 - \Omega_\mathrm{u}^0 = -k\frac{A_0^2}{Q_0^2}.$$

It is easy to verify that the identities $a(\eta_0) = 1$ and $a'(\eta_0) = H_0 R_0/c = 1/\sqrt{|1-\Omega_\mathrm{u}^0|}$ are satisfied.

2.5. Specific Models

According to the above model, the curvature of space can be arbitrary (constant). However, recent observations lead to the conclusion that space was flat over the entire history of the Universe. In this context, we will consider two specific models. One is open, close to flat, and does not take into account the vacuum component (we will call this the nonvacuum model), while the other has three components and is strictly flat, but with the vacuum neglected at $z > 10^3$.

We will adopt for the Hubble constant $H_0 = 65\ \mathrm{km\,s^{-1}Mpc^{-1}}$, the corresponding critical density $\rho_c^0 = 7.940 \times 10^{-30}\ \mathrm{g/cm^3}$, and the critical parameters for the baryon component $\Omega_b^0 = 0.025$ and dustlike component $\Omega_d^0 = 0.25$. The baryon density is then $\rho_b^0 = 4.684 \times 10^{-31}\ \mathrm{g/cm^3}$, the density of dustlike matter is $\rho_d^0 = 4.684 \times 10^{-30}\ \mathrm{g/cm^3}$, the mass density of the radiation corresponding to the temperature $T_0 = 2.7277$ K is $\rho_r^0 = 4.63 \times 10^{-34}\ \mathrm{g/cm^3}$, and $\Omega_r^0 = 5.83 \times 10^{-5}$.

2.5.1. Nonvacuum model. For the adopted model parameters, $1 - \Omega_u^0 = 1 - \Omega_d^0 - \Omega_r^0 = 0.7499$; i.e., this model is open ($k = -1$), which is natural, since there is no vacuum component. The other parameters are $a_r = 8.869 \times 10^{-3}$ and $a_d = 0.1667$.

2.5.2. Strictly flat model. For $k = 0$, we also have $1 - \Omega_u = 0$, so that many of the introduced values become equal to zero or infinity. In this case, the limit transition is complicated, and it is easier to consider this case individually.

We will assume that the most plausible model of the Universe for redshifts less than 10–100, in particular for the current epoch, is a flat model with three noninteracting components: dustlike matter, radiation, and the vacuum. Based on this model, we will also construct a two-component flat model for the considered epoch of radiation-dominated plasma in which the two components have the same densities, but there is no vacuum component. All values corresponding to this model will be denoted by a tilda.

The contribution of the vacuum can be neglected for the redshifts considered ($10^3 \le z \le 10^8$), so that the Hubble functions in the two-component and three-component flat models differ only slightly:

$$H = \sqrt{\frac{8\pi G}{3}}\sqrt{\rho_d^0(1+z)^3 + \rho_r^0(1+z)^4 + \rho_\Lambda},$$

$$\widetilde{H} = \sqrt{\frac{8\pi G}{3}}\sqrt{\rho_d^0(1+z)^3 + \rho_r^0(1+z)^4}.$$

We will use the same critical parameters Ω_d^0 and Ω_r^0 as above; the critical parameter for the vacuum is then $\Omega_\Lambda^0 = 1 - \Omega_d^0 - \Omega_r^0$. In the adopted model, these values are:

$$\widetilde{H}_0 = H_0\sqrt{\frac{\rho_d^0 + \rho_r^0}{\rho_d^0 + \rho_r^0 + \rho_\Lambda^0}} = H_0\sqrt{1 - \Omega_\Lambda^0}, \quad (14a)$$

$$\tilde{\rho}_c^0 = \rho_c^0(1 - \Omega_\Lambda^0), \quad (14b)$$

$$\widetilde{\Omega}_d^0\frac{\Omega_d^0}{1 - \Omega_\Lambda^0}, \tilde{\Omega}_r^0 = \frac{\Omega_r^0}{1 - \Omega_\Lambda^0}. \quad (14c)$$

For brevity, let us set $\widetilde{\Omega}_d = \Omega$, in which case $\widetilde{\Omega}_r = 1 - \Omega$, so that $\widetilde{\Omega}_d^0 = \Omega_0$ and $\widetilde{\Omega}_r^0 = 1 - \Omega_0$.

The radius of curvature R and its current value R_0 are meaningless in a flat Universe (they are infinite, and can be selected arbitrarily in the formulas), and should not arise in expressions for physical values. Indeed, the solution (12) can be written in the form

$$a(\eta) = a_r\eta + a_d\frac{\eta^2}{2} = \sqrt{1 - \Omega_0}\frac{\widetilde{H}_0 R_0}{c}\eta$$

$$+ \Omega_0\frac{\widetilde{H}_0^2 R_0^2}{4c^2}\eta^2 = 2\sqrt{1 - \Omega_0}\zeta + \Omega_0\zeta^2,$$

where we have introduced a new time variable that is linearly related to the previous time variable and is expressed in terms of $a(\eta)$ and the redshift:

$$\zeta = \frac{\widetilde{H}_0 R_0}{2c}\eta = \frac{a}{\sqrt{1 - \Omega_0(1-a)} + \sqrt{1 - \Omega_0}}$$

$$= \frac{1}{\sqrt{1+z}\left(\sqrt{1 + (1-\Omega_0)z} + \sqrt{(1-\Omega_0)(1+z)}\right)}.$$

3. RADIATIVE-TRANSFER EQUATION IN THE EARLY UNIVERSE

3.1. General Form of the Radiative-Transfer Equation for a Point Source

Let us assume the source to be pointlike and isotropic. In this case, the problem is spherically symmetrical, so that, generally speaking, the approach of the Tolman–Bondi model should be used. However, to first approximation, we can assume that the source radiation does not affect the metric of space and its expansion, and the evolution of the source radiation can be considered against the background of the standard cosmological two-component model described in Section 2.

We will describe the radiation with the mean occupation number of photon states n, rather then the intensity. The advantage of this quantity is that it is dimensionless and relativistically invariant (scalar). Due to the symmetry of our problem, the mean occupation number of photon states will depend on the

time t or time variable η, the distance of the point considered from the coordinate origin (described by the parameter χ), the angle θ between the radial direction and the ray along which the radiation propagates, and the dimensionless frequency x: $n = n(\eta, \chi, \theta, x)$.

The radiative-transfer equation has the form

$$\frac{dn}{dt} = \frac{\partial n}{\partial t} + \frac{\partial n}{\partial x}\frac{dx}{dt} + \frac{\partial n}{\partial \chi}\frac{d\chi}{dt} + \frac{\partial n}{\partial \theta}\frac{d\theta}{dt} = c\mathcal{I}_c, \quad (15)$$

where $\mathcal{I}_c$ is the collision integral, i.e., the difference between the numbers of photons with specified parameters entering and leaving the state.

We will use the parameter η instead of the time; the derivatives will be calculated with respect to η using relation (2), so that

$$\frac{\partial}{\partial t} = \frac{c}{R(\eta)}\frac{\partial}{\partial \eta}.$$

The derivative of the frequency with respect to the time is the easiest to find. Due to the redshift,

$$\nu = \nu_0\frac{R_0}{R}, \quad x = \frac{\nu}{\nu_\star} = \frac{\nu_0}{\nu_\star}\frac{R_0}{R} = x_0\frac{R_0}{R},$$
$$\frac{dx}{dt} = -x_0R_0\frac{\dot{R}}{R^2} = -xH,$$

where $H = \dfrac{\dot{R}}{R}$ is the Hubble function and $\nu_\star$ is some specified frequency.

To determine the other derivatives, we must analyze the variations of the corresponding values along the ray.

3.2. Left-hand Side of the Transfer Equation

Let us consider the ray along which the radiation propagates, having, in general, already been scattered. An arbitrary ray can be described using several parameters, one of which can be chosen to be the coordinates of the point on the ray closest to a point source at the coordinate origin. We will call this the initial point. Due to the symmetry of the problem, it is sufficient to specify this distance using the coordinate χ_0. Let a photon pass through the initial point at time $t_0 = t(\eta_0)$. Its position on the ray will be described by the parameter χ_* associated with this time and measured from time t_0. Let us determine the derivatives with respect to χ_* of the variables describing the position of the photon on the ray.

To this end, let us consider the curvilinear triangle presented in Fig. 1, with its sides extending from the source S to the initial point, from the source to the photon at time η, and from the initial point to the photon. Since all the lengths are proportional to the radius of curvature, we will consider dimensionless distances described by the coordinates χ_0, χ, and χ_*, respectively; the corresponding dimensionless lengths are $a_0 = \mathrm{sn}_k(\chi_0), \mathrm{sn}_k(\chi)$, and $\mathrm{sn}_k(\chi_*)$. In the same order, the angles opposing these sides are those between the ray and radial direction, θ, between the radial direction toward the initial point and the ray (a right angle), and between the radial direction toward the initial point and the direction toward the photon's position, θ_*.

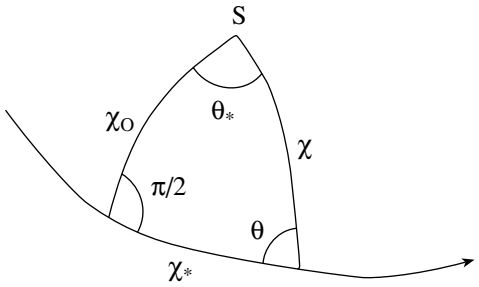

Fig. 1. The curvilinear triangle.

We can write the geometrical integrals of the transfer equation for the constructed right-angle curvilinear triangle:

$$a_0 = \mathrm{sn}_k(\chi_0) = \mathrm{sn}_k(\chi)\sin\theta, \quad (16a)$$
$$\frac{\mathrm{sn}_k(\chi_0)}{\mathrm{cs}_k(\chi_0)} = \mathrm{sn}_k(\chi_*)\tan\theta, \quad (16b)$$
$$r_0 = \mathrm{cs}_k(\chi_0) = \frac{\mathrm{sn}_k(\chi)}{\mathrm{sn}_k(\chi_*)}\cos\theta = \frac{\cos\theta}{\sin\theta_*}, \quad (16c)$$

$$\mathrm{cs}_k(\chi) = r_0\mathrm{cs}_k(\chi_*), \quad \frac{\mathrm{sn}_k(\chi)}{\mathrm{cs}_k(\chi)}\cos\theta = \frac{\mathrm{sn}_k(\chi_*)}{\mathrm{cs}_k(\chi_*)},$$
$$\cos\theta_* = \mathrm{cs}_k(\chi_*)\sin\theta.$$

The functions sn_k and cs_k are specified by equalities (6) and (7). Relation (16c) follows from the two preceding expressions (16a) and (16b). These relations are trivial in the case of a flat space. For a space with positive curvature, the triangle can be placed on a unit sphere in three-dimensional space, with the subsequent use of spherical geometry. To make the translation to the case of negative curvature, the trigonometric functions expressing the sides of the triangle must be changed to hyperbolic functions.

The following derivatives can easily be obtained from these relations:

$$\frac{d\chi}{d\chi_*} = \cos\theta, \quad (17a)$$
$$\frac{d\theta}{d\chi_*} = -\sin\theta\frac{\mathrm{cs}_k(\chi)}{\mathrm{sn}_k(\chi)}, \quad (17b)$$
$$\frac{d\theta_*}{d\chi_*} = \frac{\sin\theta}{\mathrm{sn}_k(\chi)}. \quad (17c)$$

The equation of motion of a photon along a ray is $\chi_* = \eta - \eta_0$, so that the derivatives (17a), (17b), and (17c) are simultaneously the derivatives with respect to the time coordinate η.

Thus, the transfer equation (15) takes the form

$$\frac{c}{R(\eta)}\left[\frac{\partial n}{\partial \eta} + \cos\theta\frac{\partial n}{\partial \chi} - \sin\theta\frac{\mathrm{cs}_k(\chi)}{\mathrm{sn}_k(\chi)}\frac{\partial n}{\partial \theta}\right] - xH\frac{\partial n}{\partial x} = c\mathcal{I}_\mathrm{c}. \quad (18)$$

For a flat space, when $k = 0$, $\mathrm{sn}_0(\chi) = \chi$, and $\mathrm{cs}_0(\chi) = 1$, the equation takes the usual form.

3.3. Right-hand Side of the Transfer Equation

In the problem we are considering, bremsstrahlung absorption and emission, as well as Thomson scattering, are important processes in the interaction between the matter and point-source radiation.

Bremsstrahlung absorption by thermal nonrelativistic electrons with a Maxwellian velocity distribution and the temperature T is described by the formula [4]

$$\alpha^*_\mathrm{cc} = n_\mathrm{e}n^+k_\mathrm{cc}(\nu, T), \quad \alpha_\mathrm{cc} = (1 - e^{-h\nu/k_\mathrm{B}T})\alpha^*_\mathrm{cc},$$

where the cross section is

$$k_\mathrm{cc}(\nu, T) = \frac{k^0_\mathrm{cc}}{T^{1/2}\nu^3},$$

$$k^0_\mathrm{cc} = 8\pi\frac{e^6}{c\hbar}\frac{k_\mathrm{B}}{(6\pi m k_\mathrm{B})^{3/2}} = 3.69\times10^8\ \mathrm{cm}^5\ \mathrm{K}^{1/2}\ \mathrm{s}^{-3}.$$

The absorption coefficient has been corrected for stimulated emission. The Gaunt factor is taken to be unity. The bremsstrahlung coefficient in the occupation numbers is related to the absorption coefficient by the Kirchhoff–Planck relation:

$$\epsilon_\mathrm{cc} = \alpha_\mathrm{cc}e^{-h\nu/k_\mathrm{B}T}. \quad (19)$$

The absorption coefficient associated with Thomson scattering is $\alpha_T = n_\mathrm{e}\sigma_T$, where the cross section is $\sigma_T = \frac{8\pi}{3}\left(\frac{e^2}{mc^2}\right)^2 = 6.66\times10^{-25}\ \mathrm{cm}^2$. The indicatrix for Thomson scattering is the Rayleigh index. Since the radiation field does not depend on the azimuth, the equation will contain the azimuth-averaged indicatrix

$$p(\theta, \theta') = 1 + \frac{1}{2}P_2(\cos\theta)P_2(\cos\theta'),$$

where $P_2(\mu)$ is the second Legendre polynomial.

Thus, the right-hand side of the transfer equation has the form

$$\mathcal{I}_\mathrm{c} = -[\alpha_\mathrm{cc}(\nu, T) + \alpha_T]n(\eta, \chi, \theta, x) + \epsilon_\mathrm{cc}(\nu, T) + \alpha_T\overline{I} + \epsilon_*(\eta, \chi, \theta, x), \quad (20)$$

$$\overline{I} = \frac{1}{2}\int_0^\pi \sin\theta' p(\theta, \theta')d\theta' n(\eta, \chi, \theta', x),$$

where ϵ_* describes the primary radiation from the point source.

The integral in (20) can be divided into two terms containing two angular moments $n(\eta, \chi, \theta, x)$:

$$n_0(\eta, \chi, x) = \frac{1}{2}\int_0^\pi \sin\theta' d\theta' n(\eta, \chi, \theta', x),$$

$$n_2(\eta, \chi, x) = \frac{5}{2}\int_0^\pi \sin\theta' P_2(\cos\theta')d\theta' n(\eta, \chi, \theta', x).$$

Let us now specify the source function ϵ_* and separate the direct from the diffuse radiation.

3.4. Direct Radiation

The entire space is filled by homogeneous and isotropic equilibrium cosmological radiation with the mean occupation number

$$n_\mathrm{e}(\eta, x) = \frac{1}{e^{h\nu_\star x/k_\mathrm{B}T} - 1} = \frac{1}{e^{h\nu_\star x_0/k_\mathrm{B}T_0} - 1}. \quad (21)$$

It is straightforward to verify that this function satisfies (18) with the right-hand side (20) without the last term. In fact, both the left-hand and right-hand sides vanish, the left-hand side because the mean occupation number for the background radiation does not depend on anything, and the right-hand side due to the Kirchhoff–Planck relation (19). This is the equilibrium background radiation. In spite of the fact that it interacts with matter, overall, the matter and radiation do not affect one another during this interaction; only a common temperature is established. After the epoch of recombination, the electron density becomes extremely small (it can be assumed to be zero), and the right-hand side of the transfer equation no longer contains terms describing the interaction between radiation and matter (the radiation is separated from the matter), while the left-hand side corresponds to the free propagation of the radiation. The quantity (21) remains constant and satisfies the transfer equation.

Let us now consider the direct radiation of the source. We will first find an expression for ϵ_*. The relation between the total energy L emitted by the

source (for all time, in all space, in all directions and frequencies) and ϵ_* is

$$L = \frac{2h\nu_\star^4}{c^2}\int\limits_0^\infty dt \int d^3r \int\limits_0^\infty x^3 dx \epsilon_*(\eta,\chi,\theta,x).$$

The factor before the integrals is introduced to translate the occupation number into intensity. Expressing time in terms of η and writing the integral over space in terms of integrals over the three variables, taking into account the volume element $d^3r = R^3(\eta)\mathrm{sn}_k^2(\chi)\sin\theta d\chi d\theta d\varphi$, we obtain

$$L = 2\pi\frac{2h\nu_\star^4}{c^3}\int\limits_0^\infty R^4(\eta)d\eta\int\limits_0^\infty \mathrm{sn}_k^2(\chi)d\chi \qquad (22)$$
$$\times\int\limits_0^\pi \sin\theta d\theta\int\limits_0^\infty x^3 dx\epsilon_*(\eta,\chi,\theta,x).$$

It follows from the expression for the right-hand side of the transfer equation (20) that the units of ϵ_* are inverse length.

If the power of the source radiation at the time t_s with the time coordinate η_s at frequency x_s is $L\delta(t-t_\mathrm{s})$, we can write

$$\epsilon_*(\eta,\chi,\theta,x) = L\frac{c^3}{2h\nu_\star^4}\frac{\delta(\eta-\eta_\mathrm{s})}{R^4(\eta_\mathrm{s})}\frac{\delta(\chi)}{\mathrm{sn}_k^2(\chi)}$$
$$\times\frac{\delta(\cos\theta-1)}{2\pi}\frac{\delta(x-x_\mathrm{s})}{x_\mathrm{s}^3},$$

and relation (22) is satisfied.

Further, let us determine the mean occupation number for the direct radiation from the source. It is specified by the transfer equation (18) with the right-hand side (20) without any terms describing scattering:

$$\left[\frac{\partial}{\partial\eta}+\cos\theta\frac{\partial}{\partial\chi}-\sin\theta\frac{\mathrm{cs}_k(\chi)}{\mathrm{sn}_k(\chi)}\frac{\partial}{\partial\theta}\right.$$
$$\left.-x\frac{a'(\eta)}{a(\eta)}\frac{\partial}{\partial x}\right]n_*(\eta,\chi,\theta,x)$$
$$= -[n^+k_\mathrm{cc}(\nu,T)+\sigma_T]n_\mathrm{e}R(\eta)n_*(\eta,\chi,\theta,x)$$
$$+\epsilon_*(\eta,\chi,\theta,x)R(\eta).$$

Direct substitution verifies that the solution of this equation is given by the function

$$n_*(\eta,\chi,\theta,x) = L\frac{c^3}{2h\nu_\star^4}\frac{\delta(\chi-\eta+\eta_\mathrm{s})}{R^3(\eta_\mathrm{s})}\frac{\Theta(\chi)}{\mathrm{sn}_k^2(\chi)}$$
$$\times\frac{\delta(xa(\eta)/a(\eta_\mathrm{s})-x_\mathrm{s})}{x_\mathrm{s}^3}\frac{\delta(\cos\theta-1)}{2\pi}e^{-\tau},$$

where the optical distance from the source to the point is (see below)

$$\tau = \tau(\eta,\eta-\eta_\mathrm{s},x_\mathrm{s}a(\eta_\mathrm{s})/a(\eta)) = \tau_T(\eta)-\tau_T(\eta_\mathrm{s})$$
$$+\left(1-e^{-h\nu_\star x_\mathrm{s}/k_\mathrm{B}T_\mathrm{s}}\right)R_0\frac{k_\mathrm{cc}^0[E(\eta)-E(\eta_\mathrm{s})]}{\nu_\star^3x_\mathrm{s}^3T_\mathrm{s}^{1/2}a^{7/2}(\eta_\mathrm{s})}.$$

3.5. Discriminating between Direct and Diffuse Radiation

Let us represent the total occupation number for the photon states created by the source as the sum of two terms:

$$n(\eta,\chi,\theta,x) = n_*(\eta,\chi,\theta,x)+n_\mathrm{d}(\eta,\chi,\theta,x),$$

where n_d describes the diffuse part of the radiation. This function satisfies the same transfer equation (18) as the initial function, but with the "source" term ϵ_* replaced by $\epsilon_\mathrm{s}(\eta,\chi,\theta,x)$—the part of the emission coefficient due to scattering of the direct radiation from the point source. This quantity is specified by the formula

$$\epsilon_\mathrm{s}(\eta,\chi,\theta,x) = \alpha_T\left[1+\frac{1}{2}P_2(\cos\theta)\right]n_0^*(\eta,\chi,x),$$

where the zeroth moment of the direct intensity is

$$n_0^*(\eta,\chi,x) = \frac{L}{4\pi}\frac{c^3}{2h\nu_\star^4}\frac{\delta(\chi-\eta+\eta_\mathrm{s})}{R^3(\eta_\mathrm{s})}\frac{\Theta(\chi)}{\mathrm{sn}_k^2(\chi)}$$
$$\times\frac{\delta(xa(\eta)/a(\eta_\mathrm{s})-x_\mathrm{s})}{x_\mathrm{s}^3}e^{-\tau}.$$

The second moment of the direct radiation exceeds the zeroth moment by a factor of five, since $P_2(1)=1$.

For a noninstantaneous and nonmonochromatic source, the emitted energy may depend on η_s and x_s, and all the equations and their solutions must be integrated over these parameters. This does not present a problem, due to the presence of δ functions in these expressions.

3.6. A Planar Source

For comparison, a layered planar source can be considered. This is only possible if the geometry of the space itself is flat, $k=0$. As always in a planar geometry, the equation of radiative transfer does not contain an angular derivative, since the angle θ between the direction of propagation of the radiation and the normal to the source plane along the ray remains constant. Thus, the transfer equations for a planar geometry can be obtained from the corresponding equations for spherical geometry, simply by omitting the term with the derivative with respect to the angle θ. In the expression for the source term and

the intensity of the direct radiation, the combination $\delta(\chi)/\mathrm{sn}_k^2(\eta)$ must be replaced by $\delta(\chi-\chi_\mathrm{s})$.

Thus, the transfer equation acquires the form

$$\frac{c}{R(\eta)}\left[\frac{\partial n}{\partial \eta}+\cos\vartheta\frac{\partial n}{\partial \chi}\right]-xH\frac{\partial n}{\partial x}=c\mathcal{I}_\mathrm{c},$$

where the collision integral $\mathcal{I}_\mathrm{c}$ is specified by the same formula (20). In this case, the source term is

$$\epsilon_*(\eta,\chi,\mu,x)=L_\mathrm{s}\frac{c^3}{2h\nu_\star^4}\frac{\delta(\eta-\eta_\mathrm{s})}{R^2(\eta_\mathrm{s})}\delta(\chi-\chi_\mathrm{s})$$
$$\times\frac{\delta(\cos\vartheta-\cos\vartheta_\mathrm{s})}{2\pi}\frac{\delta(x-x_\mathrm{s})}{x_\mathrm{s}^3}.$$

The source is assumed to be located at the level with χ_s. Here, we calculate its luminosity per area of the planar boundary; for this reason, the denominator contains a second power of the radius of curvature. We assume that the source radiation does not depend on azimuth and propagates at an angle ϑ_s relative to a normal to the layers.

4. OPTICAL DISTANCES

4.1. Optical Distance from the Source

Under the adopted conditions, the densities of electrons n_e and protons n^+ depend only on time (and, of course, the cosmological model). In the case of total ionization, $n^+=n_\mathrm{e}=n_\mathrm{e}^0/a^3(\eta)$; in the case of partial ionization, the ionization equation must be solved. We will assume that the matter consists of completely ionized hydrogen.

Expressions for the coefficient of bremsstrahlung absorption by thermal nonrelativistic electrons and the absorption coefficient for Thomson scattering were given in Section 2.

Since the scattering coefficient does not depend on frequency, the corresponding optical distance can be determined very easily. If a photon was emitted from the source at time η_s, its equation of motion is $\chi=\eta-\eta_\mathrm{s}$. In the course of its motion, the optical distance between the photon and the source will increase according to the relation

$$\tau_T(\eta,\eta_\mathrm{s})=\int_0^\chi\alpha_T(\eta_\mathrm{s}+\chi')R(\eta_\mathrm{s}+\chi')d\chi'$$
$$=\int_{\eta_\mathrm{s}}^\eta\alpha_T(\eta')R(\eta')d\eta'=\tau_T(\eta)-\tau_T(\eta_\mathrm{s}),$$

where the universal Thomson opacity is

$$\tau_T(\eta)=\int_{\eta_\mathrm{i}}^\eta\alpha_T(\eta)R(\eta)d\eta \qquad (23)$$
$$=\sigma_T\int_{\eta_\mathrm{i}}^\eta n_\mathrm{e}(\eta)R(\eta)d\eta.$$

Since only differences in the optical distances are of interest, the lower integration limit in this formula can be chosen arbitrarily.

The situation with the bremsstrahlung mechanism is more complicated, since in this case, the absorption cross section depends on both the frequency and temperature. The time dependence of the frequency is described as follows. Let the frequency of a photon emitted from the source at time $t_\mathrm{s}=t(\eta_\mathrm{s})$ be ν_s. Then, its frequency at time $t=t(\eta)$, will be $\nu=\nu_\mathrm{s}a(\eta_\mathrm{s})/a(\eta)$. The temperature also depends on the time, according to the usual formula, $T=T_0/a(\eta)=T_\mathrm{s}a(\eta_\mathrm{s})/a(\eta)$, where $T_\mathrm{s}=T_0/a(\eta_\mathrm{s})$ is the temperature when the photon is emitted. The ratio $\nu/T=\nu_\mathrm{s}/T_\mathrm{s}$ is time-independent.

Since the particle densities, frequency, and temperature depend on time in a known way, the absorption coefficient is a known function of η or z:

$$\tau_\mathrm{cc}(\eta,\eta_\mathrm{s},x)=\left(1-e^{-h\nu_*x_\mathrm{s}/k_\mathrm{B}T_\mathrm{s}}\right)\int_0^\chi n_\mathrm{e}(\eta_\mathrm{s}+\chi')$$
$$\times n^+(\eta_\mathrm{s}+\chi')\frac{k_\mathrm{cc}^0}{\nu_\star x_\mathrm{s}^3a^{7/2}(\eta_\mathrm{s})T_\mathrm{s}^{1/2}}a^{7/2}(\eta_\mathrm{s}+\chi')$$
$$\times R(\eta_\mathrm{s}+\chi')d\chi'=\left(1-e^{-h\nu_\star x/k_\mathrm{B}T}\right)R_0$$
$$\times k_\mathrm{cc}(\nu_\star x_\mathrm{s}a(\eta_\mathrm{s}),T_\mathrm{s}a(\eta_\mathrm{s}))[E(\eta)-E(\eta_\mathrm{s})],$$

where

$$E(\eta)=\int_{\eta_\mathrm{i}}^\eta n_\mathrm{e}(\eta)n^+(\eta)a^{9/2}(\eta)d\eta \qquad (24)$$

is a quantity similar to the emission measure. The total optical distance from the source is

$$\tau(\eta,\eta_\mathrm{s},x)=\tau_T(\eta,\eta_\mathrm{s})+\tau_\mathrm{cc}(\eta,\eta_\mathrm{s},x).$$

4.2. Calculation of the Scattering Optical Distance

Let us choose for the initial times in (23) and (24) the times $t_\mathrm{i}=t(\eta_\mathrm{i})$ for which the ratio $y=\mathrm{sn}_k(\eta)/\mathrm{sc}_k(\eta)$ assumes the values from the table. The table also presents the products $X=\dfrac{a_\mathrm{r}}{a_\mathrm{d}}y=By$ for the same times. Here, we have chosen simple

values for this ratio; in fact, the values of η_i are maximum for $k = 0$ and $k = -1$, $\eta < \eta_i$, so that the optical distance (23) will be negative. This does not cause any problems, since only the differences of these quantities, which are positive, will be needed. When $k = 1$, the value of η_i is finite, since the range of variations of this variable is finite in a closed model.

We will rewrite the integral (23), substituting the time dependence of the electron density, $n_e = n_e^0/a^3(\eta) = (\rho_b^0/m_H)/a^3(\eta)$, where ρ_b^0 is the current baryon density:

$$\tau_T(\eta) = \sigma_T \int_{\eta_i}^{\eta} n_e R(\eta) d\eta = \sigma_T \frac{\rho_b^0}{m_H} R_0 \int_{\eta_i}^{\eta} \frac{d\eta}{a^2(\eta)}.$$

Introducing the new variable of integration $X = \frac{a_r}{a_d} y = By$, where y is specified by (9), and using the characteristics of this ratio enables us to reduce the integral to the form

$$\int_{\eta_i}^{\eta} \frac{d\eta}{a^2(\eta)} = -\frac{1}{2} \int_{y_i}^{y} \frac{y^2 + k}{(a_r y + a_d)^2} dy$$

$$= -\frac{1}{2} \frac{a_d}{a_r^3} f_T(X, B, k),$$

$$f_T(X, B, k) = \int_{X_i}^{X} \frac{X_1^2 + kB^2}{(X_1 + 1)^2} dX_1.$$

Calculating the integral within the limits indicated in the table yields for $k = 0$ and 1:

$$f_T(X, B, k) = X \frac{X + 2 + kB^2}{X + 1} - 2\ln(X + 1). \tag{25}$$

When $k = -1$, the constant $B(B - 2) + 2\ln(1 + B)$ is added, so that, in an open model, this function can also be written in a form that explicitly vanishes for the limiting value of the argument, $X = B$:

$$f_T(X, B, -1) = (X - B) \frac{X - B + 2}{X + 1} - 2\ln \frac{X + 1}{B + 1}.$$

For arguments close to the limiting value, $X \to 0$, the function (25) is equivalent to $f_T(X, B, k) \sim kB^2 X(1 - X) + (1/3 + kB^2)X^3$, while for an open model, we obtain as $X \to B$ then $f_T(X, B, -1) \sim \frac{(X - B)^2}{(B + 1)^2} \left[B + \frac{1/3 - B}{B + 1} (X - B) \right]$.

η_i, y_i, and X_i

Model	y	η_i	y_i	X_i
$k = 1$	$\cot(\eta/2)$	π	0	0
$k = 0$	$2/\eta$	∞	0	0
$k = -1$	$\cot(\eta/2)$	∞	1	a_r/a_d

Thus, the optical distance based on Thomson scattering is given by the formula

$$\tau_T(\eta, \eta_s) = \frac{\sigma_T}{4} \frac{\rho_b^0}{m_H} \frac{\rho_d^0}{\rho_r^0} \left(\frac{8\pi G}{3c^2} \rho_r^0 \right)^{-1/2} \times [f_T(X_s, B, k) - f_T(X, B, k)], \tag{26}$$

where $B = \frac{a_r}{a_d}$, $X = By = B \frac{\mathrm{sn}_k(\eta)}{\mathrm{sc}_k(\eta)}$, and $X < X_s$ for $\eta > \eta_s$. The factor before the bracket can also be written as $\frac{\sigma_T}{4} \frac{\rho_b^0}{m_H} \frac{\Omega_d^0}{(\Omega_r^0)^{3/2}} \frac{c}{H_0}$.

4.3. Calculation of the Absorption Optical Distance

Let us calculate the function (24). After making the same substitutions as for the Thomson-scattering distance calculation, we obtain

$$E(\eta) = \left(\frac{\rho_b^0}{m_H} \right)^2 \int_{\eta_i}^{\eta} \frac{d\eta}{a^{3/2}(\eta)}$$

$$= -\left(\frac{\rho_b^0}{m_H} \right)^2 \frac{1}{\sqrt{2}} \int_{y_i}^{y} \frac{\sqrt{y^2 + k}}{(a_r y + a_d)^{3/2}} dy$$

$$= -\left(\frac{\rho_b^0}{m_H} \right)^2 \frac{1}{\sqrt{2}} \frac{a_d^{1/2}}{a_r^2} f_c(X, B, k),$$

where

$$f_c(X, B, k) = \int_{X_i}^{X} \frac{\sqrt{X_1^2 + kB^2}}{(X_1 + 1)^{3/2}} dX_1.$$

Only for $B = 0$ (i.e. for $k = 0$) can the integral be expressed in terms of elementary functions:

$$f_c(X) = f_c(X, 0, 0) = 2\sqrt{X + 1} + \frac{2}{\sqrt{X + 1}} - 4 = 2 \frac{(\sqrt{X + 1} - 1)^2}{\sqrt{X + 1}}$$

$$= \frac{2}{\sqrt{X + 1}} \frac{X^2}{(\sqrt{X + 1} + 1)^2}. \tag{27}$$

If $B \neq 0$, the integral can be expressed in terms of elliptical integrals, but it is easier to calculate it numerically.

4.4. Calculations of Optical Distances for the Nonvacuum Model

For the values in (26), we will obtain $B = 5.321 \times 10^{-2}$.

Let us consider optical distances in the selected model. We will first calculate the dimensionless functions f_T and f_c for redshifts z from 10^8 to 10^2. Assuming that the photon was emitted from the source at time η_s, the Thomson-scattering distance at time η is specified by (26). The factor before the bracket in this formula is equal to 156.2.

The optical distance based on absorption can be determined in a similar way. After substituting expressions for its terms, the product $R_0E(\eta)$ is shown to be

$$R_0E(\eta) = -\frac{1}{2}\left(\frac{\rho_b^0}{m_H}\right)^2 \frac{\sqrt{\rho_d^0}}{\rho_r^0}\left(\frac{8\pi G}{3c^2}\right)^{-1/2} \times f_c(X,B,-1) = -\frac{1}{2}\left(\frac{\rho_b^0}{m_H}\right)^2 \frac{\sqrt{\Omega_d^0}}{\Omega_r^0}\frac{c}{H_0} \times f_c(X,B,-1).$$

Let us estimate the optical distance for the frequency at which the Planck function reaches its maximum at a certain cosmological time, $\nu_m = c_W k_B T/h, c_W = 2.821438$. For this distance,

$$\tau_{cc} = (1-e^{-c_W})\left(\frac{\rho_b^0}{m_H}\right)^2 \frac{k_{cc}^0}{T_0^{7/2}}\left(\frac{h}{c_W k_B}\right)^3 \quad (28)$$
$$\times \frac{\sqrt{\Omega_d^0}}{\Omega_r^0}\frac{c}{2H_0}[f_c(X_s,B,-1) - f_c(X,B,-1)].$$

4.5. Calculation of Optical Distance for a Flat Model

The optical distances needed for our model have already been determined. Let us rewrite them using new notation. The scattering optical distance is

$$\tau_T = \sigma_T \frac{\rho_b^0}{m_H} R_0 \frac{2c}{\widetilde{H}_0 R_0}\frac{\Omega_0}{8(1-\Omega_0)^{3/2}} \quad (29)$$
$$\times \left[f_T\left(\frac{\sqrt{1-\Omega_0}}{\Omega_0}\frac{2}{\zeta_s}\right) - f_T\left(\frac{\sqrt{1-\Omega_0}}{\Omega_0}\frac{2}{\zeta}\right)\right]$$
$$= \frac{\sigma_T}{4}\frac{\rho_b^0}{m_H}\frac{c}{\widetilde{H}_0}\frac{\Omega_0}{(1-\Omega_0)^{3/2}}[f_T(X_s) - f_T(X)].$$

We have obtained the same formula, (26); the function f_T coincides with that determined from (25), but, since $B = 0$ and $k = 0$, it does not contain any parameters:

$$f_T(X) = X\frac{X+2}{X+1} - 2\ln(X+1).$$

Taking into account the relations between the Hubble constant and critical parameters (14a), (14b), and (14c), we will see that the coefficients before the brackets in (29) and (26) also exactly coincide.

The absorption distance is calculated in exactly the same way. This product is equal to

$$R_0E(\eta) = -\frac{1}{2}\left(\frac{\rho_b^0}{m_H}\right)^2 \frac{\sqrt{\Omega_0}}{1-\Omega_0}\frac{c}{\widetilde{H}_0} f_c(X),$$

where the function $f_c(X)$ is specified by the previous formula (27). The resulting formula for the absorption distance is

$$\tau_{cc} = (1-e^{-c_W})\left(\frac{\rho_b^0}{m_H}\right)^2 \frac{k_{cc}^0}{T_0^{7/2}}\left(\frac{h}{c_W k_B}\right)^3 \quad (30)$$
$$\times \frac{\sqrt{\Omega_0}}{1-\Omega_0}\frac{c}{2\widetilde{H}_0}[f_c(X_s) - f_c(X)].$$

Here, the coefficients in (28) and (30) also coincide.

4.6. Comparing the Two Models

The optical distances in the two models considered differ only in the functions f; in the flat model, $B = 0$, while this parameter is $B \approx 0.05$ in the open model, so that the difference is insignificant. Indeed, this difference

$$f_T(X) - f_T(X,B,-1) = B^2\frac{X}{X+1} - B(B-2) - 2\ln(B+1)$$

is small for both small and large X. The term that is independent of X disappears when the difference of the functions is taken. The difference between the functions f_c is more difficult to estimate, since these functions have different domains:

$$f_c(X) - f_c(X,B,-1) = \int_0^B \frac{X_1}{(X_1+1)^{3/2}}dX_1 + \int_B^X \frac{X_1 - \sqrt{X_1^2 - B^2}}{(X_1+1)^{3/2}}dX_1$$
$$= \frac{2}{\sqrt{1+B}}\frac{B^2}{(1+\sqrt{1+B})^2} + B^2\int_B^X \frac{1}{(X_1+1)^{3/2}}\frac{dX_1}{X_1+\sqrt{X_1^2-B^2}}.$$

The order of the difference is B^2. For small $X \sim B$, this can be seen directly, while, in the case of larger X, the contribution of large values of X_1 to the integral is small.

We can describe the behavior of our functions for small and large X. When $X \to 0$,

$$f_T(X) = X^3 \sum_{n=0}^{\infty} (-1)^n \frac{n+1}{n+3} X^n,$$

$$f_c(X) = X^2 \sum_{n=0}^{\infty} (-1)^n \frac{(2n+1)!}{2^n n!(n+2)}.$$

For large X,

$$f_T(X) = X - 2\ln X + 1 - \frac{1}{X} \sum_{n=0}^{\infty} \frac{(-1)^n}{X^n} \frac{n+3}{n+1},$$

$$f_c(X) = 2X^{1/2} \sum_{n=0}^{\infty} (-1)^{n-1} \frac{(2n-3)!}{(2n)!} \frac{2n+1}{X^n} - 4.$$

Here, as usual, we assume that $(-3)! = -1$, $(-1)! = 1$.

For the large redshifts of interest for us or, more exactly, for $(1-\Omega_0)z \gg 1$, the parameters ζ, y, and X behave as follows:

$$\zeta \sim \frac{1}{2\sqrt{1-\Omega_0}} \frac{1}{z}, \quad y = \frac{1}{\zeta} \sim 2\sqrt{1-\Omega_0} z,$$

$$X = 2\frac{\sqrt{1-\Omega_0}}{\Omega_0} y \sim 4\frac{1-\Omega_0}{\Omega_0} z.$$

Accordingly, the functions f are easy to determine for such z values. The scattering optical distances calculated for the open and flat models are only different for the largest z, and even then only slightly: for $z = 10^8$, in the fourth significant figure. The absorption distances display larger but also insignificant differences, in the third significant figure for all z.

Figure 2 presents the results of these calculations. The starting value for the curves is $z = z_s$; $\log z_s = n_s = 4(1)8$. To present the curves on comparable scales, the τ_T values on the curve with $\log z_s = n_s$ have been multiplied by 10^{1-n_s}, while the τ_{cc} curves have been multiplied by $10^{(17-n_s)/2}$. The difference between these factors reflects the fact that the absorption coefficient is proportional to $T^{-1/2}$.

We can see from the figures that the optical distances initially increase rapidly with decreasing redshift; this growth is slower for the absorption distances at the frequency of the maximum of the Planck function. If the source's redshift is $z = z_s$, then, for $z_s/3 \le z \le z_s$, these distances are

$$\tau_T \sim \sigma_T \frac{\rho_b^0}{m_H} \frac{c}{\widetilde{H}_0} \frac{z_s - z}{\sqrt{1-\Omega_0}},$$

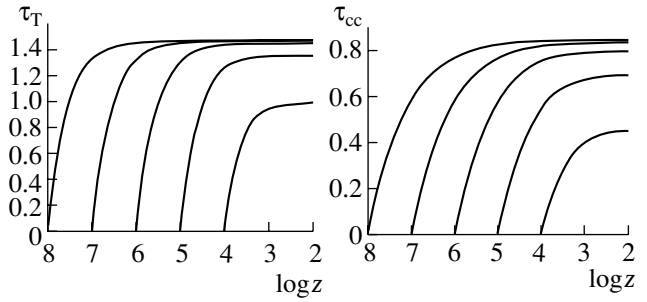

Fig. 2. Scattering and absorption optical distances as a function of the photon redshift in the course of the photon's motion away from the source. The τ_T values are multiplied by $10/z_s$, and the τ_{cc} values by $10^{-8.5} z_s^{-1/2}$.

$$\tau_{cc} \sim (1 - e^{-c_W}) \left(\frac{\rho_b^0}{m_H}\right)^2 \frac{k_{cc}^0}{T_0^{7/2}} \times \left(\frac{h}{c_W k_B}\right)^3 \frac{c}{\widetilde{H}_0} \frac{\sqrt{z_s}}{\sqrt{1-\Omega_0}} \left(1 - \frac{z}{z_s}\right).$$

For the adopted model parameters, $\tau_T \approx 0.13(z_s - z)$ and $\tau_{cc} \approx 1.8 \times 10^{-9} z_s^{-1/2}(z_s - z)$. The optical distances increase more slowly with decreasing z, gradually reaching their asymptotic values $\tau_T \sim 0.14 z_s$ and $\tau_{cc} \sim 2.5 \times 10^{-9} z_s^{1/2}$. The distances τ_{cc} reach their limiting values at smaller z, and these values are substantially smaller (by a factor of $5.6 \times 10^6 z_s^{1/2}$) than those for the scattering distances. Since the coefficient k_{cc} is inversely proportional to the third power of the frequency, this difference will be smaller at lower frequencies.

4.7. The Grey Approximation

Since the scattering coefficient substantially exceeds the absorption coefficient, the latter can be neglected relative to the source radiation. Equation (18) with the right-hand side (20) can then be integrated over frequency, as is done in calculations of model atmospheres [4].

Let us denote the frequency moments for the mean occupation number ($s \ge 0$ is not necessarily integer, so that this is essentially the Mellin transform):

$$n^{(s)}(\eta, \chi, \mu) = \int_0^{\infty} x^s n(\eta, \chi, \mu, x) dx.$$

Integration over the frequency with the weights x^s

yields

$$\frac{\partial n^{(s)}}{\partial \eta} + \mu \frac{\partial n^{(s)}}{\partial \chi} + (1-\mu^2)\frac{\mathrm{cs}_k(\chi)}{\mathrm{sn}_k(\chi)}\frac{\partial n^{(s)}}{\partial \mu} + (s+1)\frac{a'(\eta)}{a(\eta)} n^{(s)} = R(\eta)\mathcal{I}_{\mathrm{c}}^{(s)},$$

where $\mathcal{I}_{\mathrm{c}}^{(s)}$ is the result of integrating the right-hand side. The integral of the term with the frequency derivative was calculated via integration by parts.

The frequency moments of the collision integral are

$$\mathcal{I}_{\mathrm{c}}^{(s)} = -\alpha_T \left[n^{(s)}(\eta,\chi,\mu) - n_0^{(s)}(\eta,\chi) - \frac{1}{10} P_2(\mu) n_2^{(s)}(\eta,\chi) \right] + \epsilon_*^{(s)}(\eta,\chi,\mu),$$

where the moments of the source power are

$$\epsilon_*^{(s)}(\eta,\chi,\mu) = \int_0^\infty \epsilon_*(\eta,\chi,\mu,x) x^s dx.$$

After separating out the direct radiation, the function ϵ_* should be substituted by ϵ_{s}.

5. CONCLUSION

We have derived an equation describing the evolution of the radiation of a source whose intensity exceeds that of the surrounding equilibrium background radiation at the epoch of radiation-dominated plasma, between the epochs of annihilation and recombination. A cosmological model for this period was adopted. We have separated the diffuse and direct radiation, and calculated the opacities of the matter due to Thomson scattering and bremsstrahlung absorption. The latter mechanism can be neglected relative to the source radiation, and this fact was used to obtain an equation for the frequency moments.

This is the first paper in the series of studies that will be concerned with elucidating how sources of radiation affect the evolution of the Universe and how their presence is reflected in the thermal background radiation, taking into account the fact that the accuracy of observations is growing steadily. We hope to solve this problem in our forthcoming studies.

REFERENCES

1. Ya. B. Zel'dovich and I. D. Novikov, *Structure and Evolution of the Universe* (Nauka, Moscow, 1975; University of Chicago Press, 1983).
2. V. K. Dubrovich, Pis'ma Astron. Zh. **29**, 9 (2003) [Astron. Lett. **29**, 6 (2003)].
3. A. D. Chernin, Astron. Zh. **42**, 1124 (1965) [Sov. Astron. **9**, 871 (1965)].
4. V. V. Sobolev, *A Course in Theoretical Astrophysics* (Nauka, Moscow, 1985) [in Russian].

Translated by K. Maslennikov

Astronomy Reports, Vol. 49, No. 3, 2005, pp. 179–189. Translated from Astronomicheskiĭ Zhurnal, Vol. 82, No. 3, 2005, pp. 207–218.

Polarization Effects in the Radiation of Magnetized Envelopes and Extended Accretion Structures

Yu. N. Gnedin[1], N. A. Silant'ev[2], M. Yu. Piotrovich[1], and M. A. Pogodin[1]

[1] *Pulkovo Astronomical Observatory, Russian Academy of Sciences, Pulkovskoe sh. 65, St. Petersburg, 196140 Russia*

[2] *Instituto Nacional de Astrofísica, Óptica y Electrónica, Luis Enrique Erro No. 1, Apdo Postal 51 y 216, 72840 Tonantzintla, Puebla, Mexico*

Received February 26, 2004; in final form, September 20, 2004

Abstract—We have calculated the degree and position angle of the polarization of radiation scattered in a magnetized, optically thin or optically thick envelope around a central source, taking into account Faraday rotation of the plane of polarization during the propagation of the scattered radiation and the finite size of the radiation source. The wavelength dependence of the degree of polarization can be used to estimate the magnetic field of the source (a star, the region around a neutron star, or a black hole), and we have used our calculations to estimate the magnetic fields in a number of individual objects: several hot O and Wolf–Rayet stars, compact objects in X-ray close binaries with black holes (SS 433, Cyg X-1), and supernovae. The spectrum of the linear polarization can be used to determine the magnetic field in the vicinity of a central supermassive black hole, where the polarized optical radiation is generated. In a real physical model, this value can be extrapolated to the region of the last stable orbit. In the future, the proposed technique will make it possible to directly estimate the magnetic field in the region of the last stable orbit of a supermassive black hole using X-ray polarimetry. © *2005 Pleiades Publishing, Inc.*

1. INTRODUCTION

In the presence of a magnetic field, the plane of polarization of radiation propagating through the hot electron atmospheres and envelopes of stars or the accretion envelopes around quasars and active galactic nuclei is subject to Faraday rotation. The angle of rotation ψ is related to the parameters of the medium and the path of the radiation l by the expression [1]:

$$\psi = \frac{1}{2}\delta\tau_T \cos\Theta, \qquad (1)$$

where $\tau_T = N_e l\sigma_T$ is the Thomson optical depth along the path, $\sigma_T = (8\pi/3)r_e^2 \cong 6.65\times10^{-25}$ cm^2 is the Thomson-scattering cross section, $r_e = e^2/m_ec^2 \cong 2.82\times10^{-13}$ cm is the classical electron radius, N_e is the electron density, and Θ is the angle between the direction of propagation $\mathbf{n}$ and the magnetic field $\mathbf{B}$. The plane of polarization undergoes right-handed or left-handed rotation if $\Theta < 90°$ or $\Theta > 90°$, respectively, for an observer looking along the direction of propagation. The parameter δ is numerically equal to the rotation angle of the plane of polarization for a path $\tau_T = 2$ along the magnetic field, and is given by the formula

$$\delta = \frac{3}{4\pi}\frac{\lambda}{r_e}\frac{\omega_B}{\omega} \cong 0.8(\lambda\ [\mu\mathrm{m}])^2 B\ [\mathrm{G}]. \qquad (2)$$

Here, $\lambda = 2\pi c/\omega$ is the wavelength of the radiation, $\omega = 2\pi\nu$ is its angular frequency, and $\omega_B = |e|B/m_ec$ is the cyclotron frequency of the electrons in the magnetic field, $\omega_B/\omega \cong 0.93\times10^{-8}\lambda\ [\mu\mathrm{m}]\ B\ [\mathrm{G}]$.

Away from a neutron star or quasar, its magnetic field can be taken to be roughly dipolar, since the multipolar field components fall off with distance faster than the main dipolar component. Optically thick envelopes are probably fairly rare, due to the smallness of the Thomson-scattering cross section. It is possible that optically thick envelopes are formed by the matter ejected in the initial stages of supernovae, when the density of the ejected particles has not yet decreased substantially. Another example may be extended accretion structures surrounding quasars or active galactic nuclei.

The magnetospheres around black holes, including supermassive black holes, play a key role in the formation of various outflowing structures (winds, coronas, jets, etc.). The existence of such magnetospheres was recently confirmed by spectroscopic [2] and polarimetric [3] observations of X-ray binaries containing black holes.

On the other hand, the model of Blanford and Znajek [4], in which energy is extracted from a rotating black hole via the magnetic field, has stood the test of time. This idea evolved further in [5–7], with the

development of a model in which a toroidal current at the inner boundary of the disk can generate a dipolar magnetic field that connects the horizon of the black hole with the region of its accretion disk beyond its inner boundary.

The outflow of plasma from the magnetosphere and the inner part of the accretion disk forms an envelope, in which scattering-driven polarization can originate. One example of such an envelope is the broad line regions of active galactic nuclei—regions in which broad emission lines are generated.

In the absence of a magnetic field, the integrated polarization of the radiation scattered in an envelope is zero due to the axial symmetry relative to the line of sight. A magnetic field breaks this symmetry, since the (singly- or multiply-) scattered outgoing radiation undergoes nonradially symmetrical Faraday rotation as it propagates through the envelope. Axial symmetry remains only in the case of a dipolar field with its magnetic dipole $\mathbf{M}$ parallel to the line of sight $\mathbf{n}$: the integrated polarization of the radiation is then zero, as in the absence of the magnetic field.

2. AN OPTICALLY THIN ENVELOPE

The integrated polarization of radiation scattered in an optically thin envelope is relatively easy to calculate. In this case, only two factors need to be taken into account: single scattering of light from the central source on electrons in the envelope, and subsequent Faraday rotation of the plane of polarization as the scattered radiation passes through the envelope. Such calculations were carried out for various envelopes in [8–10]; however, it was assumed that a star is a point source of unpolarized radiation, leading to overestimation of the integrated polarization (see details below). The largest violation of the axial symmetry in the Faraday rotation occurs along the direction of the magnetic dipole $\mathbf{M}$, perpendicular to the line of sight $\mathbf{n}$ ($\vartheta_m = 90^\circ$). In this case, the integrated polarization reaches its maximum. The plane of polarization coincides with the plane containing the line of sight $\mathbf{n}$ and the magnetic-dipole axis $\mathbf{M}$.

According to [1, 8, 9], the Stokes parameters of the radiation received at the telescope are given by the expressions

$$F_Q(\mathbf{n}) = -\frac{L}{4\pi R^2}\frac{3}{16\pi}\sigma_T \times \int dV \frac{N_e(\mathbf{r})}{r^2}\sqrt{1-\frac{R_s^2}{r^2}}\sin^2\vartheta\cos 2(\varphi+\psi), \quad (3)$$

$$F_U(\mathbf{n}) = -\frac{L}{4\pi R^2}\frac{3}{16\pi}\sigma_T \times \int dV \frac{N_e(\mathbf{r})}{r^2}\sqrt{1-\frac{R_s^2}{r^2}}\sin^2\vartheta\sin 2(\varphi+\psi), \quad (4)$$

where L and R_s are the luminosity and radius of the star, R is the distance between the star and observer, and $\psi(\mathbf{r},\mathbf{n})$ is the angle through which the plane of polarization of radiation scattered in the volume element $dV(\mathbf{r})$ in the line of sight $\mathbf{n}$ rotates due to Faraday rotation (1). The radius vector of a volume element dV is specified by the usual spherical coordinates r, ϑ, φ. The integration is carried out over the entire visible part of the envelope. It is assumed in (3) and (4) that the X axis lies in the $(\mathbf{nM})$ plane. The polarization of the scattered radiation is small near the surface of the star, since the radiation falls onto the volume element dV almost isotropically. This effect is described analytically in [1, Ch. 4] for the frequently considered case when the intensity $I(\mu)$ of the radiation emerging from the stellar surface is approximated by the simple expression $I(\mu) = A + C\mu$. Recall that μ is the cosine of the angle between the normal to the stellar surface and the direction of propagation of the emergent radiation. Here, we consider only the case of an isotropic intensity ($C = 0$), when the depolarization of the radiation scattered near the surface reaches its maximum. This leads to the appearance of an additional factor of $\sqrt{1-R_s^2/r^2}$ in (3) and (4) compared to the analogous formulas in [8–10], where the star was assumed to be a point source. The impact of the non-pointlike nature of the source on the polarization of radiation scattered in a magnetized envelope was first calculated in [11].

We will restrict our consideration to two electron-density distributions in the envelope, $N_e(\mathbf{r})$: $N_e(r) = N_0 = \text{const}$ and $N_e(r) = N_0(R_s^2/r^2)$. The explicit analytical formulas for the Faraday-rotation angle ψ are as follows [8].

For an envelope with a constant density,

$$\psi = \frac{\delta_s \tau_{env}}{2(\eta-1)\rho^2} \times \left\{ \cos\vartheta_m \left[\cos\vartheta - \frac{\rho^2}{\eta^2}\sqrt{1-\frac{\rho^2}{\eta^2}\sin^2\vartheta} \right] + \sin\vartheta_m \cos\varphi \sin\vartheta \left(1-\frac{\rho^3}{\eta^3}\right) \right\}, \quad (5)$$

where $\eta = R_0/R_s$ is the ratio of the radii of the envelope and star, $\rho = r/R_s$ the dimensionless distance from the center of the star to the volume element, $\delta_s = 0.8\lambda^2 M/R_s^3$ the parameter (2) at the magnetic equator of the star, M is the magnetic moment of the star, $\tau_{env} = N_0\sigma_T(R_0 - R_s)$ is the Thomson optical depth of the envelope, ϑ_m is the inclination of the magnetic dipole $\mathbf{M}$ to the direction toward the observer $\mathbf{n}$.

For an envelope in which the electron density depends on the radius as $N_e \sim r^{-2}$,

$$\psi = \frac{\delta_s \tau_{env}}{2\rho^4 \sin^4\vartheta}\left\{\cos\vartheta_m\left[-(1-\cos\vartheta)\right.\right. \quad (6)$$
$$\left. + \frac{4}{3}(1-\cos^3\vartheta) - \frac{3}{5}(1-\cos^5\vartheta)\right]$$
$$\left. + \frac{3}{5}\sin\vartheta_m\cos\varphi\sin^5\vartheta\right\},$$

where $\tau_{env} = N_0\sigma_T R_s$ is the optical depth of the envelope.

Note that, terms of order $\sim\tau_{env}^2$ and higher orders in smallness are omitted in the above formulas, since we are restricting our consideration to singly-scattered radiation. In this approximation, it is sufficient to take $L/4\pi R^2$ for the flux F_I when determining the degree of polarization $p_l = \sqrt{F_Q^2 + F_U^2}/F_I$.

It follows from (3) and (4) that the parameters F_Q and F_U are

$$F_{Q,U} = F_I \tau_{env} f_{Q,U}(\delta_s\tau_{env}, \vartheta_m, \eta). \quad (7)$$

For an envelope with $N_e \sim r^{-2}$, (7) does not contain η.

For weak magnetic fields or short wavelengths, when $\psi \ll 1$, the function $f_{Q,U}$ is expressed in the asymptotic form

$$f_Q \simeq K_Q(\delta_s\tau_{env})^2\sin^2\vartheta_m, \quad (8)$$
$$f_U \simeq K_U(\delta_s\tau_{env})^3\cos\vartheta_m\sin^2\vartheta_m.$$

Since $\psi \propto \delta_s\tau_{env}$, $|f_U| \ll |f_Q|$; i.e., the electric vector of the radiation fluctuates near the **nM** plane, while the degree of polarization is $p_l \approx \tau_{env}|f_Q|$. Formulas (8) are satisfied well up to values $\delta_s\tau_{env} \approx 1$.

Figure 1 presents $p_l/\tau_{env} = (f_Q^2 + f_U^2)^{1/2}$ (in percent) and the position angle χ (in degrees) as functions of $\sqrt{\delta_s\tau_{env}}$. The X axis lies in the (**nM**) plane. The upper plots correspond to $N_e(r) = N_0(R_s/r)^2$, and the lower plots to an envelope with a constant electron density (with $\eta = 5$) for a non-pointlike star. To derive the degree of polarization, the right plots must be multiplied by $\tau_{env} < 1$.

In the case of an optically thin envelope, $p_{\max}$ (for $\vartheta_m = 90°$) can reach substantial values, $\sim 6\tau_{env}$ (%) for a non-pointlike and $\sim 10\tau_{env}$ (%) for a pointlike star. In each envelope, there exists an effective layer with $\psi \simeq 1$, which makes the dominant contribution to the integrated polarization.

In the case of strong magnetic fields, the polarization is determined by a thin layer at the outer boundary of the envelope, where the Faraday rotation is comparatively small, $\psi \leq 1$. This occurs when the optical depth of this layer is $\tau \propto 1/\delta_0 \propto \lambda^{-2}$, where $\delta_0 = 0.8\lambda^2 M/R_0^3$ is the parameter (2) at the surface of the envelope. This estimate suggests that, with the exception of this thin surface layer, the bulk of the envelope does not contribute to the integrated polarization; i.e., $\delta_s\tau_{env}/\eta^3 \gg 1$. The intensity of the radiation scattered in this layer is proportional to the optical depth τ. Therefore, the integrated polarization specified by this intensity is inversely proportional to δ_0, $p_l \simeq C(\vartheta_m)\eta^3/\lambda^2$. Analytical calculations for the case $\vartheta_m = 90°$ yield

$$p_l \approx \frac{\pi\eta^3}{16\delta_s}\sqrt{1-\frac{1}{\eta^2}} \propto \frac{1}{\lambda^2}, \quad \frac{\delta_s\tau_{env}}{\eta^3} \gg 1. \quad (9)$$

The asymptotic dependence $p_l \propto \lambda^{-2}$ is satisfied relatively well starting from $\delta_s\tau_{env}/\eta^3 \approx 50$–$100$. Formula (9) was obtained without eliminating the contribution of the part of the envelope obscured from the observer by the star itself; thus, (9) overestimates the polarization.

As was shown in [1], a star can essentially be treated as a point source of unpolarized radiation starting from a distance of one to two stellar radii

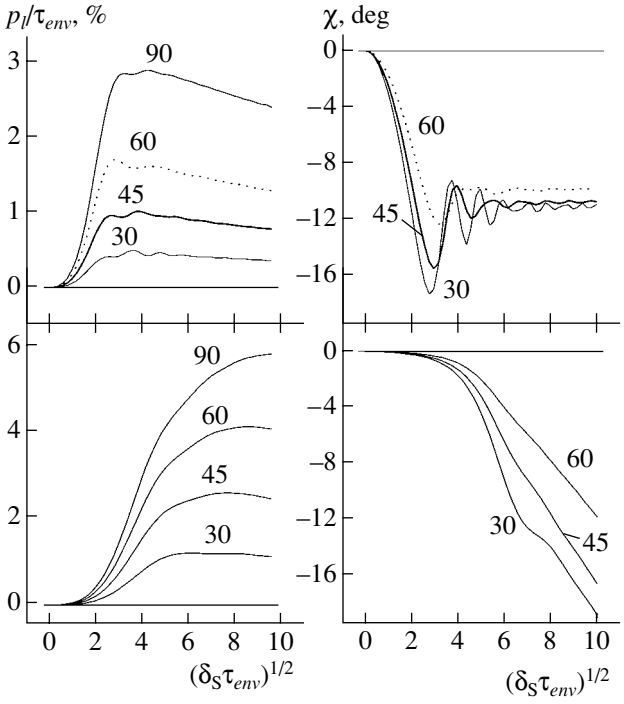

Fig. 1. Degree and position angle of the polarization of the integrated radiation in an optically thin spherical envelope in a magnetic-dipolar field. The upper plots correspond to an electron density $\propto r^{-2}$, and the lower plots to a constant electron density with $\eta = 5$. The inclination of the magnetic-dipole axis **M** to the line of sight **n**, ϑ_m, is indicated in degrees. See text for details.

from the stellar surface. Therefore, the asymptotic polarization for $\delta_s\tau_{env} \gg 1$ is the same for pointlike and non-pointlike stars (provided the thickness of the envelope exceeds two to three stellar radii).

For an envelope with an electron density $N_e \sim r^{-2}$, the maximum degree of polarization for $\vartheta_m = 90^\circ$ corresponds to $\sqrt{\delta_s\tau_{env}} \simeq 4.65$, and is equal to $2.886\%\tau_{env}$ for a non-pointlike star. For the same value of $\sqrt{\delta_s\tau_{env}}$, the pointlike model yields $3.878\tau_{env}$ (%); i.e., the degree of polarization is roughly 30% higher. In this model, the maximum is reached for $\sqrt{\delta_s\tau_{env}} = 3.05$, and is equal to $4.722\tau_{env}$ (%).

When $\sqrt{\delta_s\tau_{env}} \gg 1$ and $N_e \sim r^{-2}$, the polarization is also determined by the outer layer of the envelope ($r \geq r_*$), where $\psi = 0.5\delta(r_*)\tau(r_*) \leq 1$. The optical depth of an envelope with $r \geq r_*$ is $\tau(r_*) = \tau_{env}R_s/r_*$, where $\delta(r_*)$ is the value of the parameter (2) at this boundary. Taking into account the fact that $\delta(r_*) \propto 1/r_*^3$, we obtain $r_* \propto \sqrt{\lambda}$, which means that $p_l \propto 1/\sqrt{\lambda}$. As in the previous case, the polarization for large values of $\sqrt{\delta_s\tau_{env}}$ can be calculated using the polarization for $\sqrt{\delta_s\tau_{env}} = 10$ and the above wavelength dependence. For $\vartheta_m = 90^\circ$, the asymptotic formula is

$$f_Q \approx \frac{0.086}{(\delta_s\tau_{env})^{1/4}} \propto \frac{1}{\sqrt{\lambda}}, \quad \delta_s\tau_{env} \gg 1. \qquad (10)$$

Using the above qualitative derivation of the wavelength dependence for p_l, we can obtain the asymptotic dependence $p_l \propto \lambda^{-2(\nu-1)/(\nu+2)}$ for $N_e \propto r^{-\nu}$.

Since the polarization is determined by the contribution of regions of the envelope that are distant from the star when $\delta_s\tau_{env} \gg 1$, the spectrum and azimuthal angle of the polarization provide information about the density $N_e(\mathbf{r})$ precisely in this part of the envelope. Thus, polarization observations can be used to derive the electron distribution in the envelope (or verify models for this distribution).

3. AN OPTICALLY THICK ENVELOPE

To calculate the integrated polarization due to an optically thick envelope, we must know the intensity I and Stokes parameters Q and U of the radiation emerging from an element of the envelope's surface. We will assume that the sources of the radiation are distant from the outer surface of the envelope, so that I, Q, and U are given by the solution of the classical Milne problem for a semi-infinite plane-parallel atmosphere, taking into account Faraday rotation of the plane of polarization. This problem has been solved numerically only for the case of a magnetic field directed along the normal to the atmosphere [12, 13]. The problem is more complex in the case of an arbitrary direction of the magnetic field, and has not yet been solved. For a dipolar, i.e., inhomogeneous, magnetic field, we must know the solution of the Milne problem for an arbitrary magnetic-field direction.

In [14], simple asymptotic formulas ($\delta \geq 1$) for the Stokes parameters I, Q, and U of radiation emergent from a semi-infinite atmosphere were obtained for a number of problems, including the Milne problem. It is important that these analytical formulas are valid for an arbitrary magnetic-field direction.

The formulas of [14] yield for the Stokes parameters of the integrated radiation from an optically thick spherical envelope:

$$F_I = \frac{a^2}{R^2}F, \qquad (11)$$

$$F_Q = -\frac{a^2}{R^2}\frac{F}{\pi J_1}\frac{1-g}{1+g}\int_0^1 d\mu \qquad (12)$$

$$\times \int_0^\pi d\varphi\mu(1-\mu^2)\frac{(1-k\mu)\cos(2\varphi)}{(1-k\mu)^2 + [(1-q)\delta\cos\Theta]^2},$$

$$F_U = -\frac{a^2}{R^2}\frac{F}{\pi J_1}\frac{1-g}{1+g}\int_0^1 d\mu \qquad (13)$$

$$\times \int_0^\pi d\varphi\mu(1-\mu^2)\frac{(1-q)\delta\cos\Theta\cos(2\varphi)}{(1-k\mu)^2 + [(1-q)\delta\cos\Theta]^2}.$$

Here, F is the flux of radiation emergent from a unit area of the envelope surface, a is the outer radius of the envelope, R is the distance to the observer, and the constants J_1 and g depend on the degree of true absorption $q = \dfrac{\delta_a}{\delta_a + \delta_T}$ and were calculated in [14]. For a dipolar magnetic field, $\delta\cos\Theta$ is

$$\delta\cos\Theta = \delta_0\Big[(3\mu^2-1)\cos\vartheta_m + 3\mu\sqrt{1-\mu^2}\sin\vartheta_m\cos\varphi\Big], \qquad (14)$$

where $\delta_0 = 0.8\lambda^2 M/a^3$ is the parameter (2) at the magnetic equator of the outer surface of a spherical envelope.

Further, we will also consider two cases of a distorted dipolar field: a diamagnetic (ideally conducting) envelope, when the normal component of the field does not penetrate into the medium, and an envelope with a strong radial outflow of plasma. In the latter case, the outflow acquires a radial shape due

to the presence of a frozen-in magnetic field, similar to Parker's spherically symmetrical stellar wind from a nonrotating central source. The envelope can be considered diamagnetic when the ohmic diffusion time ($\tau_{ohm} \approx a^2/6D_m$, where $D_m = c^2/4\pi\sigma$ is the ohmic diffusion coefficient) is substantially shorter than other dynamical time scales—the turbulent mixing time, cyclotron period, etc. [15].

The radial component of the dipolar field is excluded from a diamagnetic envelope. This yields the relations

$$\delta\cos\Theta = \delta_0\Big[-\cos\vartheta_m(1-\mu^2) + \mu\sqrt{1-\mu^2}\sin\vartheta_m\cos\varphi\Big]. \quad (15)$$

On the contrary, in the case of a strong radial outflow, only the radial component of the dipolar magnetic field should remain. Thus,

$$\delta\cos\Theta = 2\delta_0(\mu^2\cos\vartheta_m + \mu\sqrt{1-\mu^2}\sin\vartheta_m\cos\varphi). \quad (16)$$

The cases (14), (15), and (16) are denoted a, b, and c, respectively, in Fig. 2.

For a small depolarization parameter ($\delta_0 \ll 1$) and the most interesting case of a medium without absorption ($q = 0$), expressions (12) and (13) can easily be calculated analytically.

$$p_l \simeq C\delta_0^2\sin^2\vartheta_m, \quad (17)$$

$$\chi \simeq D\delta_0\cos\vartheta_m, \quad (18)$$

where the coefficients C and D are $C = 0.765$, $D = 17.19$ for a complete dipole (14); $C = 0.0797$, $D = -51.56$ for a diamagnetic envelope (15); and $C = 0.319$, $D = 68.75$ for an envelope with a radial outflow (16). Note that the X axis lies in the plane containing the line of sight and the magnetic dipole; therefore, for an observer, positive χ values correspond to a counterclockwise deviation from this plane. If the magnetic dipole points away from the observer ($\vartheta_m > 90°$), the sign of χ is the opposite.

It follows from these formulas that the degree of polarization is $\propto\lambda^4$, while the rotation angle is $\propto\lambda^2$ (as in the case of classical Faraday rotation). A comparison with numerical calculations shows that (17) and (18) remain valid right up to $\delta_0 \simeq 0.25$.

4. DISCUSSION: CALCULATION RESULTS

Figure 2 presents the polarization degree p_l and position angle χ calculated using formulas (11)–(13) as functions of the dimensionless parameter $\sqrt{\delta_0} \cong 0.89\lambda[\mu\mathrm{m}]\sqrt{B_0[\mathrm{G}]}$, where $B_0 = M/a^3$ is the magnetic field at the surface of an optically thick spherical envelope. The parameter $\sqrt{\delta_0}$ was varied from zero to ten. In the case of larger values of $\sqrt{\delta_0}$, the degree of polarization can be extrapolated relatively accurately using the formula $p_l = 100p_l(\sqrt{\delta_0} = 10)/\delta_0$, and the values of the position angles χ for $\sqrt{\delta_0} = 10$ (Fig. 2) can be used.

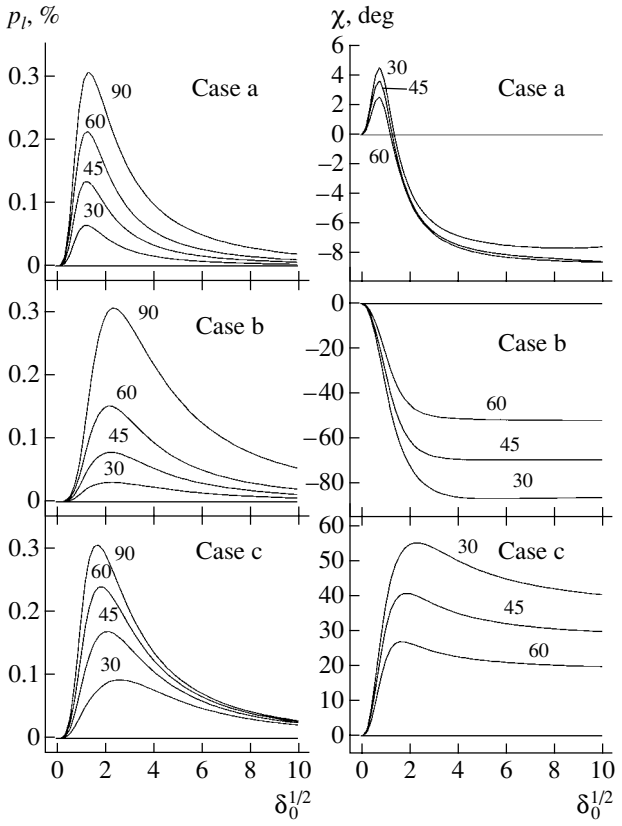

Fig. 2. Degree and position angle of the polarization of integrated radiation from a magnetized, optically thick, spherical envelope for the degree of absorption $q = 0$. The inclination ϑ_m of the magnetic-dipole axis **M** to the line of sight **n** is indicated for each curve (in degrees). See text for details.

The maximum polarization corresponds to the case when the magnetic-dipole axis is perpendicular to the line of sight; then, $\chi = 0$, and the total electric vector of the radiation oscillates in the (**nM**) plane. The asymptotic formula is satisfied when $\delta_0 > 100$ and $q = 0$:

$$p_l \cong \frac{6\%}{n\delta_0} \quad (19)$$

where $n = 3$ corresponds to a total dipole (14), $n = 1$ for a diamagnetic envelope (15), and $n = 2$ for an envelope with a radial outflow (16). The cases $n = 3, 1, 2$ are denoted a, b, and c, respectively, in Fig. 2.

When $\vartheta_m = 90°$, expressions (14), (15), and (16) for $\delta\cos\Theta$ differ only in the coefficients of δ_0 ($n = 3$ for

a total dipole, $n = 1$ for a diamagnetic envelope, and $n = 2$ for an envelope with radial outflow). Therefore, the maximum polarization is the same in all these cases, but p_{max} will correspond to different $\sqrt{\delta_0}$ values due to the differences in the above coefficients. The maximum polarizations for cases (14), (15), and (16) are reached for $\sqrt{\delta_0} = 1.385$, 2.4, and 1.895, respectively. Naturally, p_{lmax} depends on the degree of absorption q. Our calculations indicate that p_{lmax} increases monotonically from 0.307% for $q = 0$ to 1.01% for $q = 0.5$.

It follows from Fig. 2 that the position of the maximum polarization depends weakly on the inclination of the dipole axis to the line of sight. Therefore, we can find an approximate formula for the wavelength λ_{max} at which the maximum polarization is reached that is common for all ϑ_m. When $q = 0$, the above $\sqrt{\delta_0}$ value yields

$$\lambda_{max} \approx \frac{2.68}{\sqrt{nB_0}}\ \mu\mathrm{m}, \qquad (20)$$

where n are the above integer numbers corresponding to the various models. Formula (20) can be used to estimate the magnetic field at the outer surface of the spherical envelope, provided the maximum of the polarization spectrum has been determined. A formula analogous to (20) can be derived for $q \neq 0$. To this end, we must determine $(\sqrt{\delta_0})_{max}$ from the plot for case b, divide it by $\sqrt{0.8} = 0.894$, and substitute this into (20) in place of 2.68. For $q = 0.5$, this yields 2.07 instead of 2.68; i.e., taking absorption into account does not drastically affect the estimate for the magnetic field B_0. Roughly speaking, λ_{max} [μm] $\approx (B_0\,[\mathrm{G}])^{-1/2}$.

Is it possible to deduce from polarization measurements whether the envelope is optically thin or thick? First and foremost, as a rule, the degree of polarization of radiation scattered in an optically thin envelope is appreciably higher than for radiation scattered in an optically thick envelope. However, dilution with unpolarized radiation may reduce this difference. For example, when analyzing the polarization of radiation from active galactic nuclei, dilution of the polarized radiation by unpolarized radiation from stars in the galaxy must be taken into account. Therefore, from this point of view, the spectrum of the polarized radiation, i.e., the wavelength dependence of the degree of polarization, is more informative. Since the optical depth of the envelope can, in principle, depend on the wavelength, a 90° jump in the position angle at a certain wavelength could provide a criterion for identifying the transition between the optically thick and optically thin regimes (see the book [1] in this regard). The polarization of optically thin envelopes is calculated in [8, 9, 11] only for the case of a nondistorted dipolar field (case a in Fig. 2). Therefore, we will restrict our consideration to a comparison of the results obtained in these studies and the upper plots in Fig. 2.

The plots of the degree of polarization in an optically thin envelope resemble the corresponding plots for an optically thick envelope: the polarization first increases $\propto\lambda^4$, reaches its maximum, and then decreases, with the wavelength dependence during the decrease determined by the distribution of free electrons in the envelope. For an envelope with a constant electron density, at longer wavelengths, $p_l \propto \lambda^{-2}$. This coincides with the corresponding asymptotic wavelength dependence in optically thick envelopes. However, the density of free electrons in the envelope is likely to fall off with distance from the central source. If this fall-off is $\propto r^{-2}$, then the decrease of the polarization for the optically thin case is $\propto\lambda^{-1/2}$, whereas the polarization at longer wavelengths is always $\propto\lambda^{-2}$ for an optically thick envelope.

Thus, the polarization spectrum at longer wavelengths can be used to deduce whether the envelope is optically thin or thick.

To estimate the magnetic field B_0 in either type of envelope, the polarization spectrum near the maximum, i.e., near λ_{max}, must be known. Relation (20) should then be used for an optically thick envelope. An analogous expression for an optically thin envelope can be derived from the results of [8, 9]. For the most probable case, $N_e \propto r^{-2}$, the polarization spectrum of an optically thin envelope displays its maximum at the λ_{max} values

$$\lambda_{max} \approx \frac{4.65}{\sqrt{B_s\tau_{env}}} \simeq \frac{4.65}{\sqrt{B_0\tau_{env}}}\frac{R_s^{3/2}}{a^{3/2}}. \qquad (21)$$

Here, $B_s = M/R_s^3$ is the magnetic field at the surface of the central source. The field B_0 for the estimates is obtained from B_s using the law for the fall-off of a dipolar field: $B_0 = B_s R_s^3/a^3$. Since $R_s < a$ and $\tau_{env} \leq 1$, the estimate (21) results in larger λ_{max} values than (20). For large magnetic fields B_0, λ_{max} could fall in the X-ray. If B_0 is known from other considerations, the asymptotic formulas can be used to obtain estimates without knowing λ_{max}.

The spectra of the position angles χ are different for optically thin and thick envelopes. Generally speaking, this provides an additional opportunity to distinguish between these cases. However, if the measured polarization corresponds to long wavelengths, $\delta_0 \gg 1$, then χ is essentially constant and has the same sign in both cases, so that no conclusions can be drawn. The χ spectrum is, however, useful for distinguishing between the optically thick and

thin cases if it is known for wavelengths close to λ_{max}, where the spectra behave substantially differently.

5. SOME ASTROPHYSICAL APPLICATIONS

5.1. Polarization of the Radiation of Hot Stars and Wolf–Rayet Stars: Magnetic Field Estimates

Hot stars display exceptionally intense outflows of matter in the form of a dense stellar wind (with outflow rates $\dot{M} \geq 10^{-5} M_\odot/\mathrm{yr}$) [16–18]. The optical depth of the wind to electron scattering τ can be either smaller (ζ Puppis, Deneb) or larger (P Cyg, WR 40) than unity (see [17]). There has long been interest in determining the magnetic fields at the surfaces of these stars. Underhill and Fahey [19] demonstrated that dipolar magnetic fields can exist at the stellar surfaces.

Numerous attempts to measure the magnetic fields of bright stars using traditional techniques based on circular-polarization measurements have proven unsuccessful (see [16, 20]). In particular, the upper limit $B_{||} \leq 200$ G was obtained for the longitudinal (line-of-sight) component of the magnetic field for the O4I(n)f star ζ Puppis [20]. No appreciable variability of the Stokes parameter V was found. Great hopes are pinned on the future Spectro-Polarimetric INterferometer (SPIN) [17].

We can use our calculations (Figs. 1 and 2) to estimate the expected degree of polarization in the V band for a number of hot stars from the SPIN target list [17]. For an equatorial magnetic field $B_l \approx 10^2$ G, $\delta_0 \approx 0.8\lambda_V^2 B_l \approx 24.2$; if $B_l \approx 10$ G, then $\delta_0 \approx 2.42$. The table presents the calculated expected degrees of linear polarization (for an inclination of $i = 90^\circ$). We assumed the radial dependence of the stellar-wind density to be $N_e \sim r^{-2}$.

Degree of polarization for hot stars for various dipolar magnetic fields (B_l is the field at the equator)

Name of the star	τ_T	P_l, %	
		$B_l = 100$ G	$B_l = 10$ G
ζ Puppis	0.2	0.4	0.02
ε Ori	0.17	0.17	0.01
Deneb	0.03	0.01	$\ll 0.01$
P Cyg	1	0.1	0.3
WR 40	3.4	0.1	0.3

5.2. Polarization of Cyg X-1/HDE 226868

In 1975, Nolt *et al.* [21] detected intrinsic optical linear polarization in the close binary Cyg X-1/HDE 226868, whose compact component is a black hole with a mass of $\sim 10 M_\odot$ [22]. The polarization was variable with an amplitude of $\sim 0.2\%$, and its temporal behavior is rather complex. Along with the periodic dependence with $P = 5.6^\mathrm{d}$, related to the binarity of the system, the polarization also varies with the characteristic times 39^d and 78^d [21]. Possible sources of the polarized radiation of Cyg X-1/HDE 226868 were discussed in [23–25].

If we suppose that the polarization originates during the accretion of matter around the black hole, the intrinsic optical polarization should exceed that observed by Nolt *et al.* [21] by more than an order of magnitude. The degree of polarization decreases due to the strong dilution of the radiation from the accretion structures by radiation from the supergiant HDE 226868, whose luminosity is estimated to be $L_0 \approx (1-3) \times 10^{39}$ erg/s, while the X-ray luminosity of Cyg X-1 is $L_X \leq 8 \times 10^{37}$ erg/s [22]. If we assume that the optical radiation of the accretion disk originates as a result of the reprocessing of X-ray radiation from the accreting black hole, this will specify the expected intrinsic linear polarization of the accretion-disk radiation, $P_l \leq 10\%$. An optically thick accretion disk is unable to provide this degree of polarization for the most probable inclination, $i = 30^\circ$. Therefore, if the polarization originates in the matter being accreted, it can only be due to scattering in an extended optically thin corona or wind material ejected from the accretion disk. At the same time, we cannot rule out the possibility that a small (at the level of several tenths of a percent) amount of intrinsic polarization in HDE 226868 originates due to a magnetized stellar wind.

We will consider both possibilities and their physical consequences.

In the case of an optically thin magnetized corona around the accretion disk, substantial polarization ($P_l \sim 10\%$) can be obtained only from a point source or a very extended corona. In this case, the calculations of Dolginov *et al.* [1] may be used, which indicate that a degree of polarization $P_l \sim 10\%$ can be reached if $\delta_0 \tau_{env} \approx 10$, but only if the magnetic field is perpendicular to the line of sight. For an inclination of $i = 30^\circ$ this means that the magnetic field lies roughly in the plane of the disk. If the optical depth of the hot corona is $\tau_{env} \approx 0.1$, the condition $\delta_0 \approx 10^2$ implies that the magnetic field in the region where the optical radiation is generated is $B \approx 500$ G. In several accretion-disk models, the inner radius of the hot corona is $\sim 10^2 R_g$, where $R_g = 2GM/c^2$ is the

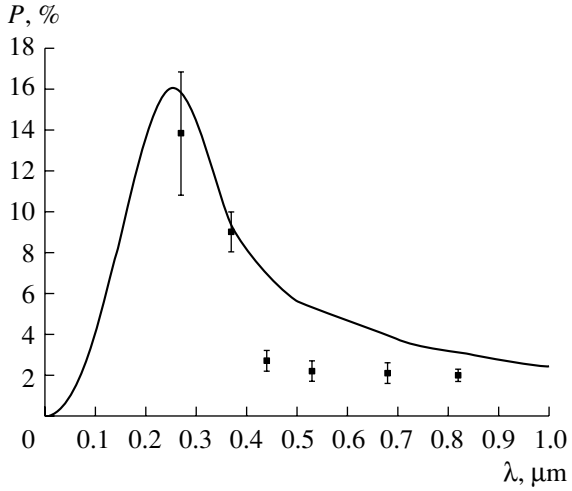

Fig. 3. Wavelength dependence of the degree of intrinsic polarization of the X-ray binary SS 433 compared with calculations for $\tau_T = 1.0$, $B_P = 1$ G, $B_T = 600$ G.

gravitational radius. The dipolar magnetic field near the last stable orbit is then $B(3R_g) \sim 10^7$ G.

Let us now consider the situation when linear polarization is generated in an extended stellar wind from the optical component, HDE 226868. The presence of this wind was confirmed by the detection of an orbital modulation of the radio radiation of Cyg X-1 due to variable absorption of the radio emission of the relativistic jet ejected from near the black hole by the stellar wind during the orbital rotation of the black hole around its optical companion [26].

Assuming that the density of the stellar wind decreases with distance from the star as $n = n_0(R_s/r)^2$ and adopting $\dot{M} \approx 2 \times 10^{-6} M_\odot$/yr, $R_s = 10R_\odot$, and the wind velocity $V_\infty \approx 1850$ km/s [26], we can estimate the optical depth of the stellar wind to electron scattering: $\tau_T \approx 0.1$. In this case, the maximum degree of polarization, $P_l \approx 0.2\%$, corresponds to the case when the angle between the magnetic-dipole axis and the line of sight is $\sim 65°$, with $(\delta_s \tau_{env})^{1/2} \approx 3$ (Fig. 1). We then obtain $B_s \approx 350$ G. Such a magnetic field seems somewhat, but not extremely, high for an OV supergiant. Note that, in this case, the magnetic-dipole axis lies in the orbital plane, and the variability of the polarization can be understood in a natural way.

5.3. Intrinsic Polarization in SS 433

The unique Galactic X-ray binary SS 433 is a microquasar with two strongly collimated ($\vartheta \approx 1°$) relativistic ($V = 0.26c$) jets. The system is characterized by three periodic motions: orbital motion with the period $P_o = 13.082^{\rm d}$, precessional motion with $P_p = 162.5^{\rm d}$, and nutational motion with $P_n = 6.28^{\rm d}$ [22, 27]. Recent spectral observations [28] have confirmed the presence of absorption lines of an A7Ib supergiant. The ratio of the masses of the relativistic component and optical star is estimated to be $q = M_X/M_V = 0.57 \pm 0.11$, while the component masses are $M_V = (19 \pm 7)M_\odot$ and $M_X = (11 \pm 5)M_\odot$ [27]. A kinematic analysis of the relativistic jets was used to determine the inclination of the orbital plane to the line of sight, $i = 78.82° \pm 0.11°$. The precession angle of the disk is $\theta = 19.80° \pm 0.18°$.

The variable (and, hence, intrinsic) linear polarization of SS 433 was first detected by McLean and Tapia [29], and later studied in the $BVRI$ bands at the Crimean Astrophysical Observatory [30]. Polarimetric UV observations of SS 433 were carried out using the high-speed HSP photometer–polarimeter of the Hubble Space Telescope in 1993 [31]. The degree of polarization in the UV reaches $P_l = (13.4 \pm 4)\%$ and is variable. Such a high degree of polarization cannot originate in the accretion disk, and probably results from scattering on electrons in the plasma ejected from the disk (for example, in a dynamical hot corona or wind). Such plasma may also be present in an optically thin advection–accretion flow around the black hole [32].

We have calculated the expected degree of polarization for radiation from a compact magnetosphere around the black hole that has been scattered in a spherically symmetric flow of ejected matter (wind) with a Parker-type magnetic field,

$$B_r = B_p(R_A/r)^2 \cos\theta, \qquad (22)$$
$$B_\varphi = B_T \frac{R_A}{r} \sin\theta, \qquad B_\theta = 0,$$

where B_p is the magnetic field at the pole of the magnetosphere, B_T is the toroidal component of the field, and R_A is the radius of the magnetosphere.

Figure 3 presents the results of calculations of the polarization of radiation scattered in an extended dynamical corona surrounding the black-hole magnetosphere. The calculations were based on the technique of [1, 8–10] (for a compact magnetosphere). Figure 3 also presents the polarimetric observations of Dolan *et al.* [31]. The optical depth of the corona to electron scattering is taken to be close to unity, $\tau_T \leq 1$.

The polarimetric UV observations of SS 433 are in good agreement with the theoretical curve if the radial and toroidal components of the magnetic field at the surface of the magnetosphere are $B_p = 1$ G and $B_T = 600$ G. The differences between the theoretical and observed optical polarizations can, in principle, be understood as a result of dilution of the polarized component by intrinsically unpolarized radiation from

the accretion disk. Although the degree of Thomson polarization of radiation from a disk is fairly high for an inclination of $i \approx 80^\circ$ ($P_l^T \approx 5\%$ [13]), the presence of a strong ($B_T \approx 600$ G) toroidal magnetic field completely depolarizes the radiation scattered in the disk via Faraday depolarization, since the depolarization parameter is $\delta_0 \geq 500(\lambda/1\mu\text{m})^2$ in this case [see (21)].

In principle, the derived components of the magnetic field near the magnetosphere can be used to obtain additional information about the parameters of the accretion onto the black hole.

According to the modern theory of rotating black holes as energy machines, the magnetosphere is the region from which the relativistic jets are ejected and where the hot corona is simultaneously formed [4, 33]. Following [33], the size of this region is $R_A \approx 5 \times 10^3 R_g$ for a purely thermal corona and $R_A \approx 3 \times 10^2 R_g$ for a so-called hybrid corona. As a result, the magnetic field in the immediate vicinity of the black hole near the last stable orbit can be estimated to be $3R_g$, where R_g is the gravitational radius. If we assume that the law (21) for a Parker field remains valid to $3R_g$, we can obtain an estimate for the maximum magnetic field of the black hole in SS 433: $B_{max} \approx 10^4$–10^6 G, depending on the type of the dynamic corona. These values are consistent with those obtained in the model of Blandford and Znajek [4].

Note also that, if we assume the radius of the magnetosphere of SS 433 to be $R_A \approx 10^{10}$ cm, according to [33], the magnetic moment of the compact object in SS 433 will be $\mu \approx 10^{30}$ G cm^3, which is close to that estimated for the microquasar GRS 1915+05 by Robertson and Leuter [2] based on very different considerations.

Finally, if, in accordance with [32], the magnetic-field lines strictly follow the motion of matter in the accretion disk, we can determine the disk viscosity coefficient introduced by Shakura and Sunyaev [34]. According to [32],

$$\frac{B_r}{B_\varphi} = \frac{U_r}{U_\varphi} \approx \alpha, \qquad (23)$$

where U_r and U_φ are the radial and Keplerian velocities of the matter being accreted in the disk.

We can also use our estimates of the components of the magnetic field near the black hole in SS 433 to estimate the parameter $\alpha \approx 2 \times 10^{-3}$, which turns out to be close to the theoretical value obtained by King *et al.* [35].

5.4. Polarization of Supernovae

Numerous recent observations provide evidence that the radiation from supernovae displays appreciable polarization (see the review [36]). Spectropolarimetrical observations of young supernovae obtained with the Keck Telescope have demonstrated that essentially all types of supernovae possess intrinsic polarization [37]. For example, intrinsic polarization was detected in the supernovae 1997dt (Ia), 1998T and 1997dq (both Ib), 1997ef (Ib/c-peculiar), 1997eq (IIn), and 1997ds (II-p) [37]. Type II and Ib/c supernovae have typical polarizations $P_l \approx 1\%$, while some display even higher polarizations [38]. The smaller the size of the hydrogen envelope and the deeper the layers that can be seen in the matter ejected in the explosion, the higher the observed polarization [38]. Such a dependence was also considered by Höflich *et al.* [39]. The degrees of polarization of type II are higher than those of type Ic supernovae.

It is natural to explain the presence of polarized radiation associated with supernovae using the traditional mechanism of scattering of the radiation from the supernova in the symmetrical envelope formed by the ejected matter. This idea has been considered in numerous studies (see, for example, [36]).

Although we agree that this mechanism probably plays a significant role in supernovae, we also wish to point out another physical mechanism that can result in appreciable polarization of the radiation of supernovae without requiring symmetry in the distribution of the ejected matter. We are referring to the integrated effect of the Faraday rotation of the plane of polarization of radiation scattered in the spherically symmetrical envelope formed by the ejected material (shock) in the presence of a magnetic field, which eventually leads to the generation of intrinsic polarization. The magnetic field in the region of propagation of the shock can be estimated in the framework of this model.

Let us consider several examples. The type-II supernova 1999em (with a plateau) was observed 7, 40, 49, 159, and 163 days after the outburst and displayed substantial intrinsic polarization [40]. The measured degree of polarization was $P_l \sim (0.2$–$0.5)\%$, which is consistent with our calculations in Fig. 2; the polarization maximum corresponds to the Faraday-depolarization parameter $\delta_0 \sim 4$, which corresponds to a magnetic field of $B \approx 16.5$ G for V-band radiation ($\lambda_{eff} = 0.55\,\mu$m).

Another example is a spectroscopically normal type-Ia supernova whose intrinsic polarization was $P_l \approx 0.7\%$ [41]. This value is more consistent with the calculations in Fig. 1 for scattering in a magnetized, optically thin envelope. In this case, the depolarization parameter is $(\delta_s \tau)^{1/2}$, where τ is the optical

depth of the envelope. The polarization $P_l \sim 1\%$ corresponds to $\delta_s \tau \sim 1$, and the implied magnetic field is $B_s \sim 4/\tau$ G. If $\tau \approx 0.1$, the magnetic field in the shock region could reach ~40 G, or even ~100 G.

No fundamental difficulty arises when the asphericity of the envelope is taken into account. Some cases of the generation of polarized radiation in a magnetized aspherical envelope are considered in [1, 9].

6. MAIN CONCLUSIONS

We have presented the results of our calculations of the integrated polarization of radiation emitted by an optically thick spherical envelope in the dipolar magnetic field of a central source (neutron star; expanding supernova envelope in the initial stage of expansion, when the matter is optically thick; envelopes around quasars and active galactic nuclei). We have also considered distorted magnetic fields in a diamagnetic envelope and envelope with strong radial outflow. We compared our calculation results with the analogous parameters obtained for an optically thin spherical envelope in a dipolar magnetic field. We have proposed a way to use polarization measurements to determine whether an envelope is optically thin or thick. Ours are the first calculations of the integrated linear polarizations of magnetized, optically thick spherical envelopes, and provide a clear understanding of the polarization degrees and position angles that may be expected in such objects.

Our theoretical results may be applied to analyses of polarimetric observations of hot stars, Wolf–Rayet stars, X-ray binaries, such as Cyg X-1/HDE 226868, SS 433, supernovae, etc. There may also be some applications to the analysis of polarimetric observations of quasars and active galactic nuclei (see [42]). We intend to embark on such a study in the future.

ACKNOWLEDGMENTS

This work was supported by the Russian Foundation for Basic Research (project no. 03-02-17223), the projects of the Presidium of the Russian Academy of Sciences "Non-stationary phenomena in astronomy" and "Extended structures in the Universe," and the Federal Science and Technology Project "Astronomy."

REFERENCES

1. A. Z. Dolginov, Yu. N. Gnedin, and N. A. Silant'ev, *Propagation and Polarization in Cosmic Media* (Nauka, Moscow, 1979; Gordon and Breach, Amsterdam, 1995).
2. S. L. Robertson and D. J. Leiter, Astrophys. J. **596**, L203 (2003).
3. Yu. N. Gnedin, N. V. Borisov, T. M. Natsvlishvili, *et al.*, Izv. Glav. Pulkov. Astron. Obs. **216**, 516 (2002); Astrophys. Space Sci. (in press).
4. R. D. Blandford and R. L. Znajek, Mon. Not. R. Astron. Soc. **179**, 433 (1977).
5. L.-X. Li, astro-ph/0202361.
6. F. M. Rieger and K. Manheim, astro-ph/0011012.
7. A. Tomimatsu and M. Takakashi, Astrophys. J. **552**, 710 (2001).
8. Yu. N. Gnedin and N. A. Silant'ev, Pis'ma Astron. Zh. **6**, 344 (1980) [Sov. Astron. Lett. **6**, 190 (1980)].
9. Yu. N. Gnedin and N. A. Silant'ev, Astrophys. Space Sci. **102**, 375 (1984).
10. N. A. Silant'ev, Yu. N. Gnedin, and T. Sh. Krymski, Astron. Astrophys. **357**, 1151 (2000).
11. M. A. Pogodin, Pis'ma Astron. Zh. **18**, 442 (1992) [Sov. Astron. Lett. **18**, 178 (1992)].
12. E. Agol, O. Blaes, and C. Ionescu-Zanetti, Mon. Not. R. Astron. Soc. **293**, 1 (1998).
13. P. S. Shternin, Yu. N. Gnedin, and N. A. Silant'ev, Astrofiz. **46**, 433 (2003) [Astrophys. **46**, 350 (2003)].
14. N. A. Silant'ev, Astron. Astrophys. **383**, 326 (2002).
15. D. Lai, Astrophys. J. **524**, 1030 (1999).
16. J. Babel and T. Montmerle, Astrophys. J. **485**, L29 (1997).
17. O. Chesneau, S. Wolf, and A. Domiciano de Souza, astro-ph/0307407.
18. M. E. Contreras, G. Montes, and F. P. Wilkin, astro-ph/0310393.
19. A. B. Underhill and R. P. Fahey, Astrophys. J. **280**, 712 (1984).
20. O. Chesneau and A. F. J. Moffat, Publ. Astron. Soc. Pac. **114**, 612 (2002).
21. I. G. Nolt, J. G. Kemp, R. J. Rudy, *et al.*, Astrophys. J. **199**, L27 (1975).
22. A. M. Cherepashchuk, Usp. Fiz. Nauk **171**, 864 (2001) [Phys. Usp. **44**, 821 (2001)].
23. N. G. Bochkarev, E. A. Karitskaya, R. A. Syunyaev, *et al.,* Astron. Zh. **55**, 185 (1979).
24. E. A. Karitskaya, Astron. Zh. **58**, 146 (1981) [Sov. Astron. **25**, 80 (1981)].
25. Yu. N. Gnedin, N. V. Borisov, T. M. Natsvlishvili, M. Yu. Piotrovich, and N. A. Silant'ev, astro-ph/0304158.
26. C. Brocksopp, R. P. Fender, and G. G. Pooley, Mon. Not. R. Astron. Soc. **336**, 699 (2002); astro-ph/0206460.
27. A. M. Cherepashchuk, R. A. Sunyaev, E. V. Seifina, *et al.*, astro-ph/0309140 (2003).
28. D. R. Gies, W. Huang, and M. V. McSwain, Astrophys. J. **578**, L67 (2002).
29. I. S. McLean and S. Tapia, Nature **287**, 704 (1980).
30. Y. S. Efimov, V. Piirola, and N. M. Shakovskoy, Astron. Astrophys. **138**, 62 (1984).
31. J. F. Dolan, P. T. Boyd, S. N. Fabrica, *et al.*, Astron. Astrophys. **327**, 648 (1997).
32. L.-X. Li, astro-ph/0112503.
33. T. J. Maccarone and P. S. Coppi, astro-ph/0204235.
34. N. I. Shakura and R. A. Sunayev, Astron. Astrophys. **24**, 377 (1973).

35. A. R. King, J. E. Pringle, R. G. West, *et al.*, astro-ph/0311035.
36. L. Wang, D. Baade, P. Höflich, *et al.*, Messenger **109**, 47 (2002).
37. D. C. Leonard, A. V. Fillipenko, A. J. Barth, *et al.*, Astrophys. J. **536**, 239 (2000).
38. J. C. Wheeler, P. Höflich, L. Wang, *et al.*, astro-ph/9912080.
39. P. Höflich, J. C. Wheller, and L. Wang, Astrophys. J. **521**, 179 (1999).
40. D. C. Leonard, A. V. Fillipenko, and M. S. Brotherton, Astrophys. J. **553**, 861 (2001).
41. D. Kasen, P. Nugent, L. Wang, *et al.*, astro-ph/0301312.
42. Yu. N. Gnedin and N. A. Silant'ev, Pis'ma Astron. Zh. **28**, 499 (2002) [Astron. Lett. **28**, 438 (2002)].

Translated by K. Maslennikov

Astronomy Reports, Vol. 49, No. 3, 2005, pp. 190–200. Translated from Astronomicheskiĭ Zhurnal, Vol. 82, No. 3, 2005, pp. 219–230.

Properties of Stellar Trajectories in Numerical Dynamical Models of Open Star Clusters

V. M. Danilov and E. V. Leskov

Astronomical Observatory, Ural State University, pr. Lenina 51, Yekaterinburg, 620083 Russia

Received September 20, 2004

Abstract—Stellar trajectories in models of open star clusters that are nonstationary in the regular field of the cluster are analyzed. The maximum characteristic Lyapunov exponents λ of the trajectories of the stellar motions in the open cluster are estimated. The mean λ in the open-cluster models considered are $\overline{\lambda} \simeq 1$ (Myr)$^{-1}$. Cluster cores and halos are regions of highly stochastic and more ordered stellar motions, respectively. The mean Lyapunov exponent, $\overline{\lambda}$, increases with the cluster density, as does the size of the highly stochastic region in the cluster core. The stellar trajectories in phase space are "glued" to a domain with a given λ. A Fourier analysis of the stellar trajectories in the open-cluster models is performed. The distributions of the periods of the stellar trajectories with the highest power-spectrum levels are constructed. The distributions of the periods corresponding to the most significant oscillations of the stellar trajectories exhibit peaks with periods commensurable with (or close to) those of the most significant oscillations of the regular field of the system. Specific features of the distributions of the periods of the most significant oscillations of the stellar trajectories and the origins of the formation of these features in the open-cluster models are discussed. © *2005 Pleiades Publishing, Inc.*

1. INTRODUCTION

Danilov [1, 2] analyzed models of open star clusters that are nonstationary in the regular force field of the cluster, close to gravitational instability, and moving in circular orbits in the gravitational field of the Galaxy. In such systems, small-scale density fluctuations due to stellar encounters can easily be amplified and become large-scale fluctuations. During violent relaxation, $t < \tau_{vr}$, open-cluster models develop steady-state radial oscillations with virtually constant amplitude and period (here t is the time and τ_{vr} is the time scale for violent relaxation). To analyze stellar streams in open-cluster models, Danilov [1] and Danilov and Dorogavtseva [3] performed statistical analyses of small intervals of stellar trajectories, enabling them to estimate the relaxation times for stellar motions in spaces corresponding to a number of parameters of the stellar motions, identify the transfer of energy from large-scale to small-scale stellar motions during periodic variations of the regular field in the model open clusters, etc.

The properties of stellar trajectories in open-cluster models [1, 3] remain poorly understood. Danilov [1] suggested that the number and influence of stochastic stellar trajectories should increase in denser model open clusters (i.e., those with a lower degree of instability in the regular field), probably decreasing the role of barriers in the phase space of such systems and ultimately removing them completely. Our estimates show that the degree of stochasticity of stellar trajectories in cluster models [3] does, in fact, increase in denser models with lower degrees of nonstationarity.

A number of methods have been used to analyze stellar trajectories in models of stellar systems. These include estimation of the characteristic Lyapunov exponents [4–12], Fourier analysis of stellar trajectories [7, 8], the use of trajectory-complexity indices based on analyses of the power spectra of trajectories (two different definitions of the complexity of a trajectory can be found in [4, 11]), Fourier analysis of the divergences of close trajectories, correlation analysis of time series for the stellar coordinates in phase space [13], a geometric method that involves estimation of the Ricci curvature [14], analysis of angular dynamical spectra [15, 16], the use of the ROTOR and spectral distance D between the spectra of two different initial vectors for the deviations of perturbed trajectories from a base trajectory [16], and the use of the surface of a Poincaré section [9], mapping equations [15–18], frequency maps [17, 18], and the fast Lyapunov indicator (FLI) and FLI maps [17]. Two (or more) methods are usually applied simultaneously to analyze the properties of stellar trajectories. In most cases, the above methods have been applied to non-self-consistent, steady-state, collisionless models of stellar systems and clusters. When analyzing systems consisting of N gravitating bodies (see, e.g., [14]),

1063-7729/05/4903-0190$26.00

Table 1. Parameters of the open-cluster models

Model number	R_1/R_2	N_1/N_2	N_1	R_2/R_t	$\langle R\rangle/R_t$	$\langle\delta\alpha/\alpha\rangle$	τ_{vr}	$\overline{\lambda}$
1	0.24	0.25	100	0.9	0.57	0.53 ± 0.09	50	0.79 ± 0.03
2	0.24	0.25	100	0.8	0.51	0.28 ± 0.03	42	0.97 ± 0.04
3	0.34	0.67	200	0.8	0.44	0.15 ± 0.02	42	1.21 ± 0.04
4	0.24	0.25	100	0.7	0.45	0.14 ± 0.02	34	1.25 ± 0.05
5	0.45	1.50	300	0.8	0.40	0.07 ± 0.03	42	1.22 ± 0.07
6	0.63	4.00	400	0.8	0.42	0.06 ± 0.03	42	1.04 ± 0.03

isolated clusters that are (most often) close to virial equilibrium have been considered.

The properties of stellar trajectories in dynamical models of star clusters have been investigated in [7, 9] and [8, 10], in which stationary, collisionless models of star clusters moving in circular orbits about the Galactic center are analyzed. Both Carpintero *et al.* [7] and Muzzio *et al.* [8] pointed out the increase in the fraction of chaotic stellar trajectories in the outer regions of globular-cluster models (see Fig. 6 in [7] and Fig. 1 in [8]; both analyses disregard stellar encounters when estimating the fraction of chaotic trajectories). According to [7], the fraction of chaotic trajectories increases to 50–90% at the cluster periphery. Muzzio *et al.* [8] suggested that the chaotic behavior at the periphery of a cluster is the result of the combined effect of three forces acting on the stars: the gravitational force of the cluster, the centrifugal–centripetal (differential) force, and the Coriolis force.

Here, we include the effect of stellar encounters in our open-cluster models, leading to a higher degree of stochasticity and more complex Fourier spectra of the stellar trajectories in the cluster core compared to the estimates of [7, 9] and [8, 10].

Fourier analyses of stellar trajectories are of considerable importance for determining the role of synchronization of the stellar motions in the formation of the frequency spectrum for oscillatory motions in model open clusters. It is also of interest to analyze the distributions of stellar trajectories in cluster models over the periods with the highest spectral density for a given trajectory (found by analyzing the time dependences of the stellar phase-space coordinates). Such analyses make it possible to identify significant periodicities in the stellar motions and compare the distributions for open-cluster models with different degrees of nonstationarity, enabling studies of how the synchronization of radial motions of stars in clusters affects the motions of stars with frequencies that are incommensurable with the frequency of the radial oscillations.

According to Rabinovich and Trubetskov [19, p. 348], synchronization of oscillations in self-oscillating systems with many degrees of freedom shifts the oscillation frequency and gives rise to a set of frequencies commensurable with the frequency of the synchronous oscillations. If this mechanism contributes to the evolution of model open clusters, its effect should be to enhance the statistically most significant frequencies (and periods) of the stellar motions and lead to the appearance of resonance peaks in the period distributions of the stellar trajectories (i.e., resonances with the radial oscillations of the model cluster). Analysis of the coherence between the phases of the periodic components of the stellar trajectories and the periodic components of oscillations of the regular fields of model clusters is of considerable interest for studies of the synchronization of stellar motions in nonstationary open-cluster models.

Our aim in this paper is to analyze the properties of stellar trajectories in open-cluster models that are nonstationary in the regular force field of the cluster.

2. DESCRIPTION OF OPEN-CLUSTER MODELS

Following [1–3], we consider a cluster of $N = 500$ stars moving about the Galactic center in the plane of the Galaxy in a circular orbit with a radius of 8200 pc. At the initial time $t = 0$, we model the star cluster as a system of two concentric (i.e., with coincident centers of mass) gravitating spheres that simulate a halo and core. We analyzed six open-cluster models, whose parameters are listed in Table 1.

Column 1 in Table 1 gives a number labeling each open-cluster model. In all the open-cluster models considered, the initial ratios R_1/R_2 and N_1/N_2 (columns 2 and 3) obey the relation $R_1/R_2 \simeq 0.39 \times (N_1/N_2)^{0.35}$, which is based on observational data [20], where R_1 and R_2 are the radii of the cluster core and halo and N_1 and N_2 are the number of stars in the cluster core and halo, respectively (the initial N_1 is given in column 4). We set the masses of all stars

equal to $1M_\odot$. As in [1–3], we consider the motions of the cluster stars in a rotating reference frame (ξ, η, ζ) fixed to the cluster center of mass, with the ξ, η, and ζ axes pointing from the cluster center of mass toward the Galactic center, along the direction of the cluster motion in the Galactic plane, and perpendicular to the Galactic plane, respectively. We adopted the model for the Galactic potential of [21]. We used a random number generator to specify the initial positions and velocities of the stars in the model open clusters so that, at $t = 0$, the cluster does not rotate relative to external galaxies and each subsystem (halo and core) has an approximately uniform initial number density of stars in the (ξ, η, ζ) coordinate space. The speeds of stars in cluster subsystem i can be calculated using the formulas

$$V_i = \sqrt{C_i U(r)}, \quad i = 1, 2, \tag{1}$$

where $r = |\mathbf{r}|$ and $V = |\mathbf{v}|$ are the absolute values of the radius vector $\mathbf{r} = (\xi, \eta, \zeta)$ and the velocity vector $\mathbf{v}$ for the motion of the star about the cluster center of mass, $U(r)$ is the gravitational potential of the cluster, and the subscripts $i = 1$, 2 correspond to the cluster core and halo, respectively. We chose the constants C_i so that both the cluster and its subsystems obey the conditions of virial equilibrium at $t = 0$, without including the effect of the gravitational field of the Galaxy [22]. We used a random number generator to specify r and the directions of the vectors $\mathbf{r}$ and $\mathbf{v}$ in the open-cluster models, as is described by Danilov [23] for his cluster model 2. In our computations, we used the units pc, Myr, and $M_\odot$, and smoothed the force functions on the right-hand sides of the equations of motions of the stars (the smoothing technique and smoothing parameter is described in [24]).

Columns 5 and 6 in Table 1 give the initial values of R_2/R_t and $\langle R\rangle/R_t$, where R_t is the cluster tidal-stability radius in the Galactic field computed in accordance with [25] and $\langle R\rangle$ is the average distance of a star from the cluster center.

The degree of nonstationarity of the model open clusters in the regular field is determined by the amplitude of oscillations of the virial coefficient, $\delta\alpha$, where $\alpha = 2E_c/W$, $E_c = T + W$, and T and W are the kinetic and potential energy of the cluster, respectively, without allowance for the gravitational field of the Galaxy (as in [1–3]). The various initial values of R_1/R_2, N_1/N_2, and R_2/R_t in cluster models 1–6 result in various degrees of nonstationarity. Column 7 of Table 1 gives the mean ratios of the amplitudes $\delta\alpha$ of oscillations of the virial coefficient α to the mean value $\alpha = \alpha_v$, averaged over the period P_r for oscillations of the regular field. Models 1–6 are listed in Table 1 in order of decreasing degree of nonstationarity. Column 8 gives the initial value of τ_{vr} and column 9—the mean values $\overline{\lambda}$ of the estimated maximum Lyapunov exponents λ.

3. MAIN FORMULAS AND NOTATION

Chandrasekhar's [26] equations of stellar motion (5.517)–(5.519) can be written in the form

$$\dot\xi_i = u_i, \quad \dot\eta_i = v_i, \quad \dot\zeta_i = w_i; \tag{2}$$

$$\dot u_i = 2\omega v_i - \alpha_1\xi_i + G\sum_{j=1, j\neq i}^{N}(\xi_j - \xi_i)/r_{ij}^3,$$

$$\dot v_i = -2\omega u_i + G\sum_{j=1, j\neq i}^{N}(\eta_j - \eta_i)/r_{ij}^3,$$

$$\dot w_i = -\alpha_3\zeta_i + G\sum_{j=1, j\neq i}^{N}(\zeta_j - \zeta_i)/r_{ij}^3,$$

$$i = 1, \ldots, N.$$

Here, N is the number of stars and ξ_i, η_i, ζ_i and u_i, v_i, w_i are the components of the radius vector $\mathbf{r}_i$ and the velocity vector $\mathbf{v}_i$ of star i (as is noted above, we set the masses of the stars in (2) equal to $1M_\odot$). When linearized in the vicinity of the trajectory of star i, Eqs. (2) lead to variational equations for small (in magnitude) perturbations $\delta\xi_i$, $\delta\eta_i$, $\delta\zeta_i$, δu_i, δv_i, δw_i:

$$\delta\dot\xi_i = \delta u_i, \quad \delta\dot\eta_i = \delta v_i, \quad \delta\dot\zeta_i = \delta w_i, \tag{3}$$

$$\delta\dot u_i = 2\omega\delta v_i - \alpha_1\delta\xi_i + G\sum_{j=1, j\neq i}^{N}[\delta\xi_j - \delta\xi_i - (\xi_j - \xi_i)a_{ij}]/r_{ij}^3,$$

$$\delta\dot v_i = -2\omega\delta u_i + G\sum_{j=1, j\neq i}^{N}[\delta\eta_j - \delta\eta_i - (\eta_j - \eta_i)a_{ij}]/r_{ij}^3,$$

$$\delta\dot w_i = -\alpha_3\delta\zeta_i + G\sum_{j=1, j\neq i}^{N}[\delta\zeta_j - \delta\zeta_i - (\zeta_j - \zeta_i)a_{ij}]/r_{ij}^3,$$

$$a_{ij} = 3((\mathbf{r}_j - \mathbf{r}_i)\delta(\mathbf{r}_j - \mathbf{r}_i))/r_{ij}^2,$$

$$r_{ij}^2 = (\xi_j - \xi_i)^2 + (\eta_j - \eta_i)^2 + (\zeta_j - \zeta_i)^2 + e^2,$$

$$i = 1, \ldots, N,$$

where $e = \text{const}$ is a small, constant term added to the square of the distance between the stars (the smoothing parameter; see [24]); $\alpha_i = \text{const}$, $i = 1, 3$, $\alpha_1 < 0$, $\alpha_3 > 0$; and $\omega = \text{const}$ is the angular velocity of the open cluster about the Galactic center. We determined α_i and ω using the Galactic potential of [21].

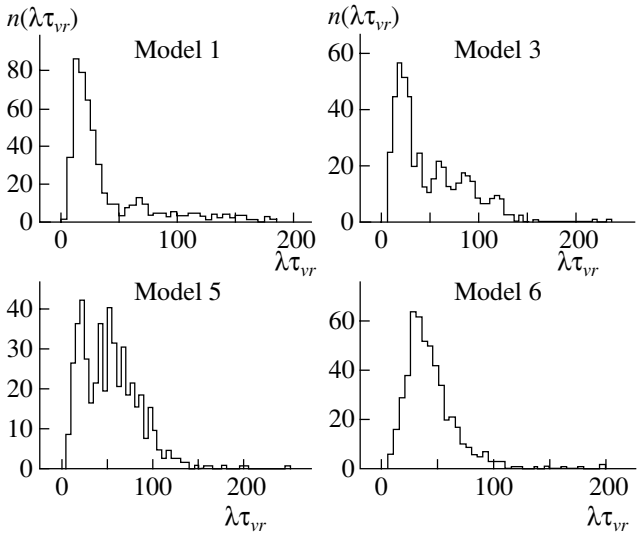

Fig. 1. Distributions of $\lambda\tau_{vr}$ for the stellar trajectories in four model open clusters.

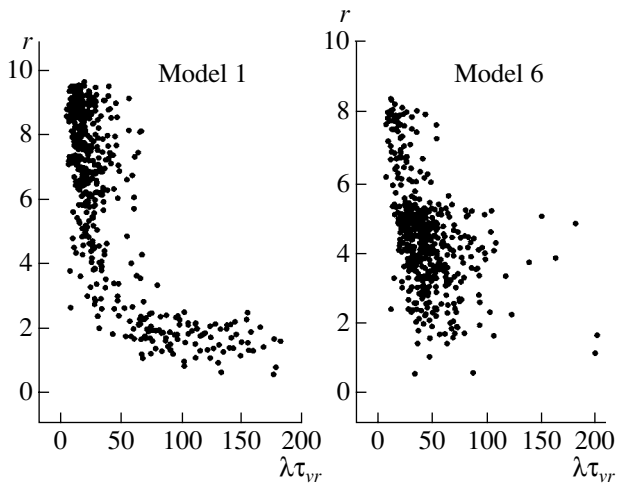

Fig. 2. $(r(0), \lambda\tau_{vr})$ diagrams for the stellar trajectories in two model open clusters.

We numerically integrated the system of equations (2)–(3) in order to compute the stellar trajectories in the open-cluster models and estimate the maximum Lyapunov exponents λ. We estimated λ using the technique described in [27, formula (5.3.10), p. 313]. We chose small values corresponding to $\delta r_i \leq 0.01 r_i$ as the initial values of $\delta\xi_i$, $\delta\eta_i$, and $\delta\zeta_i$; the initial δu_i, δv_i, and δw_i corresponded to $\delta\xi_i$, $\delta\eta_i$, and $\delta\zeta_i$, and were obtained using (1).

4. RESULTS OF THE COMPUTATIONS

We analyzed the stellar trajectories in the six model open clusters whose parameters are listed in Table 1. We estimated the maximum Lyapunov exponents λ of the stellar trajectories and constructed distributions of the stellar trajectories over $\lambda\tau_{vr}$, $n(\lambda\tau_{vr})$ (Fig. 1). The resulting λ for the stellar trajectories can be related to both the initial and final phase-space coordinates of the stars. We accordingly also constructed $(r(t), \lambda\tau_{vr})$ diagrams and families of $\lambda\tau_{vr} = \text{const}$ contours in (r, v) space for two times, $t/\tau_{vr} = 0, 2.6$.

Figure 1 shows the distributions $n(\lambda\tau_{vr})$ for cluster models 1, 3, 5, and 6. The distributions for models 2 and 4 (with $N_1 = 100$ stars in the core) are similar to that for model 1, and so we do not show them here. Most of the stellar trajectories in models 1, 2, and 4 have small positive $\lambda\tau_{vr}$ ($0 < \lambda\tau_{vr} \leq 40$–$50$). In this case, $0 < \lambda < 1$ Myr^{-1}. These λ values correspond to trajectories of stars located far from the cluster center. In model 1, these trajectories have Lyapunov time scales $t_\lambda = \lambda^{-1} \sim 1.2$–$12.5$ Myr. The trajectories of stars in the cluster core have higher λ values, 1 Myr$^{-1} < \lambda < (4$–$5)$ Myr^{-1} and, accordingly, $t_\lambda \sim 0.2$–1.0 Myr.

We used the $\lambda\tau_{vr}$ distributions of the stellar trajectories to compute the mean maximum Lyapunov exponents $\overline{\lambda}$ (and their errors) for the open-cluster models. $\overline{\lambda}$ increases from 0.8 to 1.25 Myr^{-1} with increasing density and decreasing degree of nonstationarity (Table 1). Thus, the degree of stochasticity of the stellar motions in the model open clusters decreases when the amplitudes of the oscillations of the regular field are large (in highly nonstationary systems).

Figure 2 shows $(r(0), \lambda\tau_{vr})$ diagrams for cluster models 1 and 6. The dependences of $r(0)$ on $\lambda\tau_{vr}$ for cluster models 2, 3, and 4 are similar to that for model 1. The distributions of data points on the $(r(0), \lambda\tau_{vr})$ diagrams for models 5 and 6 are also similar to each other. Accordingly, we do not show the $(r(0), \lambda\tau_{vr})$ diagrams for cluster models 2–5.

The domains of model 1 occupied by core and halo stars in Fig. 2 are clearly separated by the line $\lambda\tau_{vr} = 50$. The core size increases with the number of stars in the core, N_1 (from 2.5 pc in model 1 to 5.5 pc in model 6), whereas the boundary $\lambda\tau_{vr}$ separating the trajectories of the core and halo stars in the $(r(0), \lambda\tau_{vr})$ diagram changes only slightly: $\lambda\tau_{vr} \approx 40$–$50$. In models 1–5, the dispersion of λ (and $\lambda\tau_{vr}$) is much higher for trajectories of core stars than for trajectories of halo stars (Figs. 1 and 2). In phase-space domains corresponding to the cluster core, regions with high- and low-stochasticity trajectories can be fairly close to each other (Figs. 2 and 3).

Figure 3 shows families of $\lambda\tau_{vr} = \text{const}$ contours in (r, v) space at two times t for cluster model 1. The

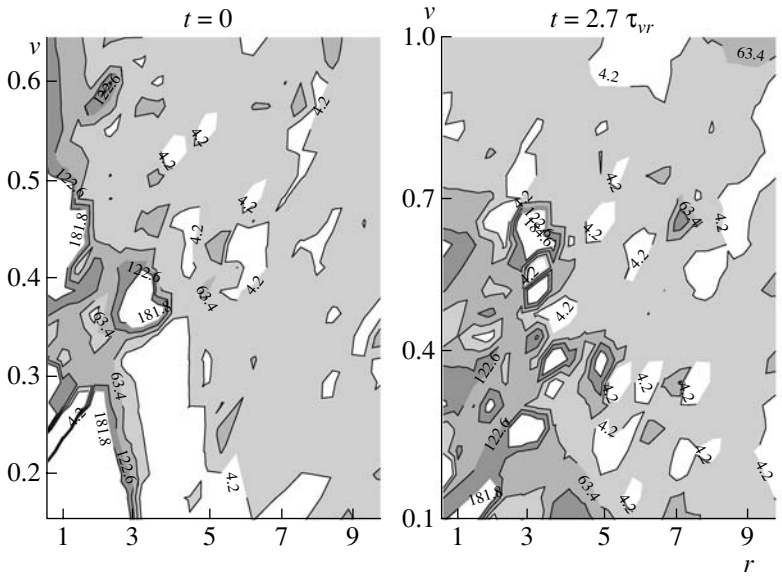

Fig. 3. $\lambda = \text{const}$ contours in (r, v) space at two times t for cluster model 1.

numbers near the contours in Fig. 3 indicate the corresponding $\lambda\tau_{vr}$ values; $\lambda\tau_{vr} \in [4.2, 181.8]$. Empty domains in the (r, v) plane are not occupied by stars at the given time. Darker domains in the (r, v) plane correspond to higher values of $\lambda\tau_{vr}$.

The families of contours $\lambda\tau_{vr} = \text{const}$ for the other cluster models are similar, and we do not show the corresponding plots here. At the initial time, the domain of substantial stochasticity ($\lambda > \overline{\lambda}$) is located in the cluster cores (at small distances r) and in the domain of small and intermediate v. As the model open clusters evolve, the domains of substantial stochasticity propagate toward even smaller values of r and v (Fig. 3). By $t/\tau_{vr} \approx 2.7$–3, narrow regions of low stochasticity penetrate into extended domains of high stochasticity in the cores of the model open clusters in (r, v) space, and small regions of high stochasticity can occasionally be found at the cluster periphery in regions of more ordered motion. In cluster models 1–6, the domains of ordered and stochastic motion are close to each other in (r, v) space.

Thus, the trajectories of stars with high λ are located in the cores of the model open clusters, whereas trajectories with low λ are located (primarily) at the cluster peripheries (Figs. 2 and 3). Therefore, the cores and halos of nonstationary clusters form domains of high stochasticity and of more regular motions, respectively. The domains of high stochasticity are larger in denser model open clusters.

The Lyapunov time scales $t_\lambda = \lambda^{-1}$ that we derived for "outer" stellar trajectories at the cluster periphery are a factor of $\sim$42–83 smaller than the t_λ estimates obtained by Carpintero *et al.* [7] for outer stellar trajectories in non-isolated, collisionless model globular clusters. Thus, allowance for stellar encounters plays an important role in the t_λ estimates, substationally decreasing the t_λ estimates for the model globular clusters.

When computed using the technique of [27, p. 313], λ for each trajectory rapidly increases with time, reaching its maximum at small t and further varying only insignificantly (Fig. 4). It follows that the phase-space trajectories of stars are "glued" to the domain of a given λ.

For each trajectory, we determined the amplitudes A, periods P, and phases Φ of the first three (highest-amplitude) sinusoidal components of the time variations of the phase-space coordinates of the stars. We used the technique described in [28, 29] to extract the sinusoidal components of the variations of the stellar phase-space coordinates. We estimated $q = E_3/E_t$, where E_3 and E_t are the energies of the first three sinusoidal components and of the entire spectrum of $r = r(t)$ for each trajectory. Here and below, we will consider the time dependences of r, $\dot{r}$, θ, ξ, η, and ζ after subtraction of their overall trends, which were determined via third-order, polynomial, and least-squares fits in time intervals $\Delta t = 3\tau_{vr}$. We estimated the energies E_t and E_3 using the temporal representation of the trajectory and its first three sinusoidal components together with formulas (3.20) and (3.30) from [30]. Our estimates indicate that the first three sinusoidal components account for most (up to 95%) of the energy of the spectra. For 75–92% of all the stellar trajectories in cluster models 1–6, the first three sinusoidal components account for

Table 2. P_i, A_i, and $\Phi_i^{(\alpha)}$ for the sinusoidal components of $\alpha(t)$ of the cluster models

Model number	P_1/τ_{vr}	A_1	$\Phi_1^{(\alpha)}$	P_2/τ_{vr}	A_2	$\Phi_2^{(\alpha)}$	P_3/τ_{vr}	A_3	$\Phi_3^{(\alpha)}$
1	0.62	0.1627	120.7°	0.52	0.0251	49.6°	1.12	0.0191	188.3°
2	0.68	0.1338	93.4	0.90	0.0253	215.8	0.59	0.0188	65.9
3	0.64	0.0744	73.9	0.84	0.0183	165.5	1.21	0.0122	271.2
4	0.78	0.0964	103.0	1.05	0.0117	194.2	0.64	0.0103	31.4
5	0.67	0.0336	93.4	1.15	0.0196	204.7	0.37	0.0069	272.1
6	0.58	0.0444	102.9	1.10	0.0441	131.3	0.45	0.0099	275.3

more than 50% of the energy in the spectra of $r(t)$ for the trajectories. Thus, these first three sinusoidal components represent the motions of stars in our open-cluster models well, and also describe fairly well the more ordered motions of stars in the halo. This agrees with the results of Kandrup *et al.* [4], who showed that the complexity of the spectrum of the stellar trajectories (the number of harmonics in the Fourier spectrum with total energies equal to 95% of the total energy in the entire spectrum) in collisionless systems decreases linearly with decreasing maximum Lyapunov exponent [4, Figs. 5, 8].

The values of q for $\alpha(t)$ for cluster models 1–6 lie in the interval $q \in [0.66, 0.93]$. Table 2 gives the parameters of the first three sinusoidal components of $\alpha(t)$ in the open-cluster models.

We constructed diagrams of q vs. $\lambda\tau_{vr}$ for cluster models 1–6. The estimates of q and $\lambda\tau_{vr}$ indicate that in models 2, 3, and 5 with $R_2/R_t = 0.8$, the fraction of trajectories with $q > 0.5$ decreases from 0.81 to 0.76 as the number of stars in the core, N_1, increases from 100 to 300. The values of q for $\alpha(t)$ for cluster models 2, 3, and 5 also decrease, from 0.93 to 0.66. This must be due to the increase in the size of the high-stochasticity domain with increasing N_1 observed for models 2, 3, and 5.

The fraction of trajectories with $q > 0.5$ reaches 0.92 in model 6 with $N_1 = 400$. The value of q for $\alpha(t)$ reaches 0.91 in model 6. Judging from the q estimates for the stellar trajectories in cluster model 6, this is the model with the most regular stellar motion. Note that, during periods when the cluster is concentrated toward the $\zeta = 0$ plane, this model develops a toroidal structure, with an increased stellar number density inside the torus (in ξ, η, ζ space), whose equatorial plane is close to $\zeta = 0$.

For a number of times, we constructed distributions of the stellar number density $\nu(\rho, t)$ projected onto the $\zeta = 0$ plane in the distance ρ from the ζ axis, as well as the radial distributions of the stellar number density $\nu(r, t)$ as a function of r. The $\nu(\rho, t)$ diagrams show density waves propagating across the cluster core away from the ζ axis at velocities comparable to the mean velocity of the peculiar motions of the stars. The amplitude of the oscillations of the density $\nu(\rho, t)$ in the core of model 6 is approximately twice that in the cores of models 1–5. For this reason, at some times, the stellar density $\nu(\rho, t)$ in the $\Delta\rho$ intervals closest to the ζ axis in cluster model 6 can be lower than in $\Delta\rho$ intervals at greater distances from this axis. Cluster models 1–6 show similar density waves in the distributions $\nu(r, t)$.

The fraction of trajectories with $q > 0.5$ increases from 0.75 to 0.85 in models 1, 2, and 4, which have an initial number of stars in the core $N_1 = 100$ and R_2/R_t decreasing from 0.9 to 0.7. The values of q for $\alpha(t)$ for models 1, 2, and 4 also increase from 0.89 to 0.97. We believe this is due to the increase in the

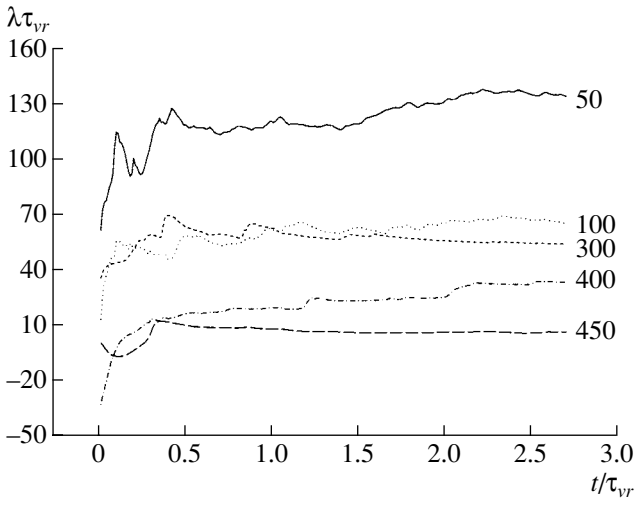

Fig. 4. Dependences of $\lambda\tau_{vr}$ on the time t/τ_{vr} for five stellar trajectories in cluster model 1. The curves are marked by the numbers of stars in the model clusters. For these trajectories, larger numbers correspond to greater mean distances from the cluster center.

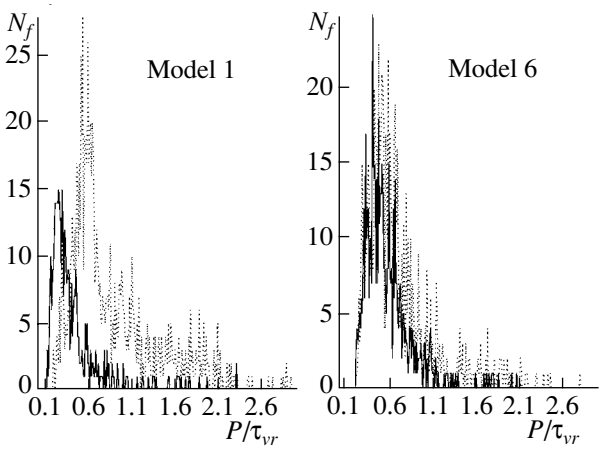

Fig. 5. Total distributions of the stellar trajectories over the periods P of the first three sinusoidal components of $\dot{r}(t)$ in two cluster models. The solid and dashed curves show the distributions of trajectories with $\lambda > \overline{\lambda}$ and $\lambda < \overline{\lambda}$, respectively.

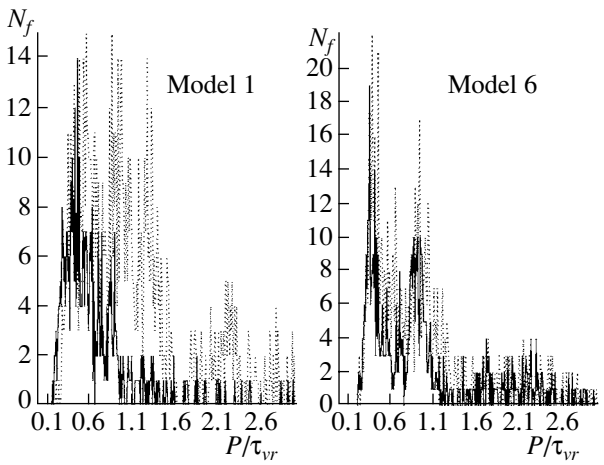

Fig. 6. Same as Fig. 5 for $\theta(t)$.

number of halo-star trajectories associated with the open cluster.

We constructed the total distribution of the trajectories over the periods P of the first three sinusoidal components obtained by analyzing $r(t)$, $\dot{r}(t)$, and $\theta(t)$, where $\dot{r} = dr/dt$ and θ is the angle between the radius vector $\mathbf{r}$ of the star at time t and the positive ζ axis direction. These distributions can be used to estimate the frequencies and phases of the most significant oscillations in the stellar motion. When constructing these distributions, we divided the trajectories into two groups according to their λ values: $\lambda < \overline{\lambda}$ and $\lambda > \overline{\lambda}$. Table 1 lists the $\overline{\lambda}$ values. Figures 5 and 6 show the results of these computations for $\dot{r}(t)$ and $\theta(t)$. Plots of the period distributions of $r(t)$ differ little from those of $\dot{r}(t)$, and we show only the latter distributions here.

The total period distributions of the first three sinusoidal components in the dependences $r(t)$, $\dot{r}(t)$, and $\theta(t)$ exhibit nonrandom and well-defined peaks at points corresponding to (or close to) periods commensurable with the period P_r of the oscillations of the regular field. We determined P_r using the frequency of the first (highest-amplitude) sinusoidal component identified in $\alpha(t)$ using the technique presented in [28, 29]. Table 2 lists the computed parameters of the sinusoidal components of the time variations of the virial coefficients (and regular fields) of the model open clusters.

Trajectories with small P have large λ and are primarily located in the cluster core, whereas trajectories with $P \geq P_r$ have small λ and are primarily located at the cluster periphery. Unlike models 1–5, model 6 exhibits no segregation of trajectories with different λ according to the periods P, and two groups of trajectories with approximately the same proportion of regular and chaotic trajectories form in each ΔP interval.

In cluster model 1 (with the highest degree of nonstationarity), a significant fraction of the stellar trajectories forming the resonance peaks at $t \simeq 3\tau_{vr}$ are located far from the cluster center ($r > R_t$). These trajectories correspond to small λ (Figs. 5 and 6). Oscillations of the regular field probably play an important role in the dissipation of these stars from the cluster.

In the open-cluster models considered, the height (and population) of the resonance peaks in the period distributions for more regular trajectories with $\lambda < \overline{\lambda}$ remains unchanged when $P < P_r$ and decreases with increasing N_1 when $P > P_r$. The number of stars located deep within the tidal surface of the cluster in the gravitational field of the Galaxy ($r \ll R_t$) increases with N_1. The escape energy of these stars increases, so that it takes longer for the system to transfer the energy of oscillations of the regular field to stars, and requires more oscillations of the regular field with period P_r to enable these stars to escape from their clusters and to produce the same population of resonance peaks as for small N_1.

The distributions of $\theta(t)$ over the main oscillation periods P in the open-cluster models form two groups, which are most clearly visible in models 2, 4, and 6; the distribution for model 6 is shown in Fig. 6. In models 2 and 4, these are the groups with periods $P < P_r$ and $P > P_r$, which mostly correspond to cluster stars and stars that have escaped from the cluster to large distances $r > R_t$ in the Galactic plane, respectively. Large values of P for $\theta(t)$ correspond to large r values, and to stellar motions directed primarily along the (ξ, η) plane, in parallel

to the Galactic plane. Ordered ($\lambda < \overline{\lambda}$) and chaotic ($\lambda > \overline{\lambda}$) trajectories in the group with $P < P_r$ are well mixed in the period distribution. Chaotic trajectories are rarely found in models 2 and 4 in the group with $P > P_r$.

The core of cluster model 6 contains two groups of stellar trajectories in the P distributions, obtained by analyzing the $\theta(t)$ dependences (Fig. 6). When $t < 3\tau_{vr}$, the distances r of these stars from the cluster center are smaller than 6 pc. The trajectories of the first group have $P < 0.62\tau_{vr}$, while the trajectories of the second group have P in the interval $P/\tau_{vr} \in [0.62, 1.1]$. In the core of model 6, the first and second group contain both chaotic and more regular trajectories, with the fraction of more regular trajectories (with small λ) in the second group exceeding 0.5 and also exceeding the fraction for the group with $P < 0.62\tau_{vr}$. The model halos are largely dominated by regular motion. According to [1, 3], open-cluster model 6 displays a doubling of the period of large-scale oscillations of the star cluster: $P_r/\tau_{vr} \simeq 0.6$ and $P_{\xi,\eta}/\tau_{vr} \simeq 1.2$); the period $P_{\xi,\eta}$ corresponds to the oscillations in the outer parts of the cluster in the (ξ, η) plane (i.e., the Galactic plane). Model 6 periodically develops a toroidal structure in (ξ, η, ζ) space (see above).

We constructed the total distributions N_Φ of the stellar trajectories over the phases Φ of the first three sinusoidal components of $r(t)$ for cluster models 1–6, using phase intervals $\Delta\Phi = 2°–18°$. The dashed curve in Fig. 7a shows the distribution N_Φ obtained for model 1 for $\Delta\Phi = 18°$. The solid curve in Fig. 7a shows a sixth-order polynomial approximation $\overline{N}_\Phi$, which gives the best rms fit to the $N_\Phi = N_\Phi(\Phi)$ values for $r(t)$.

Note that identifying the sinusoidal components in $r(t)$ using the technique of [28, 29] yields the initial phases $\Phi(0)$. As the cluster evolves, the phases $\Phi(t)$ of oscillations of $r(t)$ increase linearly with time: $\Phi(t) = \Phi(0) + (2\pi/P)t$. The distribution N_Φ of $\Phi(0)$ for $r(t)$ in Fig. 7a is dominated by initial phases close to the initial phase of the oscillations of the regular field of the cluster (i.e., the phase $\Phi_1^{(\alpha)}(0)$ of the first sinusoidal component of $\alpha(t)$ (Table 2)). This coherence between the initial phases of the radial stellar motions and the cluster oscillations is most clearly visible for models 1 and 2, which have a higher degree of nonstationarity.

The vertical line $\Phi_1 = 120.7°$ in Fig. 7a indicates the phase $\Phi_1^{(\alpha)}(0)$, which nearly coincides with the phase of the maximum of the polynomial fit $\overline{N}_\Phi$. Thus, only a small excess of the maximum $\overline{N}_\Phi$ over its minimum value (by approximately eight to nine trajectories in the phase interval $\Delta\Phi = 18°$) reflects the

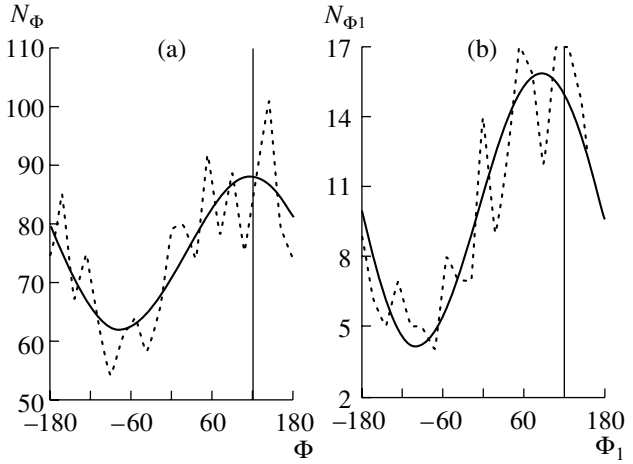

Fig. 7. (a) Total distribution N_Φ for the trajectories for cluster model 1 over the initial phases Φ of the first three sinusoidal components of $r(t)$. (b) Distribution N_{Φ_1} of the trajectories of halo stars in cluster model 1 over the initial phases Φ_1 of the first sinusoidal component of $r(t)$.

tendency of the system toward in-phase radial motions of stars. The number of trajectories with phases $\Phi(0)$ differing by less than 90° from $\Phi_1^{(\alpha)}(0)$ exceeds the number of other trajectories by only about 10%. This is, to a large extent, due to the way we specified the initial velocities in our models (all initial directions of $\mathbf{v}$ are equally probable). In this case, the phases of radial motion of the stars have an approximately uniform distribution. The stochasticity of the stellar trajectories (all $\lambda > 0$) and the random nature of stellar encounters contribute significantly to the uniformity of the distribution of the current phases of $r(t)$.

The coherence of the initial phases of the radial motions increases appreciably for halo stars. We identified the trajectories of halo stars as those having $\lambda < \overline{\lambda}$, $q > 0.5$, and maximum distances $r_{\max}$ not exceeding 20 pc during the evolution of the cluster. The dashed curve in Fig. 7b shows the distribution of the halo-star trajectories, N_{Φ_1}, over the phases of the first sinusoidal component in cluster model 1. The solid curve shows the sixth-degree polynomial $\overline{N}_{\Phi_1}$ giving the best rms fit of the $N_{\Phi_1} = N_{\Phi_1}(\Phi_1)$ values for $r(t)$. We used the standard phase interval $\Delta\Phi_1 = 18°$. The excess of the maximum of the polynomial fit $\overline{N}_{\Phi_1}$ over its minimum value in model 1 is approximately 12 trajectories in the phase interval $\Delta\Phi_1 = 18°$. In terms of percentages, this is appreciably higher than for all the stellar trajectories of the cluster model, since the trajectories of only 203 stars in model 1 satisfy the conditions $\lambda < \overline{\lambda}$, $q > 0.5$, and $r_{\max} < 20$ pc. In this case, the number of halo-star trajectories with phases $\Phi_1(0)$ differing by less than 90° from $\Phi_1^{(\alpha)}(0)$ is about

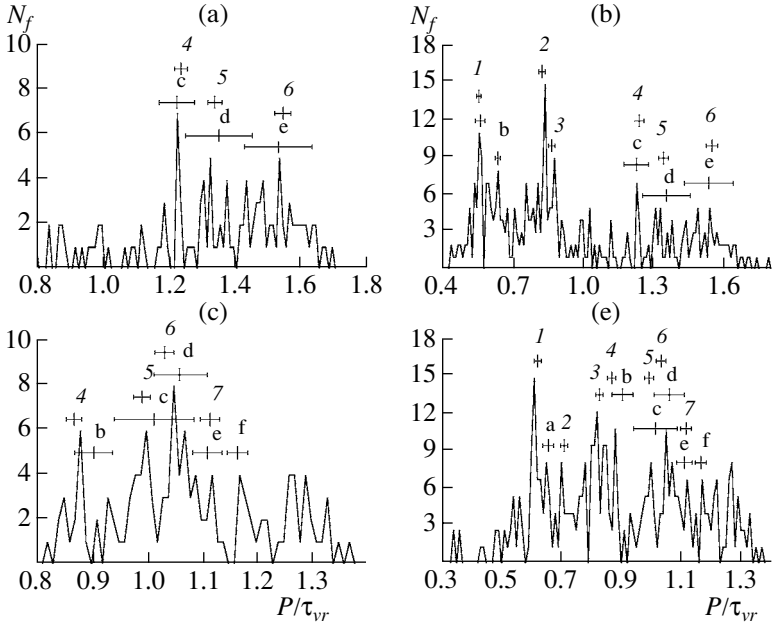

Fig. 8. Distributions N_f of the trajectories of halo stars in cluster model 1 over the periods P. Plots (a) and (b) show the distributions for the first and the first three sinusoidal components of $\eta(t)$, respectively. Plots (c) and (e) show the corresponding distributions for $\zeta(t)$. See text for explanations of curve notation.

38% higher than the number of remaining halo-star trajectories.

For a good fraction of the trajectories, the amplitudes of the stellar radial motions can increase at some times (and during some time intervals) due to the closeness of the phases of the first two sinusoidal components of $r(t)$ for these trajectories. The number of dependences $r(t)$ for which the current phases $\Phi(t)$ of the first two (among the first three) sinusoidal components differ by no more than $\Delta\Phi = 18^\circ$ is, on average, 30% of the total number of trajectories in cluster model 1, with this fraction reaching 50% at some times. The fraction of trajectories with close current phases of two (among the first three) sinusoidal components increases with increasing interval $\Delta\Phi$.

We constructed the distributions of the halo-star trajectories in cluster model 1 over the periods P of the first sinusoidal component of $\xi(t)$, $\eta(t)$, and $\zeta(t)$, as well as the analogous period distributions for the first three main sinusoidal components. When constructing these dependences, we used, in addition to the criteria for the selection of halo-star trajectories described above, the additional constraint $E_{tr} < 0.3(E_t + E_{tr})$, where E_{tr} is the energy corresponding to the trend of $r(t)$. This constraint enables us to exclude the trajectories of halo stars that departed to distances far beyond the tidal radius of the cluster during the time $3\tau_{vr}$ and then returned. The numbers in Fig. 8 indicate the periods P corresponding to the highest peaks in the distributions and the lowercase letters the theoretical estimates of these periods obtained in [31] (here and below, P is in fractions of τ_{vr}). The period of the variations of the regular cluster field is $P_r = 2\pi/\omega_r = 0.620 \pm 0.010$ (ω_r is the frequency of oscillations of the regular field). We find for $\eta(t)$: $P_a(5\nu_1) = 0.564 \pm 0.018$, $P_1\left(\frac{9}{10}\omega_r\right) = 0.568 \pm 0.009$, $P_b(2\nu_1 + \nu_2) = 0.638 \pm 0.011$, $P_2\left(\frac{3}{4}\omega_r\right) = 0.827 \pm 0.013$, $P_3\left(\frac{5}{7}\omega_r\right) = 0.868 \pm 0.014$, $P_b(\beta_3 - 2\nu_2) = 1.228 \pm 0.053$, $P_4(2\omega_r) = 1.240 \pm 0.020$, $P_5\left(\frac{13}{6}\omega_r\right) = 1.343 \pm 0.022$, $P_c(2\beta_3 - 3\nu_1) = 1.356 \pm 0.102$, $P_d(-3\nu_1 + 2\nu_2) = 1.536 \pm 0.104$, and $P_6\left(\frac{5}{2}\omega_r\right) = 1.550 \pm 0.025$, where ν_1, ν_2, and β_3 are the eigenfrequencies of the motion of a halo star in the total field of the Galactic potentials produced by a uniform ellipsoidal cluster approximating the potential of the halo in cluster model 1 averaged over the period P_r. The horizontal period error bars in Fig. 8 correspond to the errors in the approximation of the potential of the uniform gravitating ellipsoid [31] averaged over the period P_r (if Latin letters are used) or the error in P_r derived in this paper (if numbers are used).

We find for $\zeta(t)$: $P_1(\omega_r) = 0.620 \pm 0.010$,

$P_a(-\beta_3 + 2\nu_2 + 2\nu_1) = 0.656 \pm 0.018$, $P_2\left(\frac{7}{8}\omega_r\right) = 0.709 \pm 0.011$, $P_3\left(\frac{3}{4}\omega_r\right) = 0.827 \pm 0.013$, $P_4\left(\frac{5}{7}\omega_r\right) = 0.868 \pm 0.014$, $P_b(3\nu_1 - \nu_2 + \beta_3) = 0.904 \pm 0.035$, $P_5\left(\frac{5}{8}\omega_r\right) = 0.992 \pm 0.016$, $P_c(3\beta_3 - 2\nu_2) = 1.014 \pm 0.073$, $P_6\left(\frac{3}{5}\omega_r\right) = 1.033 \pm 0.017$, $P_d(-\nu_2 + 2\beta_3) = 1.060 \pm 0.051$, $P_e(\beta_3) = 1.111 \pm 0.027$, $P_7\left(\frac{5}{9}\omega_r\right) = 1.116 \pm 0.018$, and $P_f(\nu_2) = 1.166 \pm 0.019$.

Six to fifteen halo-star trajectories in cluster model 1 are grouped at or near these periods. The periods that we give here are commensurable or nearly commensurable with P_r.

Note that the stellar phase-space coordinates at $t = 0$ are random quantities obtained using continuous phase-space distributions for the core and halo stars. Stellar encounters in the cluster are also random in nature. It is therefore reasonable to expect that the frequencies and amplitudes of the stellar motions in the system should also be random and continuously distributed quantities. However, the distributions of the periods P of the trajectories exhibit resonance peaks. The most likely origin of the formation of such groups of trajectories is a "frequency shift" during the synchronization of the oscillations, as has been described for self-oscillating systems with many degrees of freedom [19, p. 348]. Such synchronization leads to the development of a set of frequencies that are commensurable with ω_r, at some of which synchronous motion (with the same frequency) of small groups of stars along their trajectories arises spontaneously. In this case, a set of intervals of radial distances for preferred motions of halo stars is likely to form in the system.

5. CONCLUSIONS

(1) We have analyzed here the trajectories of stellar motions in six model open clusters moving in circular orbits in the Galactic plane and nonstationary in the regular-force field. We estimated the maximum characteristic Lyapunov exponents λ for stellar trajectories in these open-cluster models. The mean Lyapunov exponents $\overline{\lambda}$ increase with increasing density and decreasing degree of nonstationarity of the model clusters, from 0.8 to 1.25 Myr^{-1}. Thus, the degree of stochasticity of the stellar motions in the model open clusters decreases when the amplitudes of the oscillations of the regular field are large (in strongly nonstationary systems).

(2) Stellar trajectories with high λ values are located in the cores of the model open clusters, whereas trajectories with low λ are located (primarily) at the cluster peripheries. Thus, in nonstationary open clusters, the cores and halos form domains of high stochasticity and ordered stellar motion, respectively. The size of the domain of stochasticity in the core increases in denser model clusters. During the evolution of the model open clusters, the regions of significant stochasticity propagate toward smaller r and v. Domains of regular and stochastic motions can be adjacent to each other in (r, v) space.

(3) The estimated λ for each stellar trajectory increases rapidly with time, reaching its maximum value at small t and further varying only insignificantly. Thus, stellar trajectories in phase space are "glued" to the domain with the given λ.

(4) We analyzed the amplitudes, phases, and periods of the three sinusoidal components with the highest amplitudes for the stellar trajectories for the six open-cluster models. We suggest using the parameter q (the ratio of the energy contained in these three sinusoidal components to the total energy in the Fourier spectrum of the trajectory) to analyze the properties of trajectories. The combined use of λ and q enables a more accurate separation of ordered and stochastic trajectories. Overall, the value of q for the dependence $\alpha(t)$ characterizes the complexity of the spectra of all the trajectories in the open-cluster model.

(5) In cluster models 1–5, trajectories with short periods P have high λ and are located primarily in the cluster core; trajectories with low λ have long P and are located primarily at the cluster periphery. Cluster model 6 shows no segregation of trajectories with different λ values in P, probably due to the formation of a toroidal structure in the distribution of stars in (ξ, η, ζ) space in this model.

(6) The distributions of the periods of the most significant oscillations of the stellar trajectories in the cluster models show nonrandom, well-defined peaks at periods P that are commensurable (or close to commensurable) with the period P_r of oscillations of the regular field of the cluster. The periods P corresponding to these peaks derived from the trajectories agree with the theoretical estimates of Danilov [31].

(7) A significant fraction of stars forming resonance peaks in cluster model 1, which has the highest degree of nonstationarity, are located at greater radial distances ($r > R_t$) by the end of the computations (at $t = 3\tau_{vr}$). Oscillations of the regular field of the cluster may play an important role in the dissipation of these stars from the cluster. Cluster models with

higher degrees of nonstationarity also exhibit higher coherence between the initial phases of the radial motions of stars along their trajectories and oscillations of the cluster.

REFERENCES

1. V. M. Danilov, Astron. Zh. **79**, 986 (2002) [Astron. Rep. **46**, 887 (2002)].
2. V. M. Danilov, Astron. Zh. **79**, 492 (2002) [Astron. Rep. **46**, 443 (2002)].
3. V. M. Danilov, Astron. Zh. **80**, 526 (2003) [Astron. Rep. **47**, 483 (2003)].
4. H. E. Kandrup, B. L. Eckstein, and B. O. Bradley, Astron. Astrophys. **320**, 65 (1997).
5. S. Habib, H. E. Kandrup, and M. E. Mahon, Astrophys. J. **480**, 155 (1997).
6. H. E. Kandrup, Mon. Not. R. Astron. Soc. **301**, 960 (1998).
7. D. D. Carpintero, J. C. Muzzio, and F. C. Wachlin, Celest. Mech. Dyn. Astron. **73**, 159 (1999).
8. J. C. Muzzio *et al.*, Celest. Mech. Dyn. Astron. **81**, 167 (2001).
9. D. D. Carpintero *et al.*, Celest. Mech. Dyn. Astron. **85**, 247 (2003).
10. J. C. Muzzio and M. E. Mosquera, Celest. Mech. Dyn. Astron. **88**, 379 (2004).
11. H. E. Kandrup and I. V. Sideris, Celest. Mech. Dyn. Astron. **82**, 61 (2002).
12. N. D. Caranicolas and Ch. L. Vozikis, Astron. Astrophys. **349**, 70 (1999).
13. Ch. L. Vozikis, M. Varvoglis, and K. Tsiganis, Astron. Astrophys. **359**, 386 (2000).
14. A. A. El-Zant, Astron. Astrophys. **331**, 782 (1998).
15. C. Efthymiopoulos, G. Contopoulos, and N. Voglis, Celest. Mech. Dyn. Astron. **73**, 221 (1999).
16. N. Voglis, G. Contopoulos, and C. Efthymiopoulos, Celest. Mech. Dyn. Astron. **73**, 211 (1999).
17. E. Lega and C. Froesle, Celest. Mech. Dyn. Astron. **81**, 129 (2001).
18. Y. Papaphilippou and J. Laskar, Astron. Astrophys. **307**, 427 (1996).
19. M. I. Rabinovich and D. I. Trubetskov, *Introduction to the Theory of Oscillations and Waves* (Nauchno-Izdatel'skiĭ Tsentr "Regulyarnaya i Khaoticheskaya Dinamika," Moscow–Izhevsk, 2000).
20. V. M. Danilov and A. F. Seleznev, Astron. Astrophys. Trans. **6**, 85 (1994).
21. S. A. Kutuzov and L. P. Osipkov, Astron. Zh. **57**, 28 (1980) [Sov. Astron. **24**, 17 (1980)].
22. V. M. Danilov, Astron. Zh. **65**, 716 (1988) [Sov. Astron. **32**, 374 (1988)].
23. V. M. Danilov, Astron. Zh. **77**, 345 (2000) [Astron. Rep. **44**, 298 (2000)].
24. V. M. Danilov, Astron. Zh. **74**, 188 (1997) [Astron. Rep. **41**, 163 (1997)].
25. I. R. King, Astrophys. J. **67**, 471 (1962).
26. S. Chandrasekhar, *Principles of Stellar Dynamics* (Univ. of Chicago, Chicago, 1942; Inostrannaya Literatura, Moscow, 1948).
27. A. J. Lichtenberg and M. A. Lieberman, *Regular and Stochastic Motion* (Springer, New York, 1982; Mir, Moscow, 1984).
28. D. D. Carpintero and L. A. Aguilar, Mon. Not. R. Astron. Soc. **298**, 1 (1998).
29. J. Laskar, Astron. Astrophys. **198**, 341 (1988).
30. J. Max, *Methodes et Techniques de Traitement du Signal et Applications aux Mesures Physigues* (Masson, New York, 1981; Mir, Moscow, 1983), Vol. 1.
31. V. M. Danilov, Astron. Zh. (2004) (in press).

Translated by A. Dambis

Astronomy Reports, Vol. 49, No. 3, 2005, pp. 201–216. Translated from Astronomicheskiĭ Zhurnal, Vol. 82, No. 3, 2005, pp. 231–246.

Analysis of the Dynamic Stability of Selected Multiple Stars with Weak Hierarchy

V. V. Orlov[1] and R. Ya. Zhuchkov[2]

[1] *Sobolev Astronomical Institute, St. Petersburg State University, Universitetskiĭ pr. 28, St. Petersburg, Peterhof, 198504 Russia*

[2] *Kazan State University, Kazan, Russia*

Received April 22, 2004; in final form, July 15, 2004

Abstract—The stability of multiple systems with known orbital elements and with subsystems occupying adjacent hierarchy levels is analyzed using six stability criteria and numerical simulations of their dynamical evolution. All the stability criteria considered are in qualitative agreement with the numerical computations. Of the 16 systems studied, 11 are confirmed to be stable and five (HD 40887, HD 136176, HD 150680, HD 217675, and HD 222326) may be unstable on time scales of $\sim 10^6$ yr or less. The small dynamical ages of the unstable systems may indicate that they have captured components during encounters between close binaries and field or moving cluster stars. The instability could also result from the perturbation of a stable system when it approaches a massive object (star, black hole, or molecular cloud). It is possible that some of the unstable systems are remnants of small clusters or stellar groups. © *2005 Pleiades Publishing, Inc.*

1. INTRODUCTION

Multiple stars with $N_c \geq 3$ components make up a substantial fraction (about 10%) of the stellar population of the Galaxy [1, 2]. These stars are traditionally subdivided into two groups: (1) hierarchical systems, in which no three or more components all have comparable separations, and (2) trapezium-type systems, which contain components with comparable separations. Hierarchical systems whose outer-subsystem orbits are not too elongated are usually stable, although the motions of stars in such systems are subject to periodic and secular perturbations (e.g., the Kozai [3] and other related effects [4, 5]). On the whole, the system maintains its hierarchy during its dynamical evolution. Trapezium-type systems, on the contrary, are dynamically unstable and become disrupted on time scales equal to $\sim 10^1 - 10^3$ of the mean crossing time [6, 7]. The hierarchical nature of a multiple system's structure does not guarantee by itself the stability of the system. The reason is that individual components in unstable systems can be ejected to large distances [6]. During ejection, the multiple system has a hierarchical structure, but it will later be disrupted.

All known multiple systems with measured orbital motions are hierarchical systems. However, several systems with only weak hierarchy can be found, in which the size of the inner subsystem is not negligible compared to the distance between this subsystem and the outer body. The analysis of the stability of such systems is of considerable interest.

There are at least two approaches to investigating this problem. In the first, the motion of the system is analyzed using analytical or empirical stability criteria. The second approach involves carrying out numerical simulations of the dynamical evolution of a system by numerically integrating the equations of motion. In the latter case, we must know the masses, coordinates, and velocities (or orbital elements) of all bodies of the system at some time, whereas, in the former case, it is sufficient to know the parameters used by the stability criteria employed and their critical values.

Various authors have analyzed the stability of observed multiple systems [8–11]. Szebehely and Zare [8] and Fekel [9] found most of the systems they studied to be stable, and some to be possibly unstable within certain intervals of the mutual inclination of the orbital planes, which are not known with the required accuracy. Donnison and Mikulskis [10] showed that the motions of all the systems they studied are stable according to the criterion employed. However, this paper contains a number of typographical errors and errors in the adopted orbital elements and masses, many of which have been later redetermined. Moreover, the authors of these three papers do not analyze the effect of the errors in the initial data on the result, whereas this can play an important role, especially near the stability limit.

Orlov and Petrova [11] estimate four stability parameters together with their critical values and the errors in these quantities. The results suggest that

1063-7729/05/4903-0201$26.00

some of the observed systems may be unstable. A firm interpretation of these results requires further analysis, in particular, numerical simulations of the dynamical evolution of multiple systems that are near the stability limit. In addition, new observational data for some multiple stars have been obtained recently, making new dynamical studies of these systems of interest.

We conclude our summary of current and past studies concerning the instability of observed multiple systems by noting the study of Loinard *et al.* [12], who were the first to observationally confirm the ejection of one of the components in the T Tauri multiple system.

2. CRITERIA FOR STABILITY AND ESCAPE

A number of analytical and empirical criteria for the stability of triple systems are available. Descriptions of the criteria of Golubev [13, 14], Harrington [15, 16], Eggleton and Kiseleva [17], and Mardling and Aarseth [18] are presented in the original papers, as well as by Orlov and Petrova [11], and we do not repeat them here.

Another criterion proposed by Valtonen and Kartunen [19] is based on the theory of perturbations in the three-body problem. It has the form

$$Q = \frac{a_{out}(1-e_{out})}{a_{in}} > Q^{critical}, \qquad (1)$$

where

$$Q^{critical} = 3.6\left(1+\frac{m_3}{m_1+m_2}\right) \qquad (2)$$
$$\times (1-e_{out})^{-1/11}\left(1+e_{in}^2/2\right)$$
$$\times \left[0.07+(1+\cos i)^{1.15}\right]^{1/6}.$$

Here, a_{out} and a_{in} are the semimajor axes of the orbits of the outer and inner pairs, e_{out} and e_{in} are the eccentricities of these orbits, m_1 and m_2 are the masses of the two components in the inner pair, m_3 is the mass of the distant body, and i is the angle between the orbital angular momenta of the inner and outer binaries.

We also used the empirical criterion of Tokovinin [20]:

$$T = \frac{P_{out}(1-e_{out})^3}{P_{in}} > T^{critical}, \qquad (3)$$

$$T^{critical} = 5. \qquad (4)$$

Here, P_{out} and P_{in} are the orbital periods of the outer and inner pairs.

In addition to quantities characterizing the stability of the system proper, following Orlov and Petrova [11], we introduce the following parameter characterizing the margin of stability possessed by a system:

$$\delta_i = \frac{\alpha_i - \alpha_i^{critical}}{\alpha_i^{critical}}, \qquad (5)$$

where $\alpha_i^{critical}$ is the value of the parameter corresponding to the stability limit and α_i is the observed value. Both quantities are calculated for a system based on observational data—the component masses and orbital elements of the inner and outer binaries.

We used the criterion of Griffith and North [21] to identify the state of disruption in our numerical simulations of the evolution of triple systems.

3. FORMULATION OF THE PROBLEM

Our aim was to analyze the stability of triple and higher-multiplicity systems with known orbital parameters and with subsystems having adjacent hierarchy levels using both the stability criteria listed above and numerical simulations of the component motions. We numerically integrated the equations of motion using the TRIPLE code developed by Sverre Aarseth (Institute of Astronomy, University of Cambridge, United Kingdom), which applies the technique for regularizing close encounters developed by Aarseth and Zare [22]. We modified the code slightly to adapt it to our particular needs.

Our stability analysis can be divided into several main stages.

(1) Selecting systems with known orbital parameters for the inner and outer binaries and known stellar masses.

(2) Partitioning the sample into groups according to multiplicity and the degree of closeness of the inner binary.

(3) Computing the parameters and margin of stability based on the listed criteria, and identifying possible unstable systems.

(4) Computing the dynamical evolution of the candidate unstable systems via numerical integration of their equations of motion.

(5) Analyzing each system to determine whether or not it is dynamically stable.

Since all the known parameters of stellar systems are subject to errors, more trustworthy conclusions can be reached if the component motions in multiple systems are analyzed allowing for the errors in the observational data. We plan to carry out such an analysis in a future study; the current paper should be regarded as the first part of a more general study.

Table 1. Parameters of multiple systems with known orbital elements of subsystems occupying adjacent hierarchy levels and their errors. The systems are listed in order of right ascension

System (HD, IDS) Level of hierarchy	P, yr σ_P	T_0, yr σ_{T_0}	e σ_e	a, arcsec σ_a	Ω, deg σ_Ω	ω, deg σ_ω	i, deg σ_i	M_1, $M_\odot$ σ_{M_1}	M_2, $M_\odot$ σ_{M_2}	References
5408										
00508+5949										[23, 24]
1	83.1	1952.31	0.241	0.245	175.0	333.19	54.9	8.25	5.0	
	±0.2	±0.09	±0.002	±0.002	±0.3	±0.33	±1.1	±0.80	±0.5	
11	4.84	1984.1	0.23	0.034	185	290	55	5.65	2.6	
	0.03	0.1	0.03	0.002	10	9	5	0.60	0.2	
9770										
01304−3026										[25]
1	112	1960	0.21	1.420	142	65	29	2.22	0.38	[26]
	11	11	0.10	0.015	10	10	10	0.21	0.10	
11	4.6	1991.9	0.33	0.17	158	307	22	1.44	0.78	[27]
	0.4	0.4	0.10	0.01	10	10	10	0.15	0.10	
9770										
01304−3026										[25]
1	112	1960	0.21	1.419	142	65	29	2.22	0.38	[26]
	11	11	0.10	0.015	10	10	10	0.21	0.10	
11	4.6	1932.6	0.30	0.178	57	51	22	1.44	0.78	[28]
	0.4	0.4	0.10	0.010	10	10	10	0.15	0.10	
12376										
01562+3614										[25]
1	330	1907	0.33	1.13	159	174	140	2.10	0.49	[29]
	33	33	0.10	0.11	10	10	10	0.21	0.10	
11	12.94	1989.06	0.404	0.150	191.4	295.1	67.0	1.32	0.78	[30]
	0.04	0.03	0.007	0.001	0.5	0.7	0.5	0.15	0.15	
29316										
04320+5316										[24, 31]
1	430	2033	0.32	1.36	112	327	133.0	3.0	1.17	
	5	2	0.02	0.02	3	4	1.5	0.2	0.12	
11	27	1988.9	0.86	0.17	21	52	141	1.86	1.14	
	2	0.6	0.06	0.10	10	10	10	0.19	0.11	
29316										
04320+5316										[31]
1	430	2033	0.32	1.36	112	327	133.0	3.8	3.20	
	5	2	0.02	0.02	3	4	1.5	0.3	0.32	
11	27	1988.9	0.86	0.17	21	52	141	2.40	1.40	
	2	0.6	0.06	0.10	10	10	10	0.24	0.14	

Table 1. (Contd.)

System (HD, IDS) / Level of hierarchy	P, yr / σ_P	T_0, yr / σ_{T_0}	e / σ_e	a, arcsec / σ_a	Ω, deg / σ_Ω	ω, deg / σ_ω	i, deg / σ_i	M_1, $M_\odot$ / σ_{M_1}	M_2, $M_\odot$ / σ_{M_2}	References
40887										
05566−3103										[24]
1	391	1716	0.27	3.95	143	245	110	1.28	0.69	[32]
	40	40	0.1	0.40	10	10	10	0.14	0.10	
11	68	1998.0	0.45	0.90	125	279	103	0.69	0.59	[27]
	4	0.4	0.05	0.04	5	5	5	0.10	0.10	
56986										
07142+2210										[24]
1	1200	1440	0.11	6.98	18	57	63	1.55	0.73	[33]
	120	120	0.10	0.70	10	10	10	0.80	0.10	
11	6.1	1901.2	0.35	0.00143	70	215	92	0.95	0.6	[34]
	0.6	0.6	0.10	0.00010	10	10	10	0.60	0.5	
98230/1										
11128+3205										[24, 31]
1	59.84	1995.0	0.412	2.533	101.2	127.0	122	1.14	0.94	[35]
	0.04	0.1	0.016	0.006	0.4	0.7	7	0.14	0.10	
11	1.834	1992.290	0.61	0.054	318	324	91	1.1	0.04	
	0.001	0.007	0.08	0.003	10	10	4	0.1	0.10	
108500										
12226−6113										[25]
1	2520	1953	0.63	5.43	39	173	144	1.56	0.98	[36]
	250	252	0.10	0.50	10	10	10	0.14	0.10	
11	27.1	1988.4	0.17	0.29	164	57	139	0.78	0.78	[37]
	2.7	2.7	0.10	0.03	10	10	10	0.10	0.10	
136176										
15140+2712										[24]
1	200	1941.4	0.65	1.22	62	52	58	1.8	1.1	[27]
	14	0.2	0.03	0.12	5	3	5	0.2	0.1	
11	50	1895	0.7	0.06	135	244	90	1.10	0.70	[38]
	5	5	0.1	0.01	10	10	10	0.11	0.10	
150680										
16375+3147										[39]
1	34.5	1967.8	0.46	1.36	49	111	133	1.24	0.73	
	3.5	3.5	0.1	0.1	10	10	10	0.15	0.10	
11	10.5	1953.5	0.07	0.08	23	0	90	1.05	0.19	
	1.0	1.0	0.10	0.01	10	10	10	0.11	0.10	
ADS 14296										
20435+3607										[24]
1	391	1795	0.45	0.78	139	298	134	12.8	5.12	[40]
	39	39	0.1	0.08	10	10	10	1.0	0.51	
11	11.63	1982.2	0.52	0.048	150	272	135	6.40	6.40	[41]
	1.2	1.2	0.10	0.005	10	10	10	0.64	0.64	

Table 1. (Contd.)

System (HD, IDS) Level of hierarchy	P, yr σ_P	T_0, yr σ_{T_0}	e σ_e	a, arcsec σ_a	Ω, deg σ_Ω	ω, deg σ_ω	i, deg σ_i	M_1, $M_\odot$ σ_{M_1}	M_2, $M_\odot$ σ_{M_2}	References
209790										
22009+6408										[25]
1	3800	1750	0.24	11.5	85	114	109	4.08	1.21	[42]
	380	380	0.10	1.2	10	10	10	0.29	0.12	
11	2.241	1970.992	0.50	0.072	85	273.0	68.0	2.54	1.54	[43]
	0.003	0.009	0.02	0.017	2	1.1	1.4	0.25	0.15	
209790										
22009+6408										[43]
1	3800	1750	0.24	11.5	85	114	109	1.36	0.40	[42]
	380	380	0.10	1.2	10	10	10	0.10	0.15	
11	2.241	1970.992	0.50	0.072	85	273.0	68.0	1.000	0.36	
	0.003	0.009	0.02	0.017	2	1.1	1.4	0.051	0.13	
213051/2										
22237−0032										[24]
1	760	1968	0.50	4.51	305	63	136	1.90	1.46	[44]
	76	76	0.10	0.45	10	10	10	0.25	0.15	
11	25.7	1981.2	0.59	0.076	203	23	34	1.5	0.40	
	2.6	2.6	0.10	0.008	10	10	10	0.2	0.20	
217675/6										[24]
22573+4147										[45]
1	68.6	1949.5	0.48	0.28	191	46.1	103.6	8.9	6.60	
	1.7	1.3	0.03	0.12	1	5.3	1.5	0.8	0.66	
11	8.9	1976.4	0.13	0.196	15	107	17	5.85	3.01	
	0.9	0.9	0.10	0.020	10	10	10	0.59	0.30	
218658										
23047+7451										
1	160	1934.0	0.58	0.84	64	115	28.4	6.9	1.93	[27]
	8	0.1	0.03	0.03	17	17	1.6	0.8	0.23	[46]
11	1.52	1964.37	0.3	0.0010	108	8	99.0	3.63	3.27	[47]
	0.15	0.01	0.1	0.0005	4	10	2.5	0.53	0.48	
222326										
23344+4510										[48]
1	151	1870	0.58	0.22	128	96	130	4.46	2.76	
	15	15	0.10	0.02	10	10	10	0.34	0.28	
11	15.0	1995.8	0.60	0.049	130	273	127	2.76	1.70	
	1.5	1.5	0.10	0.005	10	10	10	0.28	0.17	

4. FORMATION OF THE SAMPLE AND ITS SUBGROUPS

We selected 22 systems with $N_c \geq 3$ and known orbital parameters for the outer and inner binaries and known component masses. We excluded six of these systems, described below, from further analysis.

Table 1 gives the orbital parameters, masses, and their errors for the remaining 16 systems together with references to the original papers. The main sources of our initial data were the *Multiple Star Catalog* of Tokovinin [24] and its updated version [25].

For systems with several orbit determinations with very discrepant orbital parameters published within a short time interval, we analyzed every orbit. Likewise, when several independent estimations have yielded very different masses, we carried out our analysis using all available mass estimates.

Table 1 presents the data for all the combinations of parameters considered and the errors in the quantities determined. When no errors were reported in the original papers, we estimated them as follows.

(a) If two orbits were published within a relatively short time, with the difference between the orbital elements being comparable to the typical errors in the elements of binary orbits, we set the errors equal to the absolute values of the differences between the corresponding elements.

(b) Otherwise, we set the errors equal to 10% of the periods, semimajor axes, and masses of the stars. We also set the error of the inferred zero epoch equal to the error in the period, the error in the eccentricity to 0.1, and the errors in the angular elements to 10°.

If a component mass was less than $1M_\odot$ and no error was reported in the original paper, we set the error in this mass equal to $0.1M_\odot$, which corresponds to the typical accuracy of astrophysical data for low-mass stars.

In weakly hierarchical systems, the component motions deviate significantly from Keplerian motions, resulting in even higher errors in the inferred instantaneous values of the orbital parameters. However, our numerical simulations showed that these variations remain within the adopted errors for the sample systems and, to first approximation, are negligible for the orbital arcs described by the components during the time they have been observed.

Let us discuss the system HD 29316 in more detail. We have two independent and highly discrepant mass estimates for this multiple star, published by Heintz [31] and Tokovinin [24]. The component masses suggested by Heintz [31] are inconsistent with the observed spectral types, A8V+F9V (SIMBAD database [24]), and the combination of component masses presented by Tokovinin [24] is more plausible. Table 1 lists both versions, but we performed our subsequent computations for the second version only, and do not consider the mass estimates of Heintz [31] further.

Our sample consists of four groups.

(1) All systems with $N_c = 3$ for which both orbits have been determined. We applied all the above stability criteria to these systems. If the margin of stability is sufficiently high ($\delta_i \geq 1$ for all criteria), the system is likely to be stable. Otherwise, we analyzed the dynamical evolution of the system.

(2) All systems with $N_c > 3$ for which the orbital elements of all the subsystems have been determined. We analyzed these systems using the stability criteria for triple systems when the closest pairs are strongly isolated from other components of the system, and each can be regarded as a single body with a mass equal to the total mass of the components of the pair. If the margin of stability is low ($\delta_i \leq 1$), we analyzed the dynamic evolution of the system, as in the previous case. This approximation is not appropriate if the close pairs are not sufficiently isolated from the other stars of the system, and, in this case, the dynamical evolution of the system with $N_c > 3$ bodies must be analyzed. We plan to do this in a separate study.

(3) All systems with $N_c > 3$ for which orbital elements have been determined only for two adjacent hierarchy levels. We subdivide these systems into two subgroups:

(a) Systems for which the components external to the subsystem considered affect the dynamics only slightly, and the inner close binaries can be represented by point masses. We analyzed these systems as triple stars.

(b) Systems that maintain weak hierarchy over several sublevels; so far, we can give no definitive conclusions about their dynamics, since the analysis of the dynamics for systems of this subgroup requires additional observational data.

(4) Systems with close binaries with periods ($P_{in} \leq 10^{\mathrm{d}}$) whose evolution is strongly affected by the tidal interaction between the components (this especially applies to systems with late-type components). Such systems must be analyzed using special algorithms to simulate their evolution taking into account the tidal interaction and, in a number of cases, mass transfer, between the components. However, for none of the selected multiple stars with $P_{in} \leq 10^{\mathrm{d}}$ is the set of orbital parameters for the inner binaries complete, hindering a full analysis of their dynamics. Moreover, the sizes of the inner subsystems are usually much smaller than the pericenter distances of the outer subsystems, and such systems should have high margins of stability. Some exceptions (such as the λ Tau and CH Cyg systems) require

special studies. Eggleton and Kiseleva [49] have achieved some progress in analyzing the dynamics of such subsystems, taking into account astrophysical effects. In our analysis, we treat the inner subsystems as point masses; this approach is justified by the high ratios of the sizes of the outer and inner systems ($\sim 10^2$ or more for all objects of this group).

Table 2 lists the objects of groups 1, 3, and 4. We discuss both systems of group 2 (HD 68255/6/7 and HD 76644) below.

Let us now discuss the systems excluded from further analysis and thereby from Table 1.

(1) IDS 02208+6657 = HD 15089 = ADS 1860 = HIP 11569 = ι Cas.

This is a visual triple system whose primary has been resolved using speckle interferometry [50] and found to be a binary with period ≈50 yr and semimajor axis ≈0.1″ [31]; i.e., the system consists of four components. The angular separations AB and AC differ by less than a factor of three, and are equal to 2.9″ and 6.7″, respectively. An orbital solution has been obtained for the AB pair [31], but the orbit AB–C remains undetermined, making it impossible to analyze the dynamics of this system at the current time.

(2) IDS 08415+0647 = ADS 6993 = ϵ Hya.

This system consists of five components with angular separations of 0.0025″ (SB1 subsystem Cc), 0.25″ (AB), 4.66″ (AB–C), and 19″ (ABC–D). The periods of the innermost SB1 subsystem and of the outermost system are $P_{in} = 10^{\rm d}$ and $P_{out} = 8300$ yr. Not all orbital parameters have been determined for the system [24, 25, 31]. The AB–C subsystem has a period of 990 yr and is weakly hierarchical with respect to the ABC–D subsystem, with an angular-separation ratio of ∼4.5. In this case, the dynamics of the inner subsystem must be modeled including the perturbations due to component D, for which not all orbital elements have been determined; so far, only the period has been estimated.

(3) IDS 14516–2058 = GJ 570.

This system has four components with angular separations of 0.143″, 32.3″, and 258″ and periods of 0.84, 2130, and 45400 yr, respectively [25]. The orbit of the outer subsystem has not been determined, making it impossible to correctly model the dynamics of the inner subsystem without including the perturbations due to the distant component, given the period ratio of ∼20.

(4) IDS 15596–1932 = β Sco.

The system consists of five components, with the most distant having an angular separation of 13.6″ from the primary. The orbits of the subsystems have semimajor axes of 0.0014″, 0.14″, and 3.9″. The ratio

Table 2. Division of the objects into groups

System (HD, IDS)	Multiplicity[7] Subgroup
5408[1]	4
00508+5949	4
9770[2]	4
01304–3026	4
12376[3]	4
01562+3614	4
29316[4]	4:
04320+5316	3
40887	3
05566–3103	1
56986	3
07142+2210	1
98230/1[5]	4:
11128+3205	4
108500	3
12226–6113	1
136176	3
15140+2712	1
150680	3
16375+3147	1
ADS 14296	3
20435+3607	1
209790	3
22009+6408	1
213051/2	3
22237–0032	1
217675/6[6]	4
22573+4147	3
218658	3
23047+7451	1
222326	3
23344+4510	1

[1] Primary in the inner subsystem is a spectroscopic binary (SB2) with a period of $P = 4.24^{\rm d}$.
[2] Primary in the inner subsystem is an eclipsing spectroscopic binary with a period of $P = 0.47^{\rm d}$.
[3] Primary in the inner subsystem is a spectroscopic binary with a period of $P = 3.1^{\rm d}$.
[4] There is an $m_v = 13^m$ companion at an angular separation of ≈23″ from the triple star.
[5] Inner subsystem is made up of a pair with $P = 1.8$ yr and an SB1 spectroscopic binary with a period of $P = 3.98^{\rm d}$. There is a $m_v = 15^m$ likely physical companion at a separation of $\rho \approx 54''$. The system may contain another close companion.
[6] Outer subsystem is made up of a pair with a period of $P = 8.9$ yr and a spectroscopic binary with a period of $P = 3^{\rm d}$.
[7] Uncertainty in the multiplicity is indicated by a colon after the indicated number of components in the system.

Table 3. Stability parameters of the systems. The values of the corresponding parameters, critical values, and margins of stability δ are given for each criterion. The presented parameters are s, s_c, δ_s (Golubev criterion); F, F_c, δ_F (Harrington criterion); X, X_c, δ_X (Eggleton–Kiseleva criterion); Z, Z_c, δ_Z (Mardling–Aarseth criterion); Q, Q_c, δ_Q (Valtonen–Karttunen criterion); T, T_c, δ_T (Tokovinin criterion)

System	s	F	X	Z	Q	T
	s_c	F_c	X_c	Z_c	Q_c	T_c
	δ_s	δ_F	δ_X	δ_Z	δ_Q	δ_T
HD 5408	7.61	5.91	17.16	4.80	5.91	7.50
ADS 784	5.56	5.57	9.21	2.69	4.52	5.00
	0.37	0.06	0.86	0.79	0.31	0.50
HD 9770	6.09	7.02	24.50	5.27	7.02	12.08
GJ 60	3.86	5.23	7.88	2.12	4.50	5.00
(version 1)	0.58	0.34	2.11	1.49	0.56	1.42
HD 9770	5.70	7.02	24.50	5.40	7.02	12.08
GJ 60	3.86	5.23	7.61	2.09	4.39	5.00
(version 2)	0.48	0.34	2.22	1.58	0.60	1.42
HD 12376	5.10	6.23	25.51	4.43	6.23	7.67
ADS 1613	4.73	5.29	11.69	1.89	4.30	5.00
	0.08	0.18	1.18	1.35	0.45	0.53
HD 29316*	5.69	5.32	16.14	2.86	5.32	5.08
ADS 3358	5.42	5.72	21.35	1.63	5.86	5.00
	0.05	−0.07	−0.24	0.75	−0.09	0.02
HD 40887*	5.75	2.71	5.76	1.87	2.71	2.24
GJ 225.2	6.26	5.53	12.60	2.16	4.83	5.00
	−0.08	−0.51	−0.54	−0.13	−0.44	−0.55
HD 56986	27.85	34.12	195.68	25.27	34.12	137.95
ADS 5983	5.99	5.48	8.11	2.01	4.36	5.00
	3.65	5.23	23.13	11.57	6.83	26.59
HD 98230/1	2.28	7.34	32.63	4.56	7.34	6.63
ADS 8119	2.27	4.90	21.09	1.74	3.95	5.00
	0.00	0.50	0.55	1.62	0.86	0.33
HD 108500*	11.52	8.88	92.14	7.59	8.88	4.67
	6.16	5.59	25.96	3.04	4.47	5.00
	0.87	0.59	2.55	1.50	0.99	−0.07
HD 136176*	2.37	1.03	3.99	0.61	1.03	0.17
ADS 9578	6.00	5.58	48.34	1.92	5.40	5.00
	−0.60	−0.81	−0.92	−0.68	−0.81	−0.97
HD 150680*	2.46	1.39	3.28	1.30	1.39	0.52
ADS 10157	3.67	5.56	12.20	3.22	4.40	5.00
	−0.33	−0.75	−0.73	−0.60	−0.68	−0.90

Table 3. (Contd.)

System	s	F	X	Z	Q	T
	s_c	F_c	X_c	Z_c	Q_c	T_c
	δ_s	δ_F	δ_X	δ_Z	δ_Q	δ_T
HD 198183	9.91	6.41	33.61	4.22	6.41	5.59
ADS 14296	6.09	5.43	20.23	2.15	5.09	5.00
	0.63	0.18	0.66	0.96	0.26	0.11
HD 209790	85.79	117.85	1695.85	78.57	117.85	744.44
ADS 15600	5.27	5.34	11.15	1.84	4.75	5.00
(version 1)	15.27	21.05	151.14	41.77	23.78	147.89
HD 209790	69.64	117.79	1695.85	78.52	117.78	744.44
ADS 15600	4.15	5.34	10.71	1.84	4.75	5.00
(version 2)	15.79	21.04	157.29	41.78	23.78	147.89
HD 213051/2*	4.26	5.78	29.56	3.64	5.78	3.70
ADS 15971	4.36	4.88	26.19	1.80	3.95	5.00
	−0.02	0.19	0.13	1.02	0.46	−0.26
HD 217675/6*	2.75	2.44	7.69	2.16	2.44	1.08
o And	5.50	4.87	14.82	2.75	3.61	5.00
	−0.50	−0.50	−0.48	−0.22	−0.32	−0.78
HD 218658	10.44	10.14	104.93	7.80	10.14	7.77
ADS 16538	5.52	5.33	22.72	2.33	4.34	5.00
	0.89	0.90	3.62	2.35	1.34	0.55
HD 222326*	4.74	2.30	10.05	1.44	2.30	0.74
ADS 16904	5.95	5.58	33.60	2.28	5.49	5.00
	−0.20	−0.59	−0.70	−0.37	−0.58	−0.85

Note: Asterisks indicate systems we found to be unstable according to some (or all) of the criteria employed (see text).

of the apparent sizes of the outer orbit and the orbit of the subsystem of the next hierarchy level is ∼3.5. The binary at the next hierarchy level has an orbital semimajor axis of 3.9″, period of 610 yr, and eccentricity of 0.91. Thus, the orbits of the two outer components may have comparable semimajor axes and periods, making a dynamical analysis of this system of interest. However, such an analysis is currently impossible because the orbital elements for the outer body are not known [25].

(5) IDS 08065+1757 = HD 68255/6/7 = ADS 6650 = HIP 40167.

This is a quadruple system whose two inner orbits and outer orbit are all known. It consists of two relatively close systems with periods of 59.6 yr and 17.3 yr (with orbital semimajor axes 0.862″ and 0.182″, respectively). The period of rotation of the pairs about their common center of mass is 1120 yr, and the semimajor axis of the relative orbit is 7.7″ [25, 31]. The ratios of the outer and inner periods are thus equal to 19 and 64, implying that the dynamics of the system should be modeled taking into account the interactions of all four components, as we plan to do in the future.

(6) IDS 08524+4826 = HD 76644 = ADS 7114 = HIP 44127= ι UMa.

This is also a quadruple system for which the two inner orbits and the outer orbit are all known, and which consists of two close subsystems that rotate with a period of 818 yr ($a = 9.092''$) about their common center of mass. The periods of the inner subsystems are 39.7 and 11.0 yr (the corresponding

Table 4. Stability parameters of the systems (same as Table 3 but with the longitude of the ascending node changed by 180° for one of the subsystems)

System	s	F	X	Z	Q	T
	s_c	F_c	X_c	Z_c	Q_c	T_c
	δ_s	δ_F	δ_X	δ_Z	δ_Q	δ_T
HD 5408*	5.17	5.91	17.16	4.80	5.91	7.50
ADS 784	5.56	4.80	9.21	2.23	3.71	5.00
	−0.07	0.23	0.86	1.16	0.59	0.50
HD 9770	5.15	7.02	24.50	5.27	7.02	12.08
GJ 60	3.86	5.23	7.88	1.97	4.35	5.00
(version 1)	0.34	0.34	2.11	1.67	0.61	1.42
HD 9770	5.61	7.02	24.50	5.40	7.02	12.08
GJ 60	3.86	5.23	7.61	2.08	4.38	5.00
(version 2)	0.46	0.34	2.22	1.60	0.60	1.42
HD 12376*	2.26	6.23	25.51	4.43	6.23	7.67
ADS 1613	4.73	4.60	11.69	1.65	3.21	5.00
	−0.52	0.35	1.18	1.68	0.94	0.53
HD 29316*	5.71	5.32	16.14	2.86	5.32	5.08
ADS 3358	5.42	5.72	21.35	1.64	5.88	5.00
	0.05	−0.07	−0.24	0.75	−0.09	0.02
HD 40887*	2.30	2.71	5.76	1.87	2.71	2.24
GJ 225.2	6.26	4.77	12.60	1.70	3.32	5.00
	−0.63	−0.43	−0.54	0.10	−0.18	−0.55
HD 56986	22.72	34.12	195.68	25.27	34.12	137.95
ADS 5983	5.99	4.74	8.11	1.76	3.50	5.00
	2.79	6.21	23.13	13.32	8.76	26.59
HD 98230/1	2.36	7.34	32.63	4.56	7.34	6.63
ADS 8119	2.27	5.71	21.09	2.06	5.24	5.00
	0.04	0.29	0.55	1.27	0.40	0.33
HD 108500*	12.72	8.88	92.14	7.59	8.88	4.67
	6.16	5.59	25.96	3.23	4.70	5.00
	1.06	0.59	2.55	1.35	0.89	−0.07
HD 136176*	1.85	1.03	3.99	0.61	1.03	0.17
ADS 9578	6.00	4.80	48.34	1.81	4.93	5.00
	−0.69	−0.79	−0.92	−0.67	−0.79	−0.97
HD 150680*	1.49	1.39	3.28	1.30	1.39	0.52
ADS 10157	3.67	4.79	12.20	2.74	3.35	5.00
	−0.59	−0.71	−0.73	−0.53	−0.58	−0.90

Table 4. (Contd.)

System	s	F	X	Z	Q	T
	s_c	F_c	X_c	Z_c	Q_c	T_c
	δ_s	δ_F	δ_X	δ_Z	δ_Q	δ_T
HD 198183	7.09	6.41	33.61	4.22	6.41	5.59
ADS 14296	6.09	4.70	20.23	1.85	4.48	5.00
	0.16	0.36	0.66	1.28	0.43	0.12
HD 209790	68.14	117.85	1695.85	78.57	117.85	744.44
ADS 15600	5.27	4.64	11.15	1.39	2.73	5.00
(version 1)	11.92	24.41	151.14	55.52	42.21	147.89
HD 209790	57.49	117.78	1695.85	78.52	117.78	744.44
ADS 15600	4.15	4.64	10.71	1.39	2.73	5.00
(version 2)	12.86	24.40	157.29	55.53	42.19	147.89
HD 213051/2*	4.38	5.78	29.56	3.64	5.78	3.70
ADS 15971	4.36	4.88	26.19	1.85	4.21	5.00
	0.00	0.19	0.13	0.97	0.37	−0.26
HD 217675/6*	3.53	2.44	7.69	2.16	2.44	1.08
o And	5.50	5.66	14.83	2.94	4.12	5.00
	−0.36	−0.57	−0.48	−0.27	−0.41	−0.78
HD 218658	7.50	10.14	104.93	7.80	10.14	7.77
ADS 16538	5.52	4.63	22.72	2.15	3.76	5.00
	0.36	1.19	3.62	2.63	1.70	0.55
HD 222326*	3.11	2.30	10.05	1.44	2.30	0.74
ADS 16904	5.95	4.81	33.60	1.90	4.63	5.00
	−0.48	−0.52	−0.70	−0.24	−0.50	−0.85

Note: Asterisks indicate systems we found to be unstable according to some (or all) of the criteria employed (see text).

orbital semimajor axes are 0.680″ and 0.474″, respectively) [25]. As in the previous case, we plan to analyze the dynamics of this system in the framework of the four-body problem in the future.

5. ANALYSIS OF THE STABILITY OF MULTIPLE SYSTEMS BASED ON THE STABILITY CRITERIA AND DYNAMICAL-EVOLUTION COMPUTATIONS

We used the listed stability criteria to analyze the stability of each of the 16 systems and estimated the margin of stability δ_i for each of the six criteria. The results are presented in Table 3.

The longitude of the ascending node is the parameter that is most problematic to determine. Therefore, although this parameter has, in principle, been determined unambiguously in the original papers, we also present here the results of our empirical computations for $\Omega + 180°$ (Table 4). As is evident from a comparison of the data in Tables 3 and 4, changing Ω does not appreciably affect the inferred stability. We also computed the empirical stability for the Ω_{in} and Ω_{out} values yielding the most stable configurations. Even in this case, the stability parameters of the systems did not change qualitatively. Thus, a 180° ambiguity in Ω, and even significant deviations from the published values, have no qualitative effect on the stability of these systems.

We have several systems with unstable motions according to some (and, in some cases, all) of the criteria employed, marked by asterisks in Tables 3 and 4.

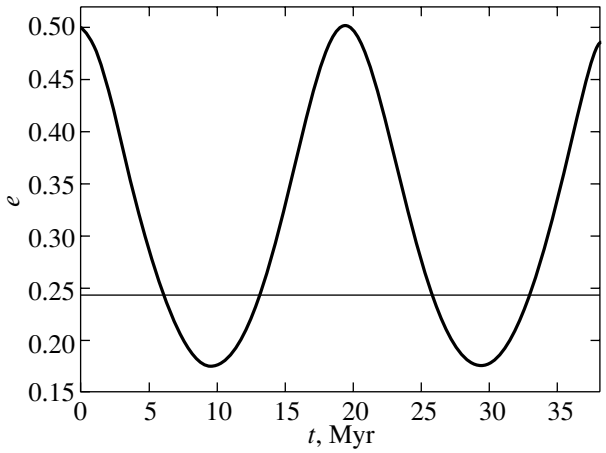

Fig. 1. Time variations of orbital eccentricities in the hierarchical system HD 209790 ($P_{out} = 3800$ yr and $P_{in} = 2.24$ yr). The thin and bold curves correspond to the outer and inner orbits, respectively.

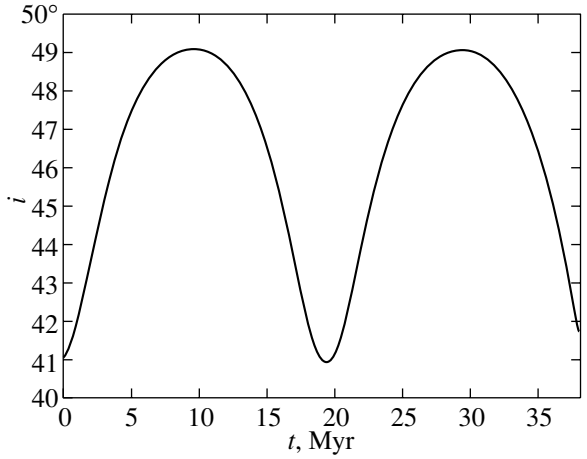

Fig. 2. Time variations of the mutual orbital inclination in the hierarchical system HD 209790.

For these systems, and also for the systems with a minimum margin of stability $\delta_i \leq 1$, we performed further analyses of their stability by numerically simulating their dynamical evolution. For comparison purposes, we performed similar computations for the system HD 209790, which has a substantial margin of stability ($\delta_i > 10$).

The TRIPLE code that we used enables integration of the equations of motion with a fractional error in the total energy of no more than 10^{-10} over $\sim 10^6$ yr of the system's evolution. We also monitored the integration errors by computing the evolution forward and back to return to the initial time and comparing the resulting coordinates and velocities with their initial values. The fractional deviations of the coordinates and velocities from their initial values did not exceed 5% over 2×10^6 yr of evolution, demonstrating that the integration errors were small.

We chose the total integration time based on the following considerations. Systems that are unstable according to the results of Anosova and Orlov [6], Hut [51], Eggleton and Kiseleva [17], and Rubinov *et al.* [7] will be disrupted on time scales of $\sim 10^2 - 10^3$ rotations of the outer binary. The evolution time scale is $\sim 10^6$ yr for all the sample systems except HD 108500 and the comparison system HD 209790, for which it exceeds $1000 P_{out}$. Our computations for HD 108500 covered 2.5×10^6 yr, which is $\approx 10^3 P_{out}$.

We followed the evolution of HD 209790 for $1000 P_{out}$. Note that, as is evident from Figs. 1 and 2, the orbital elements of this system are either constant (semimajor axis and eccentricity of outer binary), or undergo Kozai oscillations (mutual inclination i and eccentricity of the inner orbit), so that $\sqrt{1 - e_{in}^2} \cos i = \text{const}$ [52]. It follows that this system does not show a tendency to disrupt over long time scales—a result that is natural for a system with considerable hierarchy. The simulations of the dynamics of all the systems with considerable margins of stability yield similar results.

The variations of the orbital parameters of unstable systems are not periodic (as is clear from the example of HD 136176; see Figs. 3–5). Table 5 lists the disruption times for five systems that are unstable according to all six criteria employed. We determined the disruption times for these systems by numerically computing their evolution. We also computed the evolution from the present time to 10^6 yr in the past for the systems shown to be unstable by our simulations. All these systems were unstable in the case of this reverse evolution as well. The disruption times, velocities of ejected bodies, total system lifetimes, and the periods of the initial binaries (prior to capture) are also listed in Table 5.

These data lead us to conclude that unstable systems are likely to be dynamically young objects. They could have formed during encounters between single stars and multiple systems with small relative velocities ($\sim$1–10 km/s). We found the highest ejection velocity to be that for HD 217675/6, which is closer than the other unstable systems listed in Table 5.

6. DISCUSSION OF RESULTS

We have analyzed the dynamical evolution of 16 multiple systems using various stability criteria and numerical simulations of the component motions.

The results lead to the following conclusions.

(1) The stability criteria agree with the results of the numerical simulations. The criterion proposed by Mardling and Aarseth [18] was the most accurate: it

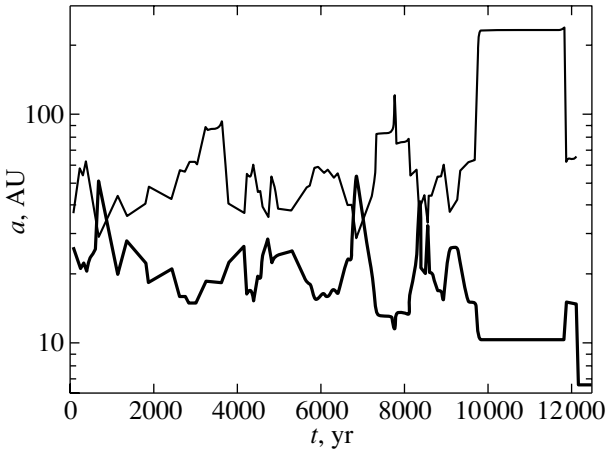

Fig. 3. Time variations of the instantaneous semimajor orbital axes in the unstable system HD 136176 ($P_{out} =$ 200 yr and $P_{in} = 50$ yr). The thin and bold lines correspond to the outer and inner orbit, respectively.

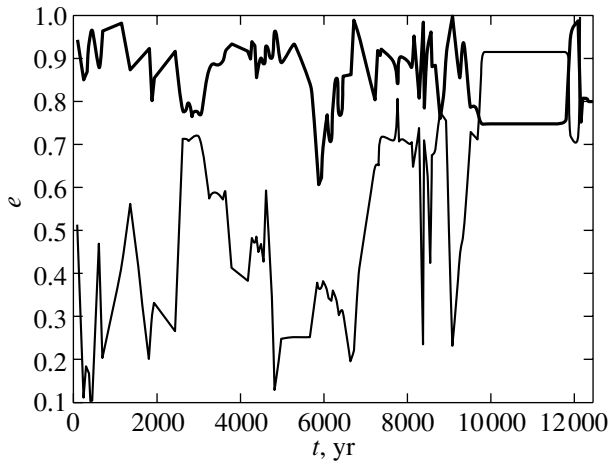

Fig. 4. Time variations of the orbital eccentricities in the unstable system HD 136176. The thin and bold lines correspond to the outer and inner orbit, respectively.

indicated instability for all the unstable systems and "failed" for none of the stable systems. Although the other criteria overall agreed with the results of the numerical simulations, they yielded discrepant conclusions about the stability of some systems. However, firmer conclusions about which of the stability criteria are most adequate is not possible without including the effect of the errors in the initial parameters.

(2) 11 systems (HD 5408, HD 9770, HD 12376, HD 29316, HD 56986, HD 98230, HD 108500, HD 198183, HD 209790, HD 213051/2, HD 218658) appear to be stable. Five systems (HD 40887, HD 136176, HD 150680, HD 217675, HD 222326) appear to be unstable.

Thus, most of the sample systems were identified as being stable, but a few may be unstable.

6.1. Reliability of the Orbital Parameters

It is important to have reliable data in order to obtain trustworthy results.

Of course, the stability of the observed multiple systems is a classical and expected result, in contrast to the conclusion that some of them are unstable. Therefore firmer conclusions can be drawn only after an analysis that takes into account the errors in the observational data. However, we wish to discuss in more detail the reliability of the orbital parameters for the systems that were identified as potentially being unstable. In particular, we wish to determine whether this result could be due to errors in the parameters of these systems. To address this question, we briefly describe each of the five potentially unstable systems.

HD 40887. This is a triple system for which Baize [32] published a solution for the outer orbit with a period and semimajor axis of 390 yr

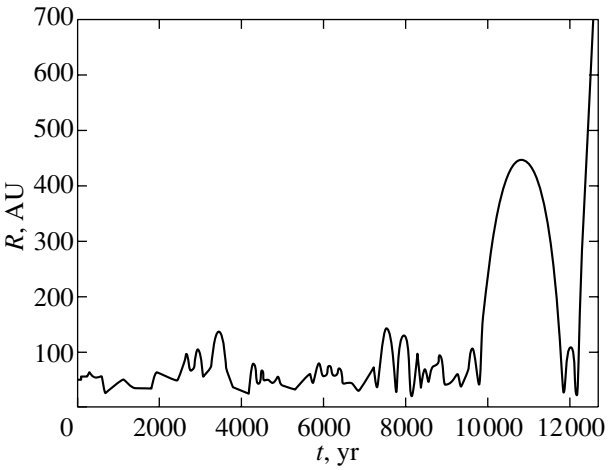

Fig. 5. Time variations of the distance between the center of mass of the inner binary and outer body, and the disruption of the unstable system HD 136176.

and 3.95″, respectively, in 1980. The arc described by the system covers 123°, and the orbit is based on 66 data points spanning the interval from 1835 through 1977. The number of points and the length of the observed arc rule out the possibility that the orbit could be completely wrong. The inner orbit of this system is based on 50 points spanning the interval from 1911 through 1996 and covering the entire period of the close pair. In his *Multiple Star Catalog*, Tokovinin [24] gives a period of 72 yr and a semimajor axis of 0.940″ for this star. Soderhjelm [27] published a refined orbit for this subsystem with similar parameters: $P = 68$ yr, $a = 0.900''$. The components have spectral types K(3–5)V. We adopted the component masses from [24] ($0.69M_\odot$, $0.69M_\odot$, and $0.59M_\odot$). The original papers do not present the

Table 5. Parameters of the dynamical evolution of unstable systems: the time before disruption for forward evolution t^+_{dis}, time before disruption for reverse evolution t^-_{dis}, total lifetime of the system t_{life} ($= t^+_{dis} + t^-_{dis}$), current orbital period of the outer subsystem P_{out}, orbital period of the binary after disruption P_{bin} (for reverse evolution), velocity of the ejected body V_{esc} (for reverse evolution) in the reference frame of the remaining binary

	HD 40887	HD 150680	HD 136176	HD 217675/6	HD 222326
t^+_{dis}, yr	378970	2750	17060	11130	5980
t^-_{dis}, yr	153830	2920	31960	7130	6780
t_{life}, yr	532980	5680	49020	18260	12760
t_{life}/P_{out}	1360	165	245	266	84
t_{life}/P_{bin}	18100	433	1420	2010	856
P_{bin}, yr	29.4	13.1	34.6	9.1	14.9
V_{esc}, km/s	2.3	7.8	2.8	12.5	3.8

errors in the orbital parameters, but the agreement between the orbits published by the different authors argues that these parameters have been determined correctly.

HD 136176. This is a triple system with a wide pair that has been observed since 1830. Heintz [53] derived the first orbit for this system in 1965 ($P =$ 203 yr, $a = 1.216''$), which was subsequently (in 1983) refined by Walbaum and Duvent [54] ($P =$ 186 yr, $a = 1.095''$). Soderhjelm [27] published the most recent version of the orbit for this subsystem ($P = 200$ yr, $a = 1.22''$). All three orbits have very similar parameters. The orbital arc observed by 1999 covers nearly the entire period, so that the derived orbital parameters should be quite reliable. Heintz [53] was the only author to report errors for the orbital parameters, and these errors indicate that the observations are fit well by the orbit (the reported errors in the period, semimajor axis, and eccentricity were ± 9 yr, $\pm 0.12''$, and ± 0.03, respectively).

Muller [38] published a solution for the inner orbit ($P = 50$ yr, $a = 0.055''$), which, despite the rather short period, may have considerable errors, since it is perpendicular to the plane of the sky. At the same time, the ratio $P_{out}/P_{in} = 4$ is very small, suggesting that the inner orbit will be unstable for a wide range of parameters, even if they have large errors.

The component masses listed in [24] and [55] are mutually consistent. All the components of the system have comparable masses and spectral types close to G0V.

HD 150680. This is a triple system consisting of a wide pair (G0IV+G7V) with a period of 34.5 yr and a semimajor axis of $1.355''$. Baize [39] published both orbits but does not report the corresponding errors.

Some researchers doubt the existence of the third component, since all the elements of the inner orbit were determined by analyzing perturbations of the outer subsystem and the third component has been observed visually only once in the infrared [56]. The third component must have a mass of no more than $0.19 M_\odot$.

It is not unlikely that the solution is erroneous: given the parameters of the outer orbit, the period and semimajor axis of the inner subsystem cannot be simultaneously equal to 10.5 yr and $0.08''$, whatever the component masses, provided that the motion is Keplerian. However, this latter assumption may be incorrect in the case of weak hierarchy, and the instantaneous parameter values (based on 71 observations spanning the period from 1935 through 1969) may be close to those determined by Baize [39]. It is also possible that there is a typographical error in Baize's paper [39].

HD 217675/6. This system has four components. The outer pair has a period and semimajor axis of 68.6 yr and $0.277''$ (according to the orbit published by Hartkopf [45], which is based on more than 60 positions obtained since 1949), while the closer subsystem has a period of 8.933 yr and is a spectroscopic and speckle-interferometric binary. The secondary, in turn, is a β Lyr eclipsing spectroscopic binary with a period of 33 days [24]. Although the astrometric orbit with a period of 8.9 yr is based on only six points, we consider its parameters to be fairly reliable, since some of them were determined independently from spectroscopic observations.

The period of the closest subsystem is two orders of magnitude shorter than the period of the subsystem with the next hierarchy level. Therefore, the binary nature of the primary does not affect the dynamics of the system to first approximation. Hartkopf [45] reports small errors for the parameters of the outer pair, which indicate a good agreement between the

reconstructed orbit and the observations, but gives no errors for the inner subsystem.

HD 222326. This is a triple system. Heintz [57] was the first to derive the orbit of the outer pair (which was found to be a binary in 1903) and determine its period, 292 yr. Zulevic [58] refined the orbit and found the period to be 238 yr. Balega *et al.* [48] derived a more accurate orbit using speckle-interferometric data obtained with the 6-meter telescope of the Special Astrophysical Observatory of the Russian Academy of Sciences. They published the first orbit for the inner subsystem (CHARA 149), whose binarity had been established in 1986. According to their results [48], the parameters of the outer and inner subsystems are $P_{out} = 151.4$ yr, $a_{out} = 0.221''$ and $P_{in} = 15.03$ yr, $a_{in} = 0.049''$. The outer orbit was reconstructed from a 110° arc that does not include the epoch of periastron, and which Balega *et al.* [48] consider to be a preliminary solution. However, the arc spanned is sufficiently long for the orbital parameters to be determined without gross errors. The inner orbit, which is based only on five speckle-interferometric observations, is less reliable in this sense. Balega *et al.* [48] estimate the spectral types of the components to be A2V+A2V+F0 and give no errors for the orbital parameters.

Thus, out of the five systems found to be unstable by our preliminary analysis, two have reliably-determined orbits with errors that are too small to be responsible for their inferred instability. The orbital solutions for three systems (HD 136176, HD 150680, and HD 222326) require refinement, but even with substantial changes in their parameters, these systems would be near the edge of the domain of stability.

We conclude that the results obtained for these five systems can hardly be due to inaccuracy in their orbital parameters. On the other hand, in order for the analysis of the stability of these systems to yield more conclusive results, this analysis must incorporate the observational errors. We plan to perform such an analysis in the future.

6.2. Interpretation of Results

We have carried out numerical simulations of multiple systems over time intervals that are several orders of magnitude shorter than the assumed component ages. Therefore, the likely dynamical instability and small dynamical ages implied by these simulations cannot be a consequence of physically small ages for the stars in the systems.

The instability of these systems could have resulted from the temporary capture of a field or cluster star in an encounter with a close binary, or via encounters between two multiple systems. Computations of the probability of the formation of binary and multiple stars in the Galaxy via capture (see, e.g., [59]) usually disregard the fact that stars in binary and multiple systems outnumber single stars. On the other hand, the formation of a temporary triple system (or even a system with more components) does not require an encounter of three single stars, which is a very rare event. It is sufficient to estimate the probability of an encounter between a field star and a binary, or between two binaries, which have much higher probabilities.

According to Hut [51], the median lifetime of such systems (hierarchical resonance scattering) is $\sim 500 P_{bin}$, where P_{bin} is the period of the binary that participated in the encounter with a field star. At the same time, the distribution of disruption times is very asymmetric, and an appreciable fraction of systems will be disrupted over longer times. For example, one-third and 10% of the systems have lifetimes longer than $3000 P_{bin}$ and $12\,000 P_{bin}$, respectively.

It is clear from Table 5 that the systems considered have lifetimes of $\sim(10^2-10^4)P_{bin}$, consistent with Hut's [51] estimates, supporting the idea that some of these systems formed via capture. Our estimates of the relative approach velocities are consistent with the residual velocities of stars in moving clusters, to which some of the systems belong, and do not rule out encounters with field stars.

Instability can also be explained by a recent encounter (without capture) between a stable system and a massive object—field star, black hole, or molecular cloud—that perturbed the component motions and moved the system beyond the stability domain into the domain of unstable motion.

It is not unlikely that some of the observed unstable systems are products of disrupted stellar groups or clusters with initial populations of $\sim 10^1-10^3$ objects, which are now in their final stage of evolution. This hypothesis seems to be more plausible for massive (and, consequently, young) systems, such as HD 217675/6 (with a B2III primary) and HD 222326 (with A2V+A2V+F0 components).

The existence of unstable multiple stars could have various origins. It is possible that a choice between possible mechanisms can be made based on a detailed analysis of the physical and dynamical properties of the systems as a whole and their constituent components, and by computing the probabilities of the realization of each scenario. Firmer conclusions about the stability or instability of the systems considered will become possible after an analysis of the errors of the observational data and their effect on the results of the dynamical-evolution simulations. We plan to carry out such an analysis in the near future.

ACKNOWLEDGMENTS

V.V. Orlov acknowledges the Program for the Support of Leading Scientific Schools of Russia (grant no. NSh 1078.2003.02), the Russian Foundation for Basic Research (project no. 02-02-17516), and the program "Universities of Russia" of the Ministry of Education and Science of the Russian Federation (grant no. UR.02.01.027) for supporting this work.

REFERENCES

1. A. Duquennoy and M. Mayor, Astron. Astrophys. **248**, 485 (1991).
2. A. V. Rubinov, A. V. Petrova, and V. V. Orlov, Publ. Astron. Observ. Belgrade **75**, 17 (2003).
3. Y. Kozai, Astron. J. **67**, 591 (1962).
4. Y. Krymolowski and T. Mazeh, Mon. Not. R. Astron. Soc. **304**, 720 (1999).
5. E. B. Ford, B. Kozinsky, and F. A. Rasio, Astrophys. J. **535**, 385 (2000).
6. Zh. P. Anosova and V. V. Orlov, Trudy Astron. Obs. Lenin. Gos. Univ. **40**, 66 (1985).
7. A. V. Rubinov, A. V. Petrova, and V. V. Orlov, Astron. Zh. **79**, 1044 (2002) [Astron. Rep. **46**, 942 (2002)].
8. V. G. Szebehely and K. Zare, Astron. Astrophys. **58**, 145 (1977).
9. F. C. Fekel, Astrophys. J. **246**, 879 (1981).
10. J. R. Donnison and D. F. Mikulskis, Mon. Not. R. Astron. Soc. **272**, 1 (1995).
11. V. V. Orlov and A. V. Petrova, Pis'ma Astron. Zh. **26**, 301 (2000) [Astron. Lett. **26**, 250 (2000)].
12. L. Loinard, L. F. Rodriguez, and M. I. Rodriguez, Astrophys. J. **587**, L47 (2003).
13. V. G. Golubev, Dokl. Akad. Nauk SSSR **12**, 529 (1967) [Sov. Phys. Dokl. **12**, 420 (1967)]
14. V. G. Golubev, Dokl. Akad. Nauk SSSR **13**, 373 (1968) [Sov. Phys. Dokl. **13**, 308 (1968)].
15. R. S. Harrington, Celest. Mech. **6**, 322 (1972).
16. R. S. Harrington, Astron. J. **82**, 753 (1977).
17. P. Eggleton and L. Kiseleva, Astrophys. J. **455**, 640 (1995).
18. R.-M. Mardling and S. J. Aarseth, *The Dynamics of Small Bodies in the Solar System: A Major Key to Solar System Studies,* Ed. by B. A. Steves and A. E. Roy (Kluwer, Dordrecht, 1999), p. 385.
19. M. Valtonen and H. Karttunen, *Three-body Problem in Astrophysics* (Cambridge Univ., Cambridge, 2005) (in press).
20. A. A. Tokovinin, Rev. Mex. Astron. Astrofis. (Ser. Conf.) **21**, 7 (2004).
21. J. S. Griffith and R. D. North, Celest. Mech. **8**, 473 (1974).
22. S. J. Aarseth and K. Zare, Celest. Mech. **10**, 185 (1974).
23. W. A. Cole, F. C. Fekel, W. I. Hartkopf, H. A. McAlister, and J. Tomkin, Astron. J. **103**, 1357 (1992).
24. A. A. Tokovinin, Astron. Astrophys., Suppl. Ser. **124**, 75 (1997).
25. A. A. Tokovinin, Priv. Comm. (2003).
26. L. J. Newburg, Republic Observ. Circ. **7**, 192 (1969).
27. S. Soderhjelm, Astron. Astrophys. **341**, 121 (1999).
28. B. D. Mason and W. I. Hartkopf, Inform. Circ. **138** (1999).
29. W. D. Heintz, Publ. Astron. Soc. Pac. **85**, 408 (1973).
30. W. I. Hartkopf, Astron. J. **119**, 3084 (2000).
31. W. D. Heintz, Astron. J. **111**, 408 (1996).
32. P. Baize, Inform. Circ. **80** (1980).
33. J. Hopmann, Mitt. Sternw. Wien **10**, 155 (1960).
34. M. A. C. Perryman *et al.*, *The Hipparcos and Tycho Catalogues* (ESA Publications, Noordwijk, 1997).
35. B. D. Mason, H. A. McAlister, W. I. Hartkopf, and M. M. Shara, Astron. J. **109**, 332 (1995).
36. D. Seymour, Astron. J. **123**, 1023 (2002).
37. W. D. Heintz, Astrophys. J., Suppl. Ser. **111**, 335 (1997).
38. P. Muller, Bull. Astron. Paris **16**, 263 (1952).
39. P. Baize, Astron. Astrophys., Suppl. Ser. **26**, 177 (1976).
40. W. Rabe, Astron. Nachr. **276**, 262 (1948).
41. I. I. Balega, Y. Y. Balega, V. A. Vasyuk, and J. J. McManus, ASP Conf. Ser. **32**, 469 (1992).
42. G. Zeller, Ann. Sternw. Wien **26**, 111 (1965).
43. D. Pourbaix, Astron. Astrophys., Suppl. Ser. **145**, 215 (2000).
44. W. D. Heintz, Astron. J. **89**, 1068 (1984).
45. W. I. Hartkopf, Astron. J. **111**, 370 (1996).
46. P. Baize, Astron. Astrophys., Suppl. Ser. **92**, 31 (1992).
47. G. D. Gatewood, I. Han, J. K. de Jonge, C. T. Reiland, and D. Pourbaix, Astrophys. J. **549**, 1145 (2001).
48. I. I. Balega, Yu. Yu. Balega, K.-Kh. Khofman, *et al.*, Pis'ma Astron. Zh. **25**, 910 (1999) [Astron. Lett. **25**, 797 (1999)].
49. P. Eggleton and L. Kiseleva, NATO ASI Ser. C. Math. Phys. Sci. **477**, 345 (1996).
50. H. A. McAlister, W. I. Hartkopf, D. J. Hutter, and O. G. Franz, Astron. J. **93**, 688 (1987).
51. P. Hut, Astrophys. J. **403**, 256 (1993).
52. L. Kiseleva, P. Eggleton, and S. Mikkola, Mon. Not. R. Astron. Soc. **300**, 292 (1998).
53. W. D. Heintz, Veroff. Sternw. Munchen **7**, 7 (1965).
54. M. Walbaum and J.-L. Duvent, L'astronomie **97**, 277 (1983).
55. T. ten Brummelaar, B. D. Mason, H. A. McAlister, *et al.*, Astron. J. **119**, 2403 (2000).
56. D. W. MacCarthy, *Nearby Stars and the Stellar Luminosity Function,* Ed. by A. G. D. Philip and A. R. Upgren (Pergamon, New York, 1983), p. 107.
57. W. D. Heintz, Veroff. Sternw. Munchen **7**, 34 (1967).
58. D. J. Zulevic, Bull. Astron. Observ. Belgrade **150**, 117 (1994).
59. P. Mansbach, Astrophys. J. **160**, 135 (1970).

Translated by A. Dambis

Astronomy Reports, Vol. 49, No. 3, 2005, pp. 217–225. Translated from Astronomicheskiĭ Zhurnal, Vol. 82, No. 3, 2005, pp. 247–255.

Atmospheric Elemental Abundances for the Components of the Multiple System ADS 11061. 41 Draconis

Yu. Yu. Balega[1], V. V. Leushin[1], and G. Weigelt[2]

[1] *Special Astrophysical Observatory, Russian Academy of Sciences, Nizhniĭ Arkhyz, Karachaĭ-Cherkessian Republic, 357147 Russia*

[2] *Max-Planck-Institut für Radioastronomie, Auf dem Hügel 69, Bonn, 53121 Germany*

Received March 25, 2004; in final form, September 20, 2004

Abstract—We obtained speckle interferometric and spectroscopic observations of the system 41 Dra during its periastron passage in 2001. The components' lines are resolved in the spectral interval 3700–9200 Å. The observed wavelength dependence of the brightness difference between the components is used to estimate the $B-V$ indices separately for each of the components: $B-V=0.511$ for component a and $B-V=0.502$ for component b. We derived improved effective temperatures of the components from their $B-V$ values and hydrogen-line profiles. The observations can be described with the parameters for the components $T^{\rm a}_{eff}=6370$ K, $\log g^{\rm a}=4.05$ and $T^{\rm b}_{eff}=6410$ K, $\log g^{\rm b}=4.20$. The iron, carbon, nitrogen, and oxygen abundances in the atmospheres of the components are $\log N({\rm Fe})^{\rm a}=7.55$, $\log N({\rm Fe})^{\rm b}=7.60$, $\log N({\rm C})^{\rm a}=8.52$, $\log N({\rm C})^{\rm b}=8.58$, $\log N({\rm N})^{\rm a}=8.05$, $\log N({\rm N})^{\rm b}=7.99$, $\log N({\rm O})^{\rm a}=8.73$, $\log N({\rm O})^{\rm b}=8.76$. © *2005 Pleiades Publishing, Inc.*

1. INTRODUCTION

The quadruple system ADS 11061 contains two spectroscopic binaries, 40 Dra and 41 Dra, orbiting their common center of mass with a period of several tens of thousands of years and an apparent orbital semiaxis that varies from 10^3 to 10^4 AU [1]. The periods of the inner orbits of the 40 Dra and 41 Dra pairs are 10.5 and 1246.7 days [2]. The system is hierarchical and probably dynamically stable. All its components have spectral types of F5–F7. The iron abundance estimate of [3] indicates that ADS 11061 belongs to the young disk population, and that its age does not exceed 2.5 billion years. In late evolutionary stages, such stars become giants with luminosities only slightly different from those of the main-sequence stars.

The system is of special interest due to the very high orbital eccentricity of the 41 Dra pair: $e=0.9754\pm0.0001$ [2]. Their motion has been studied using both spectroscopic and interferometric methods, and the combined orbit's parameters are accurately known. For example, despite the system's long period, the epoch of periastron passage is known to within about 10 minutes. At periastron, the components of the pair approach each other to a distance of about 10 stellar radii. The high eccentricity raises the question of how such a pair could be formed and why its orbit has not been circularized by the action of tidal forces over the system's lifetime, as has happened for 40 Dra. One possible scenario of the origin and dynamic evolution of ADS 11061 was suggested in [2], but the situation is far from completely clear. In the recent periastron passage of 41 Dra in May–June 2001, it was possible to obtain integrated spectra in which the components' spectra were fully resolved during a comparatively short time interval (±15 days from periastron). This made it possible to obtain reliable information on the atmospheric chemical compositions of each of the stars.

Analyses of the orbit of the 41 Dra pair yielded the components' masses, $M^{\rm a}=(1.39\pm0.15)M_\odot$ and $M^{\rm b}=(1.30\pm0.14)M_\odot$, and the system's dynamic parallax [2]. An accurate parallax is crucial for determining the star's luminosity and, provided the temperatures are known, the components' radii. Essentially all estimates of π are close to $\pi=0.023''$ [1–6], whereas the parallax of 41 Dra in the HIPPARCOS catalog is $0.01884''$ [7], much lower than this value. The HIPPARCOS value is probably wrong, since the measurements did not take into account the system's binarity. Thus, the probable distance to the system is 44.6 ± 1.0 pc.

Below, we present the results of our estimates of the components' temperatures and of the iron, carbon, nitrogen, and oxygen abundances in their atmospheres based on spectra taken with the echelle spectrographs of the 6 m and Zeiss-1000 telescopes

1063-7729/05/4903-0217$26.00

Table 1. Brightness differences between the components of 41 Dra

λ, Å/$\Delta\lambda$, Å	$\Delta m \pm$ uncertainty	Date
5000	$0.40^m \pm 0.04^m$	2001.2713
5450/300	0.48 ± 0.03	1998.7769
6000	0.46 ± 0.05	2001.2713
6050/240	0.20 ± 0.10	1993.3492
6050/240	0.30 ± 0.10	1993.7646
6050/240	0.30 ± 0.10	1993.8437
6560/300	0.38 ± 0.05	1994.7129
7000	0.44 ± 0.10	2001.2713
8500/300	0.41 ± 0.14	2001.2713
12390/1380	0.47 ± 0.20	2000.7800
12390/1380	0.55 ± 0.20	2001.1920
16480/3170	0.46 ± 0.20	2000.7800
21910/4110	0.47 ± 0.10	1996.2667

of the Special Astrophysical Observatory (Russian Academy of Sciences) and the Zeiss-2000 telescope of the International Center for Astronomical, Medical, and Ecological Research (Mt. Terskol) [8–11]. The spectrographs have resolutions from 15 000 to 100 000 and cover the spectral range from 3700 Å to 9200 Å. We also analyze the brightness differences of the components of 41 Dra estimated over a wide wavelength range via speckle interferometry and compare these to the spectroscopic data.

2. EFFECTIVE TEMPERATURES OF THE COMPONENTS OF 41 DRA

Earlier [12], we determined the effective temperatures of the system's components from the continuum spectral energy distribution of the system [13] and the equivalent widths and profiles of the observed hydrogen lines. However, we noted certain discrepancies in the data. Thus, these earlier results need to be verified and refined. For this purpose, we use color indices in the UBV system, estimates of the brightness differences of the components obtained from speckle interferometry, and ratios of line depths in the components' spectra measured when the lines for the two components can be resolved.

Though the $B-V$ values for 41 Dra in various catalogs [14, 15] differ slightly, it is reasonable to adopt the combined color index for the system $B-V = 0.507 \pm 0.001$.

We noted in [12] that the speckle-interferometric brightness difference between the components was, on average, $\Delta m = 0.426 \pm 0.028$. However, it is very important to find the wavelength dependence of this difference in order to determine the individual color indices and temperatures of the components. For this purpose, we collected all the speckle-interferometric estimates of Δm obtained with the 6-m telescope, shown in Table 1. These lead to the following wavelength dependence for Δm:

$$\Delta m = 0.330 + 0.863 \times 10^{-5}\,[\text{Å}^{-1}] \times \lambda\,[\text{Å}].$$

This means that, at the center of the B band (λ4400 Å), $\Delta m^{\mathrm{B}} = 0.368$, and at the center of the V band (λ5500 Å), $\Delta m^{\mathrm{V}} = 0.377$.

We measured the ratios of the central depths of unblended lines of the system's components using spectra covering the wavelength range from 3700 to 9200 Å obtained at phases close to periastron. The central depths of absorption lines in the combined spectrum of the system are related to the components' luminosities as

$$\frac{R^{\mathrm{a},obs}}{R^{\mathrm{b},obs}} = \frac{E^{\mathrm{a}}_\lambda}{E^{\mathrm{b}}_\lambda}\frac{R^{\mathrm{a}}}{R^{\mathrm{b}}},$$

where R^{a}, R^{b} and $R^{\mathrm{a},obs}$, $R^{\mathrm{b},obs}$ are the actual and observed central line depths, respectively. If the physical characteristics and chemical compositions of the components are similar, then

$$R^{\mathrm{a}} \approx R^{\mathrm{b}} \quad \text{and} \quad E^{\mathrm{b}}/E^{\mathrm{a}} = R^{\mathrm{b},obs}/R^{\mathrm{a},obs}.$$

Our measurements of some 300 lines show that these ratios are wavelength-dependent:

$$E^{\mathrm{b}}_\lambda/E^{\mathrm{a}}_\lambda = 0.73 - 0.54 \times 10^{-5}\,[\text{Å}^{-1}] \times \lambda\,[\text{Å}].$$

Transforming the luminosity ratios into magnitude differences, we obtain

$$\Delta m^{\mathrm{B},obs} = 0.378 \pm 0.008$$
$$\text{and } \Delta m^{\mathrm{V},obs} = 0.387 \pm 0.008,$$

in fairly close agreement with the speckle-interferometric Δm estimates.

The assumption that the B and V magnitudes for the system's components are related as

$$B^{\mathrm{b}} = B^{\mathrm{a}} + \Delta m^{\mathrm{B},obs} \text{ and } V^{\mathrm{b}} = V^{\mathrm{a}} + \Delta m^{\mathrm{V},obs}$$

is a good approximation. In this case, the system's observed $B-V$ color index will be

$$B-V = (B^{\mathrm{a}} - V^{\mathrm{a}}) - 2.5\log\frac{1+10^{-0.4\Delta m^{\mathrm{B},obs}}}{1+10^{-0.4\Delta m^{\mathrm{V},obs}}},$$

and $B^{\mathrm{b}} - V^{\mathrm{b}} = B^{\mathrm{a}} - V^{\mathrm{a}} + (\Delta m^{\mathrm{B},obs} - \Delta m^{\mathrm{V},obs})$.

Substituting the observed values into these relations, we can derive the color indices for each of the components in the 41 Dra system:

component a: $B-V = B^{\mathrm{a}} - V^{\mathrm{a}} = 0.511$,

component b: $B-V = B^{\mathrm{b}} - V^{\mathrm{b}} = 0.502$.

Using models with normal chemical composition and an atmospheric turbulent velocity of 2 km/s of Kurucz [16], we obtain for the components' effective temperatures

component a: $T_{eff}^{a} = 6370 \pm 20$ K,

component b: $T_{eff}^{b} = 6410 \pm 20$ K.

These temperatures are slightly lower than those we derived in [12], and close to the estimates of T_{eff} and $B - V$ obtained from evolutionary tracks [2].

Using the masses and luminosities derived from the orbital motion, the parallax presented in [2], and our T_{eff} estimates, we find the components' surface gravities to be

component a: $\log g^{a} = 4.05 \pm 0.10$,

component b: $\log g^{b} = 4.20 \pm 0.10$.

3. RADIAL VELOCITIES OF THE COMPONENTS OF 46 DRA

To model the system's spectra and compare the synthesized spectra with observations at various orbital phases, we must obtain measurements of the components' radial velocities. We used stellar lines near Hα, using Earth-atmospheric lines as a comparison spectrum. A list of the measured lines is presented in Table 2.

We calculated the radial velocities and reduced them to the Sun using the Dech20 code of Galazutdinov [17]. The measured radial velocities of the components relative to the Earth, V_r^{a} and V_r^{b}, are presented in Table 3, together with the correction to the Sun V_a. The phases were calculated with the elements $T =$ JD 2449571.037 and $P = 1246.680^{d}$.

The derived radial velocities are in good agreement with those of [2], confirming the correctness of the orbital elements of 41 Dra presented in that paper.

4. HYDROGEN LINE PROFILES

Synthetic spectra of 41 Dra near Hα were calculated by summing theoretical profiles derived using the SintVa code developed by Tsimbal [18]. We calculated the theoretical profiles using models with $T_{eff} = 6370$ K and $\log g = 4.05$ for component a and $T_{eff} = 6410$ K and $\log g = 4.20$ for component b. The models were derived by interpolating the model grid of Kurucz [16]. The combined synthetic Hα spectrum was calculated for four phases before and after the periastron passage in 2001. We used the components' radial velocities from Table 3 to take into account wavelength shifts in the observed spectrum. The rotational speeds of the components ($v \sin i$) needed to calculate the synthetic spectrum were determined from absorption lines of metals. The rotational speeds of both components are close to 8.5 km/s. The turbulent velocities in the components' atmospheres were determined in [3] to be $V_t^{a} = 2.15$ km/s and $V_t^{b} = 1.70$ km/s. When summing the spectra, we assumed a brightness ratio for the components of $E^{b}/E^{a} = 0.68$.

Table 2. Lines used to measure the components' radial velocities

Stellar lines		Atmospheric lines
6526.653 SiI	6575.037 FeI	6532.359 H_2O
6546.239 FeI	6583.710 SiI	6536.720 H_2O
6554.223 TiI	6586.308 NiI	6542.313 H_2O
6555.463 SiI	6587.610 C I	6547.705 H_2O
6559.588 TiII	6592.926 FeI	6548.622 H_2O
6562.808 Hα	6593.884 FeI	6552.629 H_2O
6569.216 FeI	6597.571 FeI	6557.171 H_2O
6571.174 FeI	6604.600 ScII	6572.086 H_2O
6572.779 CaI	6608.044 FeI	6574.852 H_2O
6574.228 FeI	6609.118 FeI	6599.324 H_2O

The figure shows a comparison of the calculated and observed profiles, together with theoretical profiles we calculated for a binary whose components both have $T_{eff} = 6500$ K and $\log g = 4.00$, with the same brightness ratios, turbulent velocities, and radial velocities as for the first version. At all phases, the observed Hα profiles are confined within the range of the theoretical results. However, the agreement with the model having $T_{eff} = 6370$ K and $\log g = 4.05$ for component a and $T_{eff} = 6410$ K and $\log g = 4.20$ for component b is appreciably better. This confirms the correctness of our choice of atmospheric parameters for the components of the 41 Dra system.

5. ATMOSPHERIC IRON ABUNDANCES OF THE COMPONENTS OF 41 DRA

We determined the iron abundances from the equivalent widths of 50 FeI lines and 38 FeII lines using spectra taken near periastron, when the lines of components a and b were clearly resolved. The equivalent widths of these lines, along with the atomic parameters and $\log N(\mathrm{Fe})$ values for each line and at various phases, are presented in [3], where we also describe the technique used to determine $\log N(\mathrm{Fe})$. The calculations were performed with the KONTUR code [19]. Using models with $T_{eff} = 6575$ and $\log g = 4.08$ for component a and $T_{eff} = 6600$ and $\log g = 4.26$ for component b yielded

Table 3. Radial velocities of the components of 41 Dra

Spectrum	Date	JD	Phase	$V_r^{\rm a}$, km/s	$V_r^{\rm b}$, km/s	V_a, km/s
z3818	14.11.2000	2451862.6090	0.8381	11.86 ± 1.52	1.85 ± 1.12	4.27
z3819	14.11.2000	2451862.6924	0.8382	11.13 ± 1.32	1.92 ± 1.32	4.28
t05311	20.01.2001	2451929.6299	0.8916	13.89 ± 1.67	-2.15 ± 1.22	-3.45
t05312	20.01.2001	2451929.6715	0.8917	13.54 ± 1.77	-2.07 ± 1.35	-3.46
t05413	21.01.2001	2451930.5882	0.8924	14.12 ± 1.85	-2.43 ± 1.56	-3.55
o05a	09.06.2001	2452070.4215	0.0046	-27.12 ± 1.09	44.85 ± 1.38	-1.33
t11406	26.11.2027	2452605.4215	0.4337	5.92 ± 1.37	5.48 ± 1.37	2.94

$\log N({\rm Fe}) = 7.66$ (component a) and $\log N({\rm Fe}) = 7.72$ (component b), which are slightly higher than the solar iron abundance ($\log N({\rm Fe})_\odot = 7.50$). This paper's refined effective temperatures and surface gravities for the components ($T_{eff}^{\rm a} = 6370$ K and $\log g^{\rm a} = 4.05$, $T_{eff}^{\rm b} = 6410$ K and $\log g^{\rm b} = 4.20$) lead to abundances much closer to the solar value.

The lines of neutral iron, FeI, gave the atmospheric abundances for the components

component a: $\log N({\rm Fe}) = 7.582 \pm 0.044$,

component b: $\log N({\rm Fe}) = 7.593 \pm 0.032$.

The abundances derived from lines of ionized iron, FeII, are

component a: $\log N({\rm Fe}) = 7.530 \pm 0.039$,

component b: $\log N({\rm Fe}) = 7.613 \pm 0.045$.

The rms errors of the average values describe the internal uncertainties of the results, which coincide within the errors. Thus, the system's iron overabundance relative to the Sun, if present, does not exceed +0.1dex.

Note that any further decrease in the effective temperatures for the model atmospheres would lead to poorer coincidence of the $\log N({\rm Fe})$ values derived from ions with different ionization stages. For a model temperature of 6100 K, the difference in the iron abundances derived for component a from the FeI and FeII lines is 0.13dex, and that for component b is 0.27dex, which are much larger than the uncertainties. Thus, we consider our atmospheric parameters to be confirmed by the ionization relations.

6. ATMOSPHERIC CARBON, NITROGEN, AND OXYGEN ABUNDANCES OF THE COMPONENTS OF 46 DRA

The abundances of carbon, nitrogen, and oxygen are largely determined by the evolutionary status of the star, and are an important source of information about the star's origin and history. The amount of carbon and nitrogen in stars more massive than the Sun determines the rate of hydrogen-burning nuclear reactions in the CN cycle, and thus the rate of the star's evolution. In addition, carbon, nitrogen, and oxygen, the most abundant elements in normal stars heavier than hydrogen and helium, determine the internal structure of the atmosphere and of the star as a whole. At the same time, the comparative poorness of these elements' line spectra introduces considerable difficulties in determining their abundances. For this reason, the vast majority of papers analyzing C, N, and O abundances in stellar atmospheres are based on measurements of one or two lines of each element in the stellar spectra. This makes it important to measure each carbon, nitrogen, and oxygen line present in the spectrum in order to more accurately derive the abundances. Correctly taking into account the physical conditions under which the analyzed spectral lines are formed is also important.

Our echelle spectra (3700–9200 Å) were acquired near the periastron passage, when the components' spectral lines were resolved, enabling us to identify and measure relatively many CI, NI, and OI lines in the spectrum of each of the system's components.

Table 4 presents the parameters of the CI lines measured in the spectrum of the 41 Dra system, together with the equivalent widths, W_λ (in mÅ), and carbon abundances, $\log N({\rm C})$, for each of the components. We determined W_λ for each of the components from the $W_\lambda^{{\rm a},obs}$ and $W_\lambda^{{\rm b},obs}$ values measured for the resolved lines assuming the brightness ratio $l = E^{\rm b}/E^{\rm a} = 0.68$. The actual equivalent widths in the spectra of the components are given by the relations $W_\lambda^{\rm a} = 1.68 W_\lambda^{{\rm a},obs}$ and $W_\lambda^{\rm b} = 2.50 W_\lambda^{{\rm b},obs}$.

The model atmospheres and the techniques used to derive the abundances were the same as those used in our analysis of the iron lines. The $\log gf$ values were mainly taken from the VALD list [20].

Table 4. Line parameters, CI equivalent widths, and carbon abundances in the atmospheres of components a and b of 41 DRA

λ, Å	ε_i, eV	$\log gf$	W_λ^a, mÅ	$\log N(\mathrm{C})^a$	W_λ^b, mÅ	$\log N(\mathrm{C})^b$
4762.31	7.48	−2.46	15.4	8.51	15.6	8.51
4762.53	7.48	−2.34	16.6	8.37	17.1	8.38
4792.66	7.95	−2.79	8	8.71	8	8.70
4815.22	7.95	−2.13	7.4	8.00	8	8.03
4815.48	7.95	−2.42	8.2	8.52	8.2	8.51
4817.37	7.48	−3.04	8.4	8.65	11	8.74
4926.43	8.54	−1.97	6.8	8.55	7.5	8.55
4932.05	7.68	−1.88	59.4	8.89	55.5	8.64
5039.05	7.95	−1.79	19.7	8.23	23	8.37
5039.10	7.95	−2.29	10	8.51	11	8.52
5040.12	7.95	−2.3	7	8.23	10.5	8.52
5052.17	7.68	−1.65	59	8.69	63.5	8.76
5380.34	7.68	−1.84	49.2	8.72	40	8.59
5515.55	8.85	−2.34	2.9	8.76	2.9	8.76
5793.12	7.95	−2.06	18.4	8.56	24	8.66
5800.60	7.95	−2.34	8.7	8.50	12	8.59
6586.27	9.00	−1.89	3.8	8.53	3.2	8.52
6587.61	8.54	−1.6	17.4	8.55	18.4	8.57
6588.64	9.17	−2.2	1.9	8.71	1.8	8.68
6591.46	8.85	−2.41	3	8.69	3.5	8.72
6595.24	8.85	−2.41	2.8	8.67	2.5	8.64
6602.41	8.85	−2.38	5	8.83	3.2	8.68
6605.78	8.85	−2.31	1.1	8.51	1.2	8.38
6611.35	8.85	−1.84	2.5	7.97	3.2	8.12
7116.99	8.65	−0.91	40	8.48	42	8.52
7119.66	8.64	−1.15	31.9	8.55	35	8.60
7132.11	8.65	−2.2	3.4	8.53	7	8.67
9061.43	7.48	−0.35	214	8.69	224	8.82
9062.49	7.48	−0.46	185.4	8.58	195.4	8.72
9078.29	7.48	−0.58	160.4	8.48	187.4	8.76
9088.52	7.48	−0.43	167.5	8.40	177.5	8.56
9094.83	7.49	0.15	218	8.26	228	8.44
9111.80	7.49	−0.3	184.9	8.45	225	8.78

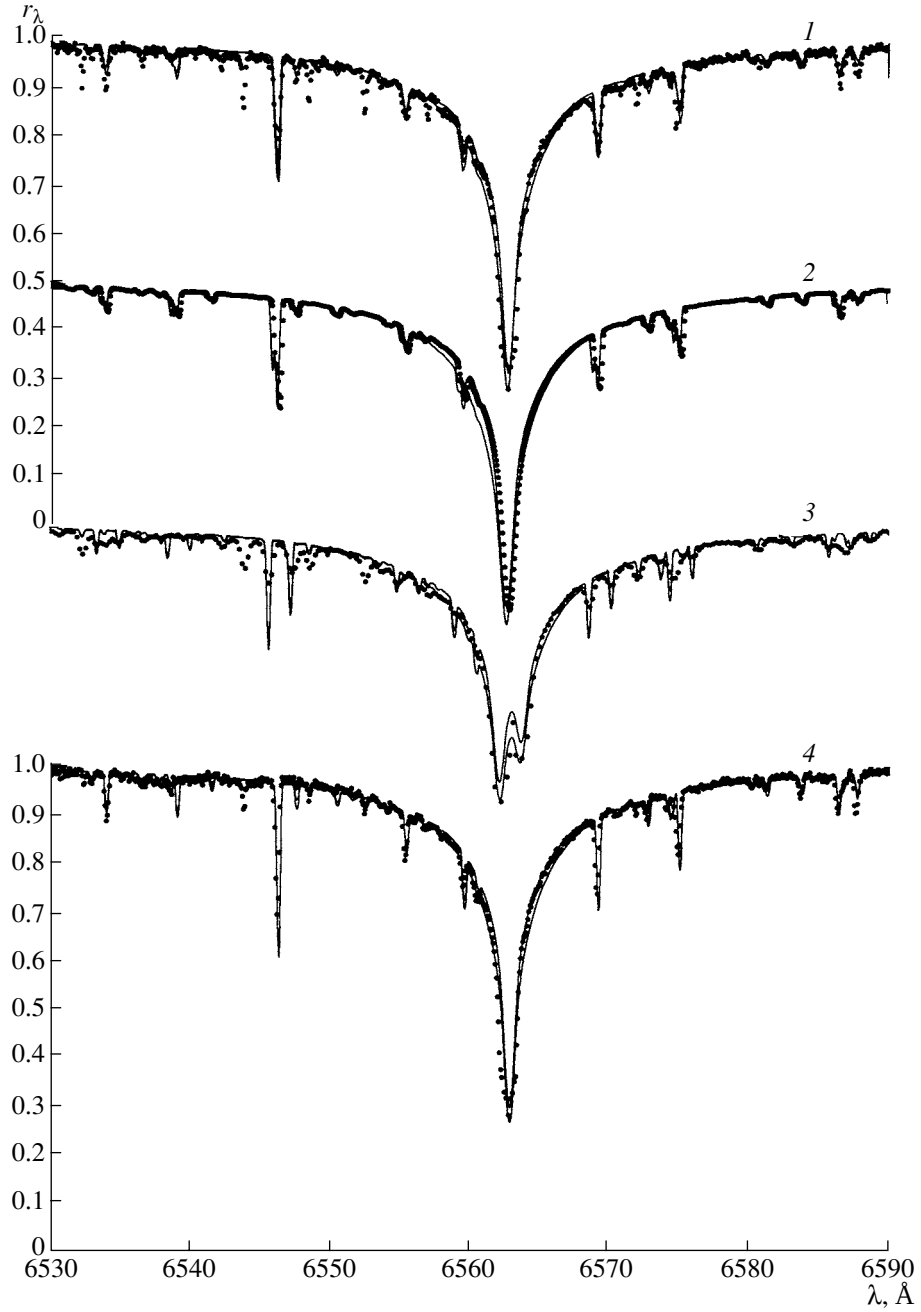

Comparison of observed (dots) and synthetic (solid curves) spectra of 41 Dra. The upper theoretical spectrum was calculated for $T^{\rm a}_{eff} = 6370$ K, $\log g^{\rm a} = 4.05$ and $T^{\rm b}_{eff} = 6410$ K, $\log g^{\rm b} = 4.20$. The lower theoretical spectrum was calculated for $T_{eff} = 6500$ K and $\log g = 4.00$. The spectra correspond to phases (*1*) 0.83, (*2*) 0.89, (*3*) 0.00, (*4*) 0.43.

Our equivalent-width calculations included four broadening mechanisms for the absorption coefficient: radiation damping, Doppler broadening, broadening due to the quadratic Stark effect, and van der Waals broadening. These effects enter the absorption coefficient as:

$$a = (\Delta\lambda_R + \Delta\lambda_{st} + \Delta\lambda_w)/\Delta\lambda_D,$$
$$v = (\Delta\lambda + d)/\Delta\lambda_D,$$

where $\Delta\lambda_R$ is the line width due to radiation damping, $\Delta\lambda_{st}$ is the Stark width, $\Delta\lambda_w$ is the van der Waals width, and d is the Stark displacement.

$\Delta\lambda_w$ can be calculated using the approximate formula of Unsold:

$$\Delta\lambda_w = \lambda^2/(4\pi c)\mathrm{C}_6^{0.4} \times 34N(\mathrm{HeI})(8kT/\pi m_H)^{0.3}.$$

Table 5. Line parameters, NI equivalent widths, and nitrogen abundances in the atmospheres of components a and b

λ, Å	ε_i, eV	$\log gf$	W_λ^a, mÅ	$\log N(\mathrm{N})^a$	W_λ^b, mÅ	$\log N(\mathrm{N})^b$
4253.39	10.34	−1.37	7.5	8.66	2	7.99
7442.30	10.33	−0.38	9.4	7.98	10	8.00
8184.86	10.33	−0.29	7.6	7.87	5.8	7.60
8188.01	10.32	−0.29	16.8	8.15	23	8.35
8216.33	10.34	0.13	21.2	7.92	16	7.66
8680.28	10.34	0.35	30.9	7.93	38.2	8.06
8683.40	10.33	0.09	26.5	8.04	28.5	8.07
8686.15	10.33	−0.3	19.6	8.17	23.8	8.29
8703.25	10.33	−0.32	8.4	7.85	8.5	7.80
8711.71	10.33	−0.23	16.1	8.02	12.5	7.92
8718.83	10.34	−0.34	11.2	7.97	18.5	8.17

Table 6. Line parameters, OI equivalent widths, and oxygen abundances in the atmospheres of components a and b

λ, Å	ε_i, eV	$\log gf$	W_λ^a, mÅ	$\log N(\mathrm{O})^a$	W_λ^b, mÅ	$\log N(\mathrm{O})^b$
6155.96	10.74	−1.36	1.9	8.83	2.4	8.86
6155.97	10.74	−1.01	3.6	8.78	4.8	8.83
6155.98	10.74	−1.12	3	8.80	3.8	8.84
6156.74	10.74	−1.49	1.5	8.84	1.7	8.84
6156.76	10.74	−0.9	4.6	8.78	5.2	8.80
6156.78	10.74	−0.69	6.3	8.75	7.1	8.76
6158.14	10.74	−1.84	1	8.91	–	–
6158.18	10.74	−1.00	4.9	8.85	–	–
6158.19	10.74	−0.41	11.6	8.77	–	–
7771.94	9.15	0.37	143.6	9.02	131.6	8.97
7774.16	9.15	0.22	123.3	8.93	117.6	8.94
7775.39	9.15	0.00	99.1	8.85	90.5	8.81
8446.25	9.52	−0.46	35.1	8.46	42.7	8.69
8446.36	9.52	0.24	51.7	8.09	63	8.31
8446.76	9.52	0.01	48	8.24	58.5	8.46

Here, line broadening due to collisions with neutral hydrogen and helium atoms is taken into account, and the constant C_6 can either be fixed (we took it from the VALD list) or calculated as

$$C_6 = 6.5 \times 10^{-9}((Z+1)^2 + 13.595)/\chi_{up})^{4/5},$$

where Z is the ion's charge and χ_{up} is the ionization potential for the upper level.

We used two techniques to take into account the quadratic Stark effect. For lines for which accurate calculations are available, we can specify the temperature-dependent electron-collision half-width, w, the ion-collision half-width, α, and the displacement, d [21]. The Stark line width and displacement can then be calculated for any point in the atmosphere using the equations

$$\Delta\lambda_{st} = 2wN_e \times 10^{-16}(1 + \alpha N_e^{1/4} A),$$

$$d = wN_e \times 10^{-16}(d/w + \alpha N_e^{1/4} B),$$

where $A = 1.75(1 - 0.75r)$, $B = 2(1 - 0.75r)$ for neutral atoms; $A = 1.75(1 - 1.2r)$, $B = 2(1 - 1.2r)$

for ions; and $r = 1.85\pi^{1/6}N_e^{1/6}(e^2/kT)^{1/2}$ is the Debye shielding radius.

If no data for w, α, and d are available, we use the following approximation to estimate the Stark broadening:

$$\Delta\lambda_{st} = \lambda^2/(4\pi c)\mathrm{C}_4 N_e,$$

where the constant C_4 is taken from the VALD list or calculated as

$$\mathrm{C}_4 = 10^{-8} \times ((Z+1)^2 + 13.595)/\chi_{up})^{5/2}.$$

The mean carbon abundances derived for the atmospheres of components a and b via a comparison of the observed and calculated equivalent widths are

component a: $\log N(\mathrm{C}) = 8.524 \pm 0.036$,

component b: $\log N(\mathrm{C}) = 8.576 \pm 0.031$.

There are many fewer nitrogen lines than carbon lines in the spectra of 41 Dra, and nearly all measurable lines that are not blended with lines of other elements have $\lambda > 8000$ Å. We could find only two NI lines in the shorter-wavelength part of the spectrum: λ4253.39 Å and λ7442.30 Å, which have equivalent widths lower than 10 mÅ. Table 5 collects for the NI lines the same data as those shown in Table 4 for the carbon lines. The mean atmospheric nitrogen abundances of components a and b are

component a: $\log N(\mathrm{N}) = 8.051 \pm 0.068$,

component b: $\log N(\mathrm{N}) = 7.991 \pm 0.034$.

We determined the atmospheric abundances of oxygen for the components of 41 Dra from lines of five triplets in the red, beginning with $\lambda > 6100$ Å. The parameters of the measured lines and $\log N(\mathrm{O})$ values for both components are presented in Table 6. The lines are fairly strong and essentially unblended, ensuring the reliability of our oxygen abundance determinations. The atmospheric abundances for each of the components are

component a: $\log N(\mathrm{O}) = 8.727 \pm 0.067$,

component b: $\log N(\mathrm{O}) = 8.761 \pm 0.055$.

7. CONCLUSION

Our spectroscopic and speckle-interferometric observations of the binary system 41 Dra in the hierarchical multiple system ADS 11061 obtained close to its periastron passage have enabled us to study the atmospheres of each of the components of 41 Dra separately. Within the uncertainties, all our observational data indicate that the effective temperatures of the system's components are 6370 K and 6410 K, respectively, for components a and b.

The virtually exact coincidence of the elemental abundances studied for the atmospheres of the two components of 41 Dra with those in the solar atmosphere and meteorites [22] is remarkable; the differences of several hundredths of a dex are probably due to equivalent-width errors and are not significant. This may mean that the chemical composition of the interstellar medium within a 50 pc radius of the Sun did not experience any considerable changes during the time from the formation of the solar system some five billion years ago until the formation of the 41 Dra system 2.5 billion years ago [2]. At the same time, the absence of any significant deviations of the C:N:O ratios in the atmospheres of the 41 Dra components from the solar values testify to a complete absence of mixing between the core and the atmosphere, despite the shock gravitational stresses periodically experienced by the stars during their periastron passages, when they approach each other to distances of only a few stellar radii.

ACKNOWLEDGMENTS

The authors thanks F.A. Musaev and D.O. Kudryavtsev for taking the spectra of 41 Dra. This study was supported by the Russian Foundation for Basic Research (project no. 01-02-16563-a).

REFERENCES

1. A. A. Kisilev and L. G. Romanenko, Astron. Zh. **73**, 875 (1996) [Astron. Rep. **40**, 795 (1996)].
2. A. Tokovinin, Yu. Yu. Balega, E. A. Pluzhnik, *et al.*, Astron. Astrophys. **409**, 245 (2003).
3. Yu. Yu. Balega, V. V. Leushin, and G. Weigelt, Bull. Spec. Astrophys. Obs. **54**, 5 (2003).
4. A. Tokovinin, Pis'ma Astron. Zh. **21**, 286 (1995) [Astron. Lett. **21**, 250 (1995)].
5. I. I. Balega, Yu. Yu. Balega, G. Fal'ke, *et al.*, Pis'ma Astron. Zh. **23**, 774 (1997) [Astron. Lett. **23**, 172 (1997)].
6. V. A. Al-Wardat, Yu. Yu. Balega, V. V. Leushin, *et al.*, *IAU Symp. No. 210: Modelling of Stellar Atmospheres, June 17–21, 2002, Uppsala, Sweden.*
7. *The Hypparcos and Tycho Catalogues*. ESA SP-1200, ESA, 1997.
8. F. A. Musaev, Pis'ma Astron. Zh. **19**, 776 (1993) [Astron. Lett. **19**, 315 (1993)].
9. V. E. Panchuk, I. D. Najdenov, V. G. Klochkova, *et al.*, Bull. Spec. Astrophys. Obs. **44**, 127 (1998).
10. V. E. Panchuk and S. V. Ermakov, Spets. Astrofiz. Obs., Nauchno-Tekh. Otchet No. 267 (1999).
11. F. A. Musaev, G. A. Galazutdinov, A. V. Sergeev, *et al.*, Kinematika Fiz. Nebesnykh Tel **15**, 282 (1999).
12. Yu. Yu. Balega, V. V. Leushin, and E. A. Pluzhnik, Bull. Spec. Astrophys. Observ. **51**, 61 (2001).
13. A. V. Kharitonov, V. M. Tereshchenko, and L. N. Knyazeva, *Spectrophotometric Catalogue of Stars* (Nauka, Alma-Ata, 1988).
14. H. L. Johnson and W. W. Morgan, Astrophys. J. **117**, 313 (1953).

15. V. G. Kornilov, I. M. Volkov, A. I. Zakharov, *et al.*, *Catalogue UBVR of Northern Sky Bright Stars* (Tr. Gos. Astron. Inst. Shternberga, Moscow, 1991), Vol. 63.
16. R. Kurucz, http://kurucz.harvard.edu
17. G. A. Galazutdinov, Preprint No. 92, SAO (Spec. Astrophys. Obs., 1992).
18. V. V. Tsimbal, *Magnetic Stars* (Spec. Astrophys. Obs., Russ. Acad. Sci., Nizhniĭ Arkhyz, 2003) (in press).
19. V. V. Leushin and G. P. Topil'skaya, Astrofiz. **22**, 121 (1985) [Astrophys. **21**, 74 (1985)].
20. F. Kupka, N. E. Piskunov, T. A. Ryabchikova, *et al.*, Astron. Astrophys., Suppl. Ser. **138**, 119 (1999).
21. G. Grim, *Spectral Line Widening in Plasma* (Mir, Moscow, 1978).
22. N. Grevesse and A. J. Sauval, *Solar Composition and Its Evolution—From Core to Corona*, Ed. by C. Frolich, M. C. E. Huber, S. K. Solanki, and R. von Steiger (Kluwer, Dordrecht, 1998), p. 161.

Translated by N. Samus'

Astronomy Reports, Vol. 49, No. 3, 2005, pp. 226–231. Translated from Astronomicheskiĭ Zhurnal, Vol. 82, No. 3, 2005, pp. 256–261.

Infrared Photometry of the Carbon Star RW LMi and an Axisymmetric Model for Its Dust Envelope

M. B. Bogdanov[1] and O. G. Taranova[2]

[1] *Chernyshevsky University, Saratov, Russia*

[2] *Sternberg Astronomical Institute, Universitetskiĭ pr. 13, Moscow, 119899 Russia*

Received April 6, 2004; in final form, September 20, 2004

Abstract—We have developed an axisymmetric model for the dust envelope of the carbon star RW LMi with a density distribution typical for the superwind stage using $JHKLM$ photometric data obtained in 1997–2003, supplemented by flux data at optical, mid-IR, and far-IR wavelengths. In contrast to earlier spherically-symmetric models, the model is able to reproduce the observed fluxes in all observed wavelength ranges, and provides a good agreement with the observational data. The estimated mass-loss rate is $\dot{M} = 1.2 \times 10^{-5}\ M_\odot/\mathrm{yr}$. The computed brightness distribution of the envelope in the near-IR is in satisfactory agreement with high-resolution observations, while the optical size is considerably larger than is observed. © *2005 Pleiades Publishing, Inc.*

1. INTRODUCTION

The carbon star RW LMi (=CIT 6=IRC+30219=AFGL 1403) is one of the brightest known objects in the mid-infrared. This provides evidence for the existence of a thick dust envelope that reprocesses the short-wavelength radiation of the central star. There have been several attempts by various authors, including ourselves, to compute models of this dust envelope assuming spherical symmetry [1–3]. In the latest [3], we considered a model of the envelope consisting of a mixture of spherical grains of amorphous carbon and silicon carbide (SiC). None of the sets of model parameters were able to fit the observed fluxes at all wavelengths, and a satisfactory agreement with the observations was obtained only for the mid- and far-IR. One possible explanation may be that the envelope has a nonspherical shape, e.g., due to the presence of a gap that is transparent to the short-wavelength radiation of the central star.

Some authors [6, 7] have suggested that RW LMi is in the early protoplanetary nebula stage, when the spherically-symmetric stellar wind typical of stars on the asymptotic giant branch (AGB) has already been transformed into a "superwind," and the envelope is ejected predominantly in the equatorial plane of the star, resulting in the formation of a gas–dust torus. The observed spectral energy distribution (SED) for such an object has a strong dependence on the inclination of the plane of the torus to the line of sight. At low inclinations, the central star is blocked by the dust, and the detected optical flux is determined by the radiation scattered in the envelope, which is emitted predominantly in the polar directions. This results in the bipolar structure that is typical for many protoplanetary nebulas. The infrared flux is formed by hot dust, which is concentrated mainly close to the equatorial plane of the torus. It is obvious that one-dimensional, spherically-symmetric models for the envelope are not adequate for such objects.

Our aim was to model the two-dimensional axisymmetric envelope of RW LMi using $JHKLM$ photometric data obtained by us in 1997–2003, supplemented with the optical and IR flux measurements of other authors. We have compared our model SED with both the observed SED and with other high-resolution observations.

2. OBSERVATIONAL DATA

We obtained infrared photometric data for the carbon star RW LMi using the 1.25-m telescope of the Crimean Laboratory of the Sternberg Astronomical Institute as a part of a program of studies of circumstellar dust envelopes. The observing method and results for 1986–1998 were published and analyzed in [3–5]. The rms errors for the $JHKLM$ photometric data for RW LMi obtained since 1994 do not exceed 0.03^m.

Figure 1 shows the observed variations of the IR fluxes of RW LMi at 1.25 μm (J) and 5 μm (M) for 1986–2003. The data plotted to the left of the dotted vertical line were used by us in [3] to calculate a spherically-symmetric model for the dust envelope of RW LMi. Figure 1 shows that, since the middle of 1998, periodic variations of the J flux have occurred against the background of a rising mean flux level,

1063-7729/05/4903-0226$26.00

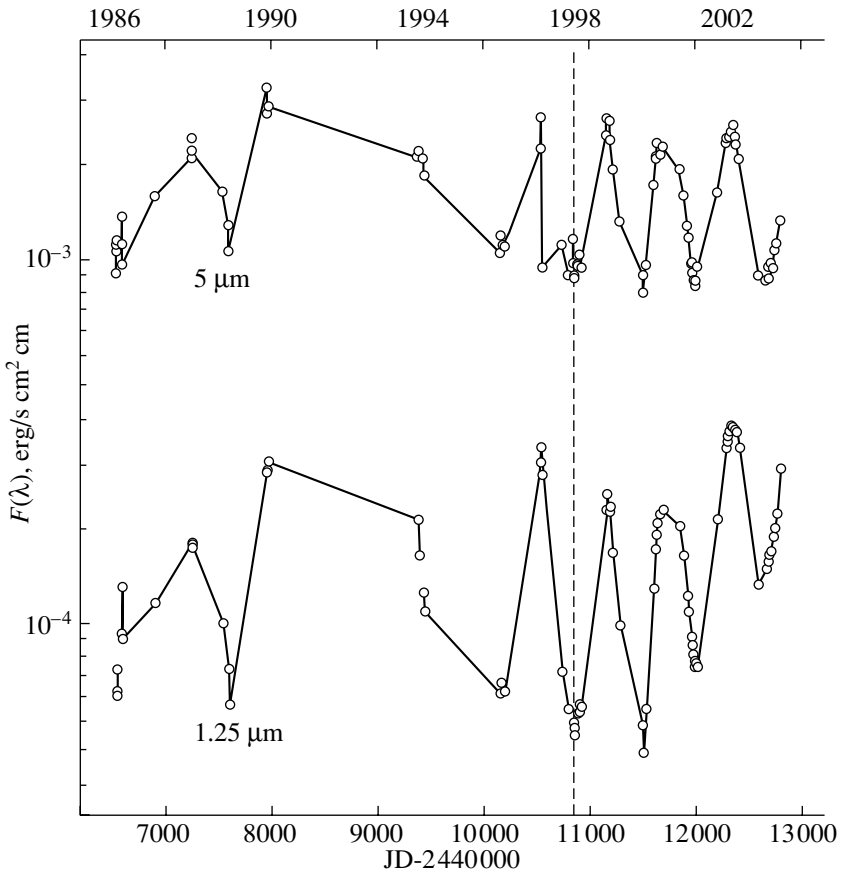

Fig. 1. Observed flux variations for RW LMi at 1.25 μm (J) and 5 μm (M) in 1986–2003. The data to the left of the dotted vertical line were used in our paper [3].

which increases by nearly a factor of three in 1998–2003. An analysis of the photometric peculiarities of RW LMi observed in 1986–2003 will be presented separately. In the present study, we used the mean *JHKLM* fluxes for 1997–2003, $F(\lambda)$, presented in the table. The table also lists the standard deviations σ and number of averaged values N, as well as the mean fluxes for 1986–1998, for comparison. We can see that the average *JHK* fluxes were higher in 1998–2003 than in 1986–1998, while no such increase in the 3.5 and 5-μm fluxes was observed (in fact, the fluxes in these wavebands even decreased slightly). We suggest that these flux variations were due to a decrease in the optical depth of the circumstellar dust envelope. The table also shows that the maximum flux increase in 1998–2003 was observed at 1.65 μm.

For comparison with the model, we used the optical and I photometric data from [8] along with our observations. The values of $F(\lambda)$ (in erg/s cm^2 cm) were derived from the average observed magnitudes using the out-of-atmosphere fluxes from [9]. In addition, we considered the longer-wavelength fluxes from the *Catalog of Infrared Observations*; the average values for the color-corrected IRAS fluxes were taken from [1, 10]. In Fig. 2, the logarithms of the observed fluxes are shown by open circles.

Along with spectrophotometric information, high-angular-resolution observations can be useful for comparisons with the model calculations. Optical images obtained with the Hubble Space Telescope and near-IR interferometric images obtained with the Keck-I telescope [11] using an aperture mask are available for RW LMi. In the blue (F439W) and yellow (F555W) filters, where scattering is especially strong, the influence of inhomogeneities in the dust distribution will blur the image. A bipolar structure consisting of two components separated by 0.2″ in positional angle 190° is clearly visible in the red filter (F675W, $\lambda_0 = 0.674$ μm, $\Delta\lambda = 0.089$ μm), providing evidence that the inclination of the axis of the dust torus to the line of sight is close to 90°. The left part of Fig. 3 shows the brightness distributions for this image plotted using contour levels at 50, 25, 12.5, 6.2, 3.1, 1.6, and 0.8% of the maximum brightness. The emission of the central star and parts of the dust torus that are closest to it dominate in the IR ($\lambda_0 = 3.083$ μm, $\Delta\lambda = 0.101$ μm). The IR brightness

Mean fluxes for RW LMi at various wavelengths derived from *JHKLM* photometry in 1986–1998 and 1997–2003

1986–1998				1997–2003		
λ, μm	$F(\lambda)$, 10^{-4} erg/s cm^2 cm	σ, 10^{-4} erg/s cm^2 cm	N	$F(\lambda)$, 10^{-4} erg/s cm^2 cm	σ, 10^{-4} erg/s cm^2 cm	N
1.25	1.20	0.12	40	1.63	0.12	59
1.65	3.25	0.32	41	4.96	0.36	59
2.2	7.99	0.71	43	10.0	0.72	61
3.5	21.2	1.50	42	20.0	1.33	60
5	14.3	0.92	42	10.0	0.71	60

distribution is plotted in the left part of Fig. 4 using the same contour levels as for the optical image.

3. CALCULATION OF THE DUST-ENVELOPE MODEL FOR RW LMi

We calculated an axisymmetric model for the envelope of RW LMi that describes the density distribution of the dust torus $\rho(r,\theta)$ using the three-parameter model for the dust envelope of a post-AGB star of [12]:

$$\rho(r,\theta) = \left(\frac{r}{r_1}\right)^{-B} [1 + A(1-\cos\theta)^F], \quad (1)$$

where r is the distance from the center of the star, θ is the angular distance from the direction toward the north pole, r_1 is the radius of the inner edge of the torus, and A, B, and F are free parameters. The radiative-transfer equation was solved using the 2-Dust code [13], which derives the radiation field and grain temperature in the envelope using the method of long characteristics, in which rays coming from all spatial directions are considered at each grid point. Such algorithms are often called "2.5 dimensional." After obtaining the main solution, the brightness distribution for selected wavelengths and the corresponding SED for various inclinations of the torus axis to the line of sight i can be calculated. We used the standard two-dimensional grid for the 2-Dust code, which has 45 radial points, most of which are concentrated toward the inner edge of the torus, and 8 polar grid points [13]. The radius of the outer edge of the torus was set to $r_2 = 60r_1$. The wavelength grid had 33 values from 0.3 to 500 μm.

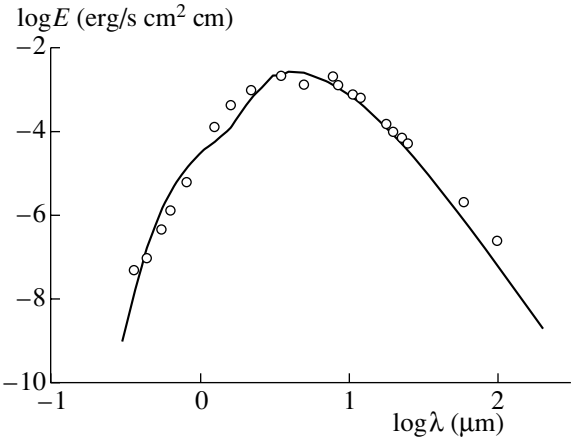

Fig. 2. Logarithms of the observed fluxes of RW LMi (open circles) as a function of the logarithms of their wavelengths. The solid curve shows the SED for the calculated model with a dust envelope.

Along with the inner radius r_1, the three parameters of the density distribution (1), and the optical depth of the envelope in the equatorial plane τ, the axisymmetric model for a given wavelength depends on the same parameters as the spherical model. These parameters determine the properties of the central star (luminosity L, effective temperature T_{eff}, and distance d) and of the dust (chemical composition, relative concentration, size distribution of the grains, optical constants). The total number of parameters is fairly large. In addition, the computational time for a model with one set of parameters using the 2-Dust code is about a factor of a hundred longer than the analogous computation for a spherical dust envelope model with the DUSTY code (version 2.0) using a similar grid and the algorithm described in [14, 15]. Therefore, it becomes especially important for the axisymmetric model to reduce the number of free parameters, if possible.

The absolute bolometric magnitude of RW LMi was determined from the period–luminosity relation for carbon stars [16] using the period $605^{\rm d}$ [8]. This magnitude is -5.18^m, which implies a luminosity for the star of $L = 9400\ L_\odot$, if the absolute magnitude of the Sun is 4.75^m [17]. We used the distance $d = 360$ pc found by us earlier [3], since it is consistent with independent estimates [18]. We assumed that a mixture of spherical grains of amorphous carbon and silicon carbide is present in the envelope, with

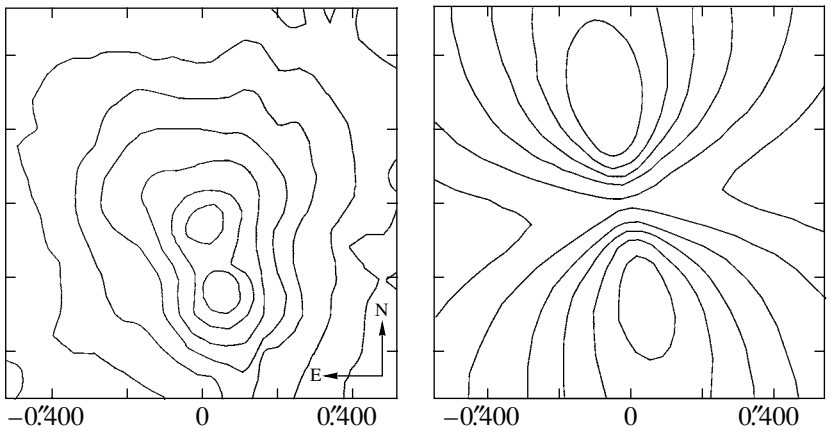

Fig. 3. Brightness distributions obtained from optical observations of RW LMi (left) and calculated using the stellar model with the dust envelope (right).

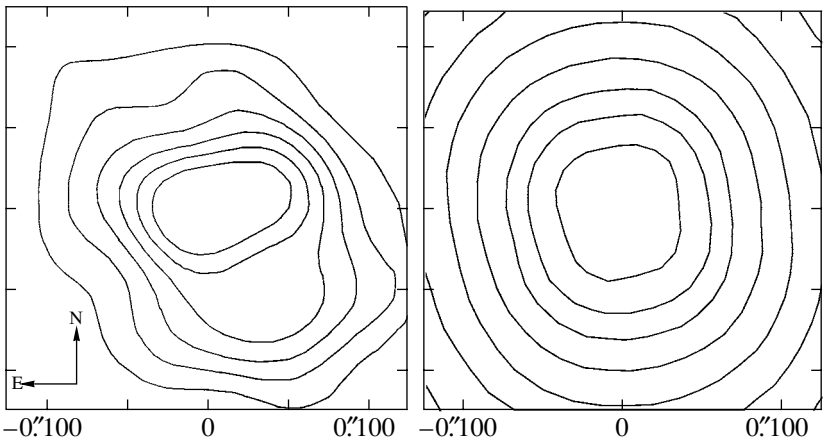

Fig. 4. Brightness distributions obtained from near-IR observations of RW LMi (left) and calculated using the stellar model with the dust envelope (right).

their relative abundances being 0.97 and 0.03, respectively. Such relative abundances are suggested by the appearance of the spectral feature at $\lambda = 11.3$ μm [3]. We adopted the law of Mathis, Rumpl, and Nordsieck [19] for the size distribution of the grains: $n(a) \propto a^{-q}$ for grains with radii $a_{\min} \leq a \leq a_{\max}$ and with $q = 3.5$, $a_{\min} = 0.005$ μm, and $a_{\max} = 0.25$ μm. The optical constants for α-SiC were taken from [20] and those for amorphous carbon from [21]. We assumed a Planck SED corresponding to the effective temperature of the star, $T_{eff} = 2700$ K, for the central source [3]. We also fixed two parameters of the density distribution (1): $B = 2$, corresponding to the condition of continuity for the spherically symmetric envelope, and $F = 1$.

Our fitting of the axisymmetric dust-envelope model for RW LMi resulted in the following parameters for the envelope. The optical depth in the equatorial plane at 11.3 μm is $\tau = 0.60$, the radius of the inner edge of the envelope is $r_1 = 2.1 \times 10^{14}$ cm, the average dust temperature at this edge is 1300 K, and $A = 19$. Thus, the mass of the dust ejected in the equatorial plane of the torus is a factor of twenty higher than the mass ejected in the polar direction. The total mass of dust in the stellar envelope is $1.8 \times 10^{-6}\ M_\odot$. The inclination of the torus axis to the line of sight is 88°. The SED for the model is shown by the solid curve in Fig. 2. Despite the presence of some discrepancies, the model is able to reproduce the observed fluxes in the entire analyzed spectral range, and the overall agreement with the observations is good.

For comparison with high-angular-resolution observations, we calculated the brightness distributions at 0.674 and 3.083 μm. We assumed that the point-spread function was determined by the diffraction for the round aperture (the Airy disk). The exact attainable resolution for interferometry with an aperture

mask is unknown. In the analysis of such observations in [11], the maximum-entropy method was applied, which makes it possible to increase the resolution over the diffraction limit. However, no more than a twofold increase in resolution is possible with the usual signal-to-noise ratios, and we adopted this factor for our analysis. We applied an algorithm based on a fast Hurtley transform [22] to convolve the model images with the point-spread function. The initial angular sizes of the model images were increased enough to eliminate limb effects. Contours of constant brightness in the calculated models for the dust envelope of RW LMi oriented in accordance with the position angle of the observed bipolar structure are shown on an appropriate scale in the right-hand panels of Figs. 3 and 4. In both figures, the coordinate origin coincides with the stellar center.

The shape of the IR brightness contours is in satisfactory agreement with the IR observations, but the angular size of the model bipolar structure in the optical is considerably larger than is observed. The model flux from the envelope at $\lambda = 0.674$ μm is also higher than the observed flux (Fig. 2). As is noted above, we expect more influence of fluctuations of the dust density in the optical, but such fluctuations are unlikely to lead to such a large difference between the images. The differences in the size and shape of the brightness contours are most likely due to some inadequacies of the model used to describe the dust torus. The fraction of the total energy emitted by RW LMi in the optical is not large, making it difficult to obtain a good agreement between the model and observed fluxes and images over a wide spectral range.

The 2-Dust code can be used to estimate the dust mass-loss rate for a given model, $\dot{M}_{\rm d}$, assuming a constant expansion velocity for the envelope [13]. In reality, the expansion should accelerate, with the dust velocity being higher than the gas velocity. A self-consistent procedure to determine the mass-loss rate and expansion velocity of an envelope was developed in [23]. We used this procedure in [3] to estimate the parameters of the spherically-symmetric wind of RW LMi that is formed by the action of radiation pressure on the dust and the resulting transfer of momentum to the gaseous medium. In the case considered here, we can obtain only a relatively crude estimate of $\dot{M}_{\rm d}$, adopting for the expansion velocity the average value $V = 17.4$ km/s, derived from radio observations of the CO emission [24]. The resulting dust mass-loss rate is $\dot{M}_{\rm d} = 2.4 \times 10^{-8}$ $M_\odot$/yr, which is very close to the estimate $\dot{M}_{\rm d} = 2.1 \times 10^{-8}$ $M_\odot$/yr obtained for our spherically-symmetric model of the envelope in [3]. Taking the gas-to-dust mass ratio in the envelope of RW LMi to be 500 [3], which is close to the average ratio for carbon stars [23], we estimate the total mass-loss rate to be 1.2×10^{-5} $M_\odot$/yr.

4. CONCLUSION

IR photometric observations of RW LMi obtained over the last six years show continuing variability of the brightness of this carbon Mira-type star, with the amplitude and period remaining nearly constant. At the same time, there has been an increase in the JHK fluxes, especially at 1.65 μm, accompanied by a decrease of the L and M fluxes. This behavior is probably due to variations of the density in the circumstellar dust envelope.

We have interpreted the observed SED of RW LMi using an axisymmetric dust-envelope model with a density distribution typical for the superwind stage. This model can describe the observed fluxes from the optical to the far-IR fairly well. The calculated IR brightness distributions are in satisfactory agreement with high-angular-resolution observations in the IR, but the size of the model optical image is appreciably larger than is observed in the optical.

The estimated mass-loss rate obtained assuming a constant envelope expansion velocity is $\dot{M} = 1.2 \times 10^{-5}$ $M_\odot$/yr, which is close to the rate found previous for a spherically-symmetric model of the dust envelope.

ACKNOWLEDGMENTS

The authors are grateful to Dr. T. Ueta for enabling us to use the 2-Dust code. This work was partially supported by the Federal Science and Technology Program "Astronomy."

REFERENCES

1. M. Rowan-Robinson, T. D. Lock, D. W. Walker, and S. Harris, Mon. Not. R. Astron. Soc. **222**, 273 (1986).
2. C. R. Marshall, D. A. Leahy, and S. Kwok, Publ. Astron. Soc. Pac. **104**, 397 (1992).
3. M. B. Bogdanov and O. G. Taranova, Astron. Zh. **76**, 780 (1999) [Astron. Rep. **43**, 684 (1999)].
4. O. G. Taranova, Astrofiz. **27**, 29 (1987) [Astrophys. **25**, 616 (1987)].
5. O. G. Taranova and V. I. Shenavrin, Pis'ma Astron. Zh. **25**, 860 (1999) [Astron. Lett. **25**, 750 (1999)].
6. S. R. Trammell, H. L. Dinerstein, and R. W. Goodrich, Astron. J. **108**, 984 (1994).
7. T. Ueta, M. Meixner, D. E. Moser, *et al.,* Astron. J. **125**, 2227 (2003).
8. A. Alksnis, Balt. Astron. **4**, 79 (1995).
9. V. L. Straizys, *Multicolor Stellar Photometry* (Mokslas, Vilnius, 1977), p. 312 [in Russian].
10. M. P. Egan and C. M. Leung, Astrophys. J. **383**, 314 (1991).

11. J. D. Monnier, P. G. Tuthill, and W. C. Danchi, Astrophys. J. **545**, 957 (2000).
12. M. Meixner, T. Ueta, M. Bobrowsky, and A. K. Speck, Astrophys. J. **571**, 936 (2002).
13. T. Ueta and M. Meixner, Astrophys. J. **586**, 1338 (2003).
14. Z. Ivezic and M. Elitzur, Mon. Not. R. Astron. Soc. **287**, 799 (1997).
15. Z. Ivezic and M. Elitzur, Mon. Not. R. Astron. Soc. **303**, 864 (1999).
16. M. A. T. Groenewegen and P. A. Whitelock, Mon. Not. R. Astron. Soc. **281**, 1347 (1996).
17. C. W. Allen, *Astrophysical Quantities* (Athlone, London, 1973; Mir, Moscow, 1977), p. 446.
18. M. Cohen and K. Hitchon, Astron. J. **111**, 962 (1996).
19. J. S. Mathis, W. Rumpl, and K. H. Nordsieck, Astrophys. J. **217**, 425 (1977).
20. B. Pegourie, Astron. Astrophys. **194**, 335 (1988).
21. V. G. Zubko, V. Mennella, L. Colangeli, and E. Bussoletti, Mon. Not. R. Astron. Soc. **282**, 1321 (1996).
22. M. B. Bogdanov, Astron. Zh. **70**, 201 (1993) [Astron. Rep. **37**, 105 (1993)].
23. M. A. T. Groenewegen, P. A. Whitelock, C. H. Smith, and F. Kerschbaum, Mon. Not. R. Astron. Soc. **293**, 18 (1998).
24. B. Zuckerman and H. M. Dyck, Astron. Astrophys. **209**, 119 (1989).

Translated by L. Yungel'son

Astronomy Reports, Vol. 49, No. 3, 2005, pp. 232–241. Translated from Astronomicheskiĭ Zhurnal, Vol. 82, No. 3, 2005, pp. 262–272.

IR Photometry of the Symbiotic Star BF Cyg: Detection of the Red Giant's Ellipsoidal Brightness Variability

B. F. Yudin†, V. I. Shenavrin, E. A. Kolotilov, A. A. Tatarnikova, and A. M. Tatarnikov

Sternberg Astronomical Institute, Universitetskiĭ pr. 13, Moscow, 119992 Russia

Received June 20, 2004; in final form, July 15, 2004

Abstract—We present the results of our IR photometric observations of the classical symbiotic star BF Cyg acquired in 1978–2003. The variability range in the J and K bands was $\sim 0.2^m$. A periodic component in the cool star's brightness variations is clearly visible, its period being half the orbital one and its J amplitude being $\sim 0.15^m$. This component is associated with the ellipsoidal shape of the red giant, which model calculations show fills its Roche lobe. This is required in order to reproduce ellipsoidal brightness variability with such a large amplitude: the calculated amplitude for a red giant filling 90% of its Roche lobe is half the observed value. At the same time, it was not possible to confidently chose the optimum component-mass ratio, $q = M_{giant}/M_{hot}$, and orbital inclination, i, from possible values in the ranges $q = 2$–4, $i = 70°$–$90°$. Including the contribution from the hot radiation sources (the hot component and ionized envelope), which vary with a period equal to the orbital period, has a considerable influence on the estimated parameters associated with the red giant's ellipsoidal brightness variations, and this contribution cannot be neglected. The deviations of the observed from the calculated light curve are irregular, with the rms deviation being $\sigma(\mathrm{O-C}) \approx 0.04^m$. © *2005 Pleiades Publishing, Inc.*

1. INTRODUCTION

Based on its outburst activity, BF Cyg was assigned to the group of classical symbiotic stars, whose prototype is Z And. During outbursts, its brightness grows over several months and then decreases over several years. Strong outbursts repeat once every few decades. The strongest outbursts have amplitudes reaching 3^m in the U band. During the strongest outbursts, some classical symbiotics, including BF Cyg, experience radical spectral changes: the high-excitation emission becomes much weaker or disappears completely, while the hot component begins to resemble a B–F supergiant [1, 2]. The most recent outburst of BF Cyg (1989–1992) was analyzed in detail in [3]. In particular, it was demonstrated that the hot component's luminosity increased only modestly (by a factor of ~ 2) during the outburst, while its temperature decreased from 60 000 to 7000 K.

Based on the intensity of its TiO absorption bands, the cool component of BF Cyg can be classified as an M4.5–M5.5 red giant [4, 5]. Its luminosity class (II or III) has not been firmly established. The strongest evidence for the star having luminosity class III is probably its low value of $V_{rot} \sin i$, which corresponds to a radius for the red giant $R_\mathrm{g} = 70 \pm 32 R_\odot$ [6]. In this case, the cool component will fill less than half its Roche lobe. However, their analysis of the time characteristics of an eclipse of the hot component observed in 1999 during a large outburst led Skopal *et al.* [7] to conclude that the red giant filled its Roche lobe ($R_\mathrm{g}/A = 0.54 \pm 0.02$), and hence was a bright giant of luminosity class II.

These two options are significantly different from the point of view of the character of the mass transfer between the symbiotic star's cool and hot components. In the former case, this will involve the capture of some of the red giant's stellar wind by the hot component, and in the latter, it will involve disk accretion. Model mechanisms for the hot component's outbursts will likewise be different (cf. [8] and references therein). Thus, determining the degree of Roche-lobe filling by the cool component is a fundamental problem in studies of classical symbiotic stars.

It is possible to obtain a radial-velocity curve only for the cool component of a symbiotic star, from radial-velocity measurements for absorption lines formed in its atmosphere, while the hot component does not produce any lines in the spectrum. All emission lines originate in the circumstellar envelope. Thus, observations can be used to estimate the mass function only for the cool component. To derive the masses of both components, we need some other methods to determine the component-mass ratio and orbital inclination.

The radial-velocity curve for the cool component of BF Cyg is given in [6]. High-resolution spectra

† Deceased.

1063-7729/05/4903-0232$26.00

were obtained near $\lambda \approx 1.62$ μm. The derived orbital parameters are $P_{orb} = 757.2 \pm 2.6$ days, $e = 0$, and $f(m) = 0.0239 \pm 0.0026$. BF Cyg is an eclipsing binary. The period of the star's visual brightness variations has been estimated to be 757.3 days [9] or 756.8 days [10].

The presence of a periodic component in the red giant's brightness variations with a period equal to half the orbital period would provide convincing evidence that the cool component fills its Roche lobe. These variations result from the ellipsoidal (pearlike) shape of the red giant, which is deformed by tidal distortions due to the hot companion. The amplitude of the ellipsoidal brightness variations measures the degree of Roche-lobe filling. Clearly, this effect should be investigated in the infrared, where the red giant of a classical symbiotic star dominates during the quiescent state.

IR monitoring of the recurrent symbiotic nova T CrB revealed the presence of ellipsoidal brightness variations with a J amplitude of $\sim 0.2^m$ [11]. Modeling taking into account the cool component's ellipsoidality effect yielded estimates of the component-mass ratio and the orbital inclination to the line of sight [12]. Ellipsoidal I brightness variations were detected for the classical symbiotic star CI Cyg [13].

We present here the results of our many-year monitoring of BF Cyg in the IR, where only a few brightness estimates were available until recently. Our main goal was to determine if the cool component's brightness variations included a periodic component with $P = P_{orb}/2$, due to the deformation of the red giant by tidal perturbations from its hot companion, and to determine the amplitude of this component if present. The presence of such a component with a fairly large amplitude would provide weighty evidence that the red giant's Roche lobe is filled, whereas the absence of such a component would support the view that the Roche lobe is not fully filled. We are also conducting systematic photometric and spectrophotometric observations of BF Cyg in the optical, and plan to present a detailed analysis of these data in a subsequent paper. We will use these data in the present paper only to a limited extent, as is required for our analysis for the red giant.

2. PHOTOMETRIC BEHAVIOR OF BF Cyg

We obtained $JHKLM$ photometric observations of the symbiotic star BF Cyg using the 1.25-m telescope of the Sternberg Astronomical Institute's Crimean station. The standard star used was BS 7417, which has brightnesses of $J = 1.01^m$, $H = 0.16^m$, $K = 0.16^m$, and $L = -0.01^m$. The uncertainties of the resulting brightness estimates were no larger than 0.03^m in J, H, and K and no larger than 0.06^m in L. Table 1 presents our $JHKL$ photometric data accumulated since 1978 (the results of our UBV photometry obtained since 1993 will be presented in a separate paper). Figure 1 shows the U and J light curves.

A strong outburst of the hot component of BF Cyg occurred during our observations, beginning in 1989. The outburst was also quite substantial in the infrared (Fig. 1), with the J brightness of BF Cyg increasing by $\sim 30\%$ over the star's mean brightness in quiescence. The brightening was the result of an increase in the hot component's luminosity by a factor of ~ 2 during the outburst, together with a strong decrease in its temperature, so that its photometric and spectroscopic properties resembled those of a hot supergiant [3]. Our spectrophotometric data suggest that the hot component was in the same state in 1987, as is indicated by the increased J brightness of BF Cyg at that time.

In 1993, the hot component of BF Cyg returned to its quiescent state and we decided to monitor the star in the IR with the best possible time coverage and minimum uncertainties, in order to study the character of the red giant's brightness variations. Since then, the uncertainties of our J and K brightness estimates have been no larger than 0.02^m, usually being $\sim 0.01^m$. We will now use this particular part of the light curve, beginning with JD 2449114 (May 6, 1993), to investigate the red giant's variability. These observations were favored by exemplary quiet behavior of the hot component right up until our most recent observations (see the U light curve in Fig. 1).

The vertical bars in Fig. 1 mark the epochs of U brightness minima (eclipses of the hot component and of part of the circumstellar envelope by the red giant) calculated using the formula

$$\mathrm{Min}\, U = 2\,449\,135 + 758.0^{\mathrm{d}} E. \qquad (1)$$

This ephemeris was derived from the U light curve of BF Cyg since 1993 via a periodogram analysis.

The amplitude of the J brightness variations was $\sim 0.2^m$, appreciably larger than the observational uncertainties. Thus, the cool component of BF Cyg is a variable star—an expected finding, given the red giant's late ($\sim$M5) spectral type. A linear approximation of the J light curve (the straight line segment in Fig. 1) shows that the red giant's mean J brightness increased by $\sim 0.04^m$ during our observations. A similar increase was shown by the K brightness, so that the mean $J - K$ color index remained unchanged at $\langle J - K \rangle \approx 1.35^m$.

For $E(B - V) = 0.4$ [10], the red giant's color index $\langle J - K \rangle_0$ indicates it should be assigned a spectral type of $\sim$M4, based on a comparison with

Table 1. *JHKLM* photometry of BF Cyg

JD 2440000+	*J*	*H*	*K*	*L*	JD 2440000+	*J*	*H*	*K*	*L*
3795			6.38	5.44	8115	7.32		6.05	
3835	7.73		6.41		8437	7.41		6.14	
3836	7.73		6.40		8528	7.25		6.18	
4033	7.69		6.48		8568	7.30	6.34	6.02	
4043	7.72				8790	7.43		6.31	
4151	7.60	6.84			8796	7.45		6.28	
4367	7.64				8790	7.43		6.31	
4414	7.71	6.73	6.40		8796	7.45		6.28	
4507	7.57	6.58			8790	7.43		6.31	
4807	7.58	6.63	6.23		8796	7.45		6.28	
5124	7.46				8823	7.50	6.55	6.18	5.90
5128	7.67	6.41	6.11		8850	7.55		6.20	
5133				5.32	8852	7.55		6.20	
5134				5.48	8878	7.43		6.09	5.69
5245			6.38		8879	7.38		6.13	5.73
5518	7.45	6.52	6.16		9114	7.62		6.31	5.95
5837	7.60				9144	7.69		6.34	6.01
5874	7.72	6.42		5.89	9235	7.58		6.25	5.90
5875			6.19	5.83	9294	7.59		6.24	
5876	7.72			5.83	9502	7.68	6.74	6.33	6.03
5879				5.74	9525	7.65		6.36	5.93
5931	7.61	6.57	6.17	5.81	9529	7.68	6.66	6.30	5.97
5943					9534	7.62	6.66	6.32	5.94
5951	7.55	6.54	6.21	5.92	9855	7.71	6.74	6.45	6.06
5961					9883	7.72		6.35	5.96
6224	7.61	6.58	6.24	6.02	9938	7.65		6.29	
6337	7.58	6.56	6.19	5.89	9943	7.63		6.29	
6579					9974	7.59		6.31	
6580					9997	7.54		6.26	
6581	7.56				10002	7.56		6.25	
6616	7.56	6.56	6.25	5.79	10064	7.55		6.21	
6690	7.58			5.89	10199	7.66	6.65	6.25	6.05
7044	7.39	6.48	6.13	5.80	10204	7.65	6.66	6.27	5.98
7046	7.37				10211	7.70	6.65	6.26	
7418	7.64		6.38		10233	7.70	6.65	6.30	5.95
7436	7.62		6.37		10242	7.65		6.28	
7702	7.29	6.40	6.14	5.82	10261	7.64		6.32	
7808	7.31		6.10		10294	7.65		6.32	
8024	7.35		6.15		10623	7.64		6.28	
8027	7.32		6.14		10699	7.60	6.62	6.28	5.99
8053	7.34		6.12		10754	7.58		6.20	
8064	7.32		6.12		10765	7.54	6.56	6.19	5.91

Table 1. (Contd.)

JD 2440000+	*J*	*H*	*K*	*L*	JD 2440000+	*J*	*H*	*K*	*L*
10868	7.51	6.55	6.19	5.85	12031	7.57		6.23	
10978	7.59		6.22		12037	7.56		6.22	
11009	7.68		6.34		12125	7.63		6.28	
11037	7.71		6.32		12126	7.66		6.30	
11095	7.63		6.24		12127	7.66		6.28	
11300	7.51		6.17		12131	7.67		6.30	
11336	7.52		6.18		12132	7.64		6.31	
11351	7.56		6.21		12153	7.69		6.33	
11355	7.54		6.20		12157	7.68		6.34	
11358	7.55		6.18		12158	7.67		6.33	
11359	7.55		6.20		12187	7.64		6.34	
11360	7.55		6.18		12190	7.67		6.34	
11361	7.54		6.19		12192	7.70		6.31	
11365	7.54		6.20		12211	7.69		6.33	
11383	7.54		6.20		12220	7.66		6.32	
11384	7.55		6.19		12348	7.58		6.24	
11385	7.54		6.22		12367	7.57		6.24	
11387	7.55		6.22		12391	7.59		6.24	
11390	7.52		6.17		12420	7.59		6.24	
11393	7.54		6.18		12455	7.58		6.25	
11420	7.54		6.18		12.483	7.64		6.28	
11421	7.55		6.21		12510	7.70		6.28	
11423	7.53		6.20		12537	7.62		6.28	
11453	7.55		6.23		12540	7.63		6.28	
11686	7.59	6.60	6.22	5.97	12740	7.51		6.18	
11687	7.60		6.24		12751	7.53		6.20	
11707	7.60		6.25		12774	7.53		6.19	
11738	7.68		6.32		12778	7.52		6.19	
11740	7.71		6.31		12800	7.50		6.21	
11741	7.67		6.30		12806	7.54		6.20	
11768	7.71		6.35		12809	7.54		6.22	
11770	7.72		6.36		12836	7.58		6.24	
11777	7.70		6.33		12840	7.57		6.25	
11779	7.71		6.33		12843	7.57		6.24	
11780	7.72		6.33		12866	7.61		6.28	
11782	7.73		6.34		12867	7.61		6.28	
11802	7.72		6.34		12869	7.60		6.28	
11834	7.68		6.31		12871	7.60		6.28	
11865	7.58		6.23		12889			6.31	
11867	7.57		6.21		12890	7.66		6.31	
12007	7.58		6.23		12925	7.69		6.33	
12012	7.56		6.23						

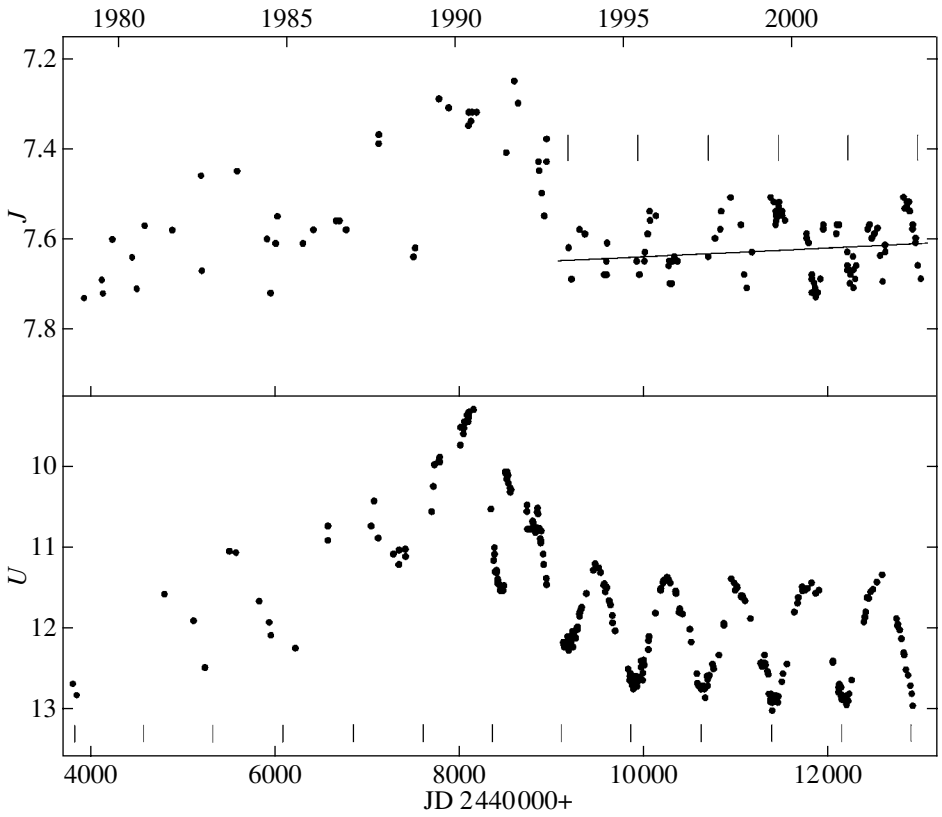

Fig. 1. U and J light curves of the symbiotic star BF Cyg. The solid line is a linear fit to the J light curve. The vertical bars mark the epochs of primary brightness minima calculated using (1).

the color indices of red giants in the solar neighborhood [14]. The mean color index $\langle J-K\rangle_0$ corresponds to the same spectral type. A comparison of $\langle J-K\rangle_0$ with the color indices of red giants in the bulge [15] indicates a spectral type for the red giant in BF Cyg of ∼M6. Recall that the spectral type derived from the intensities of the TiO bands is ∼M5 [4, 5]. The differences in the IR color indices of red giants having similar spectral types (based on their TiO bands) but belonging to different Galactic populations can be explained as an effect of metallicity differences [15]; the metallicity is higher for red giants in the bulge. If present, enhanced metal abundances for red giants in symbiotic stars probably reflect these binaries' evolutionary history, and are not related to their population types.

Figure 2 presents (J, K) and $(J, J-K)$ diagrams plotted using the same horizontal scale. The solid lines are linear fits to these relations. These diagrams were plotted using only IR brightness estimates obtained since 1993. We can see from Fig. 2 that the mean $J-K$ color index increases with decreasing J brightness. The increase in the color index is $\sim 0.05^m$, corresponding to changes in the red giant's spectral type within one subtype. However, the scatter of the data points around the approximating line is not smaller than this mean increase. In addition, this scatter is not smaller than the corresponding scatter in the (J, K) diagram, although the brightness variations in these spectral bands are significantly correlated. The correlation coefficient for the linear relation between the red giant's J and K brightness is ∼0.87. At the same time, the correlation coefficient for the linear fit relating the J brightness and $J-K$ color index is ∼0.45, while that for the relation between the K brightness and $J-K$ color index is close to zero, with the $(K, J-K)$ diagram displaying a cloud of data points.

3. PERIODIC BRIGHTNESS VARIATIONS OF THE RED GIANT

Consider the J and K light curves of BF Cyg beginning in 1993 (JD = 2 449 114). By that time, the hot component had returned to its quiescent state, and the red giant's light dominated in the IR. We can see from Fig. 1 that the J light curve exhibits minima coinciding with the U-brightness minima. One exception is the minimum of 1999 (JD = 24 411 384), when maxima were displayed by the J and K light curves, as opposed to the minimum observed in U.

It is possible that the expected brightness minimum of the cool component failed to occur due to the

considerable irregularity of the red giant's variability, as is characteristic of stars with such late spectral types. Several cases of aperiodic IR brightness variations are known for symbiotic stars, towards both higher and lower brightnesses compared to the expected values (cf. [16] and references therein). For this reason, we did not use the data corresponding to the "missing" minimum of 1999 in our subsequent periodicity analysis, although, if included, these data would only change the depth of the minimum in the folded light curve slightly, without affecting the basic conclusion that there is a periodic component in the brightness variations of the BF Cyg red giant.

We searched for periodic components in the brightness variations using code written by Yu.K. Kolpakov (http://infra.sai.msu.ru/prog/kolpakov). Possible periodicities were detected by approximating the data time series with a combined function (which we will call an approximation curve), which includes a polynomial part (a third-order polynomial) that reproduces the cubic trend of the signal's permanent component and a Fourier series up to the third harmonic. The coefficients of the approximating polynomial are determined from a least-squares fit.

The periodogram analysis revealed the presence of JK brightness variations with periods of $P_1 = 767 \pm 15$ days ($\approx P_{\rm orb}$) and $P_2 = 381 \pm 5$ days ($\approx 1/2 P_{\rm orb}$). The deviations of P_1 from $P_{orb} = 757.2 \pm 2.6$ days and from $P(U) \approx 758.0 \pm 0.4$ days are within the errors in the period P_1. The comparatively large uncertainty of our P_1 estimate is due to the irregularity of the red giant's brightness variability. In particular, we believe this to be the origin of the missing expected IR brightness minimum of 1999. Note that, if we include the 1999 data points in the periodogram analysis, the estimates of the periods P_1 and P_2 will change by less than 1%, and these changes are within the uncertainties in the periods.

Figure 3 shows the U and J light curves of BF Cyg folded with the 758-day period, together with the corresponding approximation curves. When folded with the 762-day period ($2P_2$), the shape of the J curve and the parameters of the approximation curve remain virtually unchanged. The zero epoch of the shallower J brightness minimum (phase $\varphi = 0$ in Fig. 3) coincided with the zero epoch of the U brightness minimum (JD 2449135). We will call this minimum of the J light curve the primary minimum. At this time, the red giant is near its lower conjunction, so that it covers the hot component and part of the circumstellar envelope. According to the red giant's radial-velocity curve, the times of lower conjunction are given by the formula

$$T_{\rm conj} = \text{JD } 2449124 + 757.2^* E \text{ days [6]}. \quad (2)$$

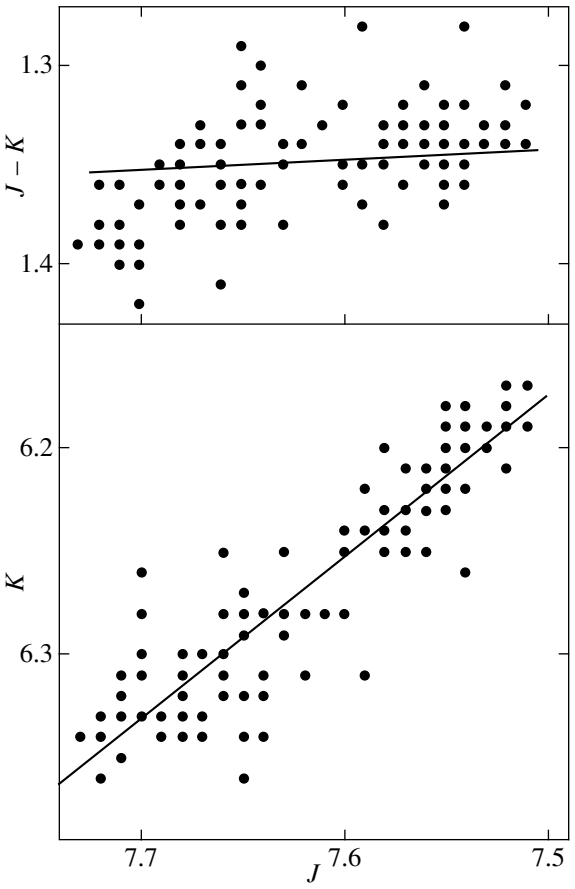

Fig. 2. (J, K) and $(J, J-K)$ diagrams. The solid lines are linear fits to the relations.

Since we are considering a time interval when the red giant's light dominated in the IR, the primary minimum, whose depth is $\sim 0.13^m$, cannot be due to an eclipse of part of the hot radiation source (the hot component + the circumstellar envelope).

The secondary minimum of the J brightness (the red giant is behind the hot component, upper conjunction) is observed at phase $\varphi \approx 0.48$, and is $\Delta_{min} \approx 0.02^m$ deeper than the primary minimum. For the ratio of the radii of the hot and the cool components, $R_{hot}/R_{giant} \approx 0.0035$ [10], the secondary minimum, with a depth of $\sim 0.15^m$, cannot be due to an eclipse of part of the red giant by the hot subdwarf. Thus, the IR brightness variations of the cool component of BF Cyg contain a periodic component whose period is half the orbital period, which is not associated with partial eclipses of the hot radiation sources or of the red giant.

This brightness variability of the cool component is likely due to the ellipsoidal shape of the red giant (or, in the case of cataclysmic variables, of the main-sequence star) that it acquires when it fills its Roche lobe (we, accordingly, will call this ellipsoidal

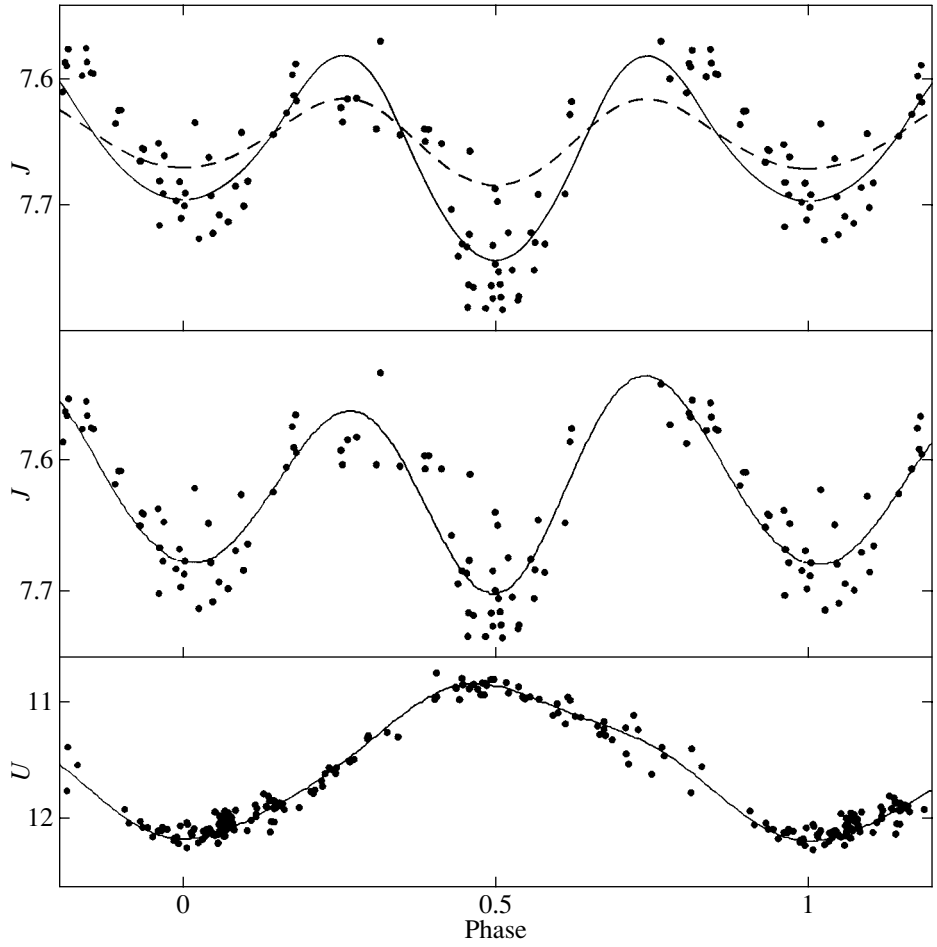

Fig. 3. U and J light curves of BF Cyg folded using (1). The solid curve in the middle panel is an approximation fit to the folded curve. The observational data in the upper panel were corrected for the light from the hot source. The solid and dashed curves in the upper panel are light curves calculated in models with $q = 3$, $i = 80°$, $\mu = 1$ and $q = 3$, $i = 80°$, $\mu = 0.9$, respectively. See text for more detail.

brightness variability). Note that various depths of the minima are characteristic of the ellipsoidal brightness variability of red giants [12]. There are no alternative explanations for this kind of brightness variability occurring in a cool component in a binary system, and we will, accordingly, analyze this variability in an ellipsoidal-variability model.

The J brightness maxima are observed at phases $\varphi \approx 0.25$ and 0.73, with the second maximum being $\sim 0.02^m$ brighter. These brightness should be equal in a pure ellipsoidal-variability model for the red giant. When comparing the model light curve for the red giant and the approximation curve or observed curve in our subsequent analysis, we will use the mean brightness of the cool component in its two brightness maxima. According to the approximation curve, the mean brightness at the maxima is $A \approx 0.15^m$ higher than the mean brightness at the secondary minimum. The K variability amplitude is $A \approx 0.13^m$. An ellipsoidal IR brightness-variability amplitude that high indicates that the red giant should be close to filling its Roche lobe.

The difference between the giant's mean brightness at phases $\varphi = 0.2$–0.3 and $\varphi = 0.7$–0.8 (brightness maximum) and its mean brightness at $\varphi = 0.45$–0.55 (secondary minimum) is $A' \approx 0.13^m$. The same difference results from a similar averaging using the approximation curve calculated for the set of phases corresponding to the dates of the actual observations. The rms deviation of the individual differences between the approximation curve and the observed curve is $\sigma(O-C) \approx 0.04^m$. Our analysis of $O-C$ shows the deviations to be irregular (random), though it is possible that this conclusion will change when the number of brightness estimates has increased considerably.

4. MODEL COMPUTATIONS

We calculated the light curve for a red giant distorted by tidal perturbations from the hot component

using a classical ellipsoidal model [17], which is based on the following assumptions. The two components are described by the gravitational potential of two point masses. The red giant's axial rotation is synchronized with the orbital motion. (See [18] and references therein on the validity of this last condition for BF Cyg-type symbiotic binaries.) The orbit is circular, as follows from the analysis of [6].

We assumed that the red giant's effective temperature was $T_{eff} = 3000$ K (corresponding to a spectral type of M5 [14]) and that each element of its surface emitted as a blackbody source whose temperature was determined by a gravitational darkening law. As was demonstrated in [12], the J band is the best suited of the JHK bands if we wish to use a blackbody source to describe the real spectral energy distribution of the red giant. The exponent in the gravitational darkening law was taken to be $\beta = 0.08$ (the Lucy law for stars with convective envelopes). The limb-darkening coefficients were taken from [19].

The model input parameters included μ, describing the degree of Roche-lobe filling (in our case, μ is the ratio of the polar radii of the star and Roche lobe; if the Roche lobe is filled, $\mu = 1$), the component-mass ratio, $q = M_{giant}/M_{hot}$, and the orbital inclination, i. The parameter q was varied in the range $q = 2$–6 (cf. [6] and references therein).

The U variability amplitude, $\sim 1.4^m$ (Fig. 1), indicates that the red giant eclipses not only part of the hot component's circumstellar envelope, but the hot component itself (in the case of a spherically symmetric circumstellar envelope). Otherwise, the red giant would have covered less than half of the gaseous envelope, and the U brightness-variability amplitude would have been no larger than 0.7^m. For this reason, we varied i in the range $i = 90°$–$70°$. The best-fit model was obtained when the sum of the squared deviations between the model and observed light curves was minimum.

Table 2 presents the magnitude differences between the secondary and primary minima (Δ_{min}) together with the J variability amplitude (A) for the model in which the red giant fills its Roche lobe ($\mu = 1$). These parameters were estimated from the extrema of the model curve. Recall that the observed values of these parameters, corresponding to the extrema of the approximation curve, are $\Delta_{min} \approx 0.02^m$ and $A \approx 0.15^m$. We can see from Table 2 that the model calculations do not admit this combination of Δ_{min} and A. The calculated Δ_{min} is $\sim 0.02^m$ higher than the observed value for models with the required value for A. If we select a model that correctly reproduces Δ_{min} (with decreased q and β), A will no longer retain its require value, since Δ_{min} and A vary simultaneously.

Table 2. Dependence of the model light-curve parameters Δ_{min}/A (magnitude difference between the primary and secondary minima/the amplitude of the secondary minimum) on the input model parameters q and i ($q = M_{giant}/M_{hot}$, i is the orbital inclination) when the cool component fills its Roche lobe

i	q		
	4	3.3	2.5
	Δ_{min}/A		
90°	0.045/0.141	0.047/0.151	0.051/0.167
80°	0.042/0.136	0.044/0.146	0.048/0.162
70°	0.035/0.125	0.037/0.134	0.040/0.148

We can see in Table 2 that Δ_{min} and A depend fairly weakly on the input parameters i and q (at the level of 0.01^m). In addition, some combinations of i and q lead to virtually the same values of Δ_{min} and A (see, for example, the models along the main diagonal of Table 2). The minimum sum of squared deviations between the model and observed light curves is formally achieved for $(i, q) = (80, 3.3)$. This folded model curve is shown in Fig. 3.

At the same time, the relation between the amplitude A and the parameter μ is strong enough to enable us to draw firm conclusions about the degree of Roche-lobe filling by the red giant. In fact, the calculated amplitude for $(i, q) = (90, 3.3)$ and $\mu = 0.9$ is $A \approx 0.07^m$, which is half the observed amplitude (Fig. 3). Thus, we conclude that the cool component of BF Cyg essentially fills its Roche lobe—provided, of course, that the brightness variations with a period of half the orbital period do, indeed, represent ellipsoidal variability. No other explanation has been proposed to explain these variations.

Due to the eclipse, the brightness of the hot source (the hot component + the ionized envelope) varies considerably in the course of the orbital motion of the binary BF Cyg (Figs. 1 and 3). It is lowest at the primary minimum and highest at the secondary minimum of the red giant's IR brightness. Accordingly, the contribution of the hot source to the total IR brightness of BF Cyg (due to the hot source + the red giant) will be lowest at the primary minimum and highest at the secondary minimum. Thus, taking the hot source into account will increase the brightness difference between these minima.

If we assume that the hot component's quiescent temperature is $\sim 6 \times 10^4$ K, the electron temperature of the gaseous envelope is $T_e \sim 10^4$ K, and the color excess is $E(B-V) \approx 0.4$ [10], then, with the mean

brightness of the hot source ($\langle U\rangle \approx 12.3^m$), its contribution to the J radiation will be $\sim$3%. For the U brightness variability amplitude of 1.4^m (Fig. 2), the contribution of the hot source to the J radiation at the primary and secondary minima of the J brightness will be $\sim$1.3% and $\sim$4.7%, respectively. Assuming harmonic brightness variations of the hot source with the 758-day period, we subtracted its contribution to the J radiation, thereby deriving the "corrected" brightness of the red giant.

Note that the contribution of the hot component to the J radiation of the hot source is less than 10%; i.e., the main contribution of the hot source in the IR is made by the ionized envelope. In addition, the contribution of the hot source to the K band will differ from its contribution to the J band by less than 0.5%. Hence, taking this radiation into account will not change the $J-K$ color index, leaving the spectral classification of the red giant unaltered (see Section 2).

The red giant's corrected light curve folded with the 758-day period is plotted in Fig. 3 along with the folded model curve calculated for $\mu = 1$, $q = 3.3$, and $i = 80°$ (Table 2). We normalized the calculated curve to the observed curve using the condition that $\langle \mathrm{O{-}C}\rangle = 0$. The rms deviation of the $O{-}C$ estimates is $\sigma(\mathrm{O{-}C}) \approx 0.04^m$.

The difference between the giant's mean brightness at phases $\varphi = 0.2{-}0.3$ and $\varphi = 0.7{-}0.8$ (brightness maximum) and its mean brightness at $\varphi = 0.45{-}0.55$ (secondary minimum) is now $A' \approx 0.134^m$ ($A' \approx 0.122^m$ when the hot source is not taken into account). The difference between the giant's mean brightness at phases $\varphi = -0.05{-}0.05$ (primary minimum) and its mean brightness at phases $\varphi = 0.45{-}0.55$ (secondary minimum) is $\Delta'_{min} \approx 0.045^m$ ($\Delta'_{min} \approx 0.015^m$ when the hot source is not taken into account). Similar averaging using the model curve ($\mu = 1$, $q = 3.3$, $i = 80°$) calculated for the set of phases corresponding to the dates of the actual observations (Fig. 4) leads to $A' \approx 0.137^m$ and $\Delta'_{min} \approx 0.042^m$.

The model reproduces the features of the periodic component of the red giant's light curve rather well when the contribution of the hot source (small as it is) is taken into account. Nevertheless, we would like to stress again that it is not possible to unambiguously choose a best model from the list in Table 2. This is hindered by the considerable irregularity of the variability of the red giant's IR brightness, which distorts the periodic ellipsoidal component and introduces appreciable errors in parameters such as A and Δ_{min}. Additional ambiguity in selecting the best model is due to the relatively weak dependence of the model light-curve parameters, A/Δ_{min}, on the input model parameters, such as q and i (Table 2).

However, we can be confident that ellipsoidal brightness variability is present, and has a large amplitude and minima with different depths. This large amplitude and the fairly strong dependence of the model light-curve amplitude on the degree of Roche-lobe filling by the cool component (μ) enable us to conclude that the cool component of BF Cyg essentially fills its Roche lobe, and is thus a luminosity-class-II red giant.

5. CONCLUSION

Our long-term monitoring observations of the classical symbiotic star BF Cyg in the IR demonstrate that the red giant's brightness variations contain a periodic component, with a period of half the orbital period and a J amplitude of $\sim 0.15^m$.

These brightness variations are due to the ellipsoidal shape of the cool component of BF Cyg, which, according to our model calculations, should fill its Roche lobe. In this case, the accretion of matter from the red giant onto the hot component occurs via an accretion disk, which provides an accretion rate sufficient, from an energetic point of view, to produce the observed novalike outbursts of BF Cyg.

The effect we have detected is consistent with our current understanding of BF Cyg. Earlier observations showed that the system's cool component filled its Roche lobe during an eclipse of the hot component in 1999 [7]. The question of whether BF Cyg is a normal red giant or a bright giant of luminosity class II could be answered directly if the distance to the system were known. However, it is not possible to determine the distance to the star using direct methods. Since the distance to BF Cyg exceeds 2 kpc and it is located fairly high above the Galactic plane ($b \approx 7°$), it is likewise not possible to estimate its distance from the observed interstellar reddening (for BF Cyg, this yields only a lower limit for the distance of $\sim$500 pc [10], which is too nearby for a star of luminosity class III, and even more so for luminosity class II). The spectral classification [20] also does not provide an exact answer to this question.

Ellipsoidal brightness variations have now been revealed for such classical symbiotic stars as CI Cyg [13] and YY Her [21]. However, they are definitely absent for noneruptive symbiotic stars, such as V443 Her [22] and RW Hya [23], although these stars are a kind of twin of the classical symbiotic stars in quiescence. Their orbital periods are also similar.

It is not unambiguously known why only some of these apparently similar symbiotic stars display outbursts and others do not. In our opinion, the most

probable origin is differences in the degree of Roche-lobe filling by the cool components. When the lobe is sufficiently filled, the relatively low-efficiency accretion of the red giant's stellar wind, which is largely compensated by the stellar wind from the hot component, is replaced by the more efficient disk accretion [8]. However, the accumulated direct evidence that the cool components of classical symbiotic stars fill their Roche lobes is still not conclusive. Many years of systematic observations in the IR are needed in order to determine with confidence whether a red giant's brightness displays ellipsoidal variations.

ACKNOWLEDGMENTS

This study was supported by the Russian Foundation for Basic Research (project nos. 02-02-16235, 03-02-06765, and 03-02-16662).

REFERENCES

1. A. A. Boyarchuk and P. E. Gershberg, *Eruptive Stars* (Nauka, Moscow, 1970), p. 113 [in Russian].
2. S. J. Kenyon, *The Symbiotic Stars* (Cambridge Univ., Cambridge, 1986), p. 283.
3. A. Cassatella, T. Fernandez-Castro, R. Gonzales-Riestra, and J. J. Fuensalida, Astron. Astrophys. **258**, 368 (1992).
4. A. P. Ipatov and B. F. Yudin, Astron. Astrophys., Suppl. Ser. **65**, 51 (1986).
5. Z. X. Zhu, M. Friedjung, G. Zhao, *et al.*, Astron. Astrophys., Suppl. Ser. **140**, 69 (1999).
6. F. C. Fekel, K. H. Hinkle, R. R. Joyce, *et al.*, Astron. J. **121**, 2219 (2001).
7. A. Skopal, A. Vittone, L. Errico, *et al.*, Mon. Not. R. Astron. Soc. **292**, 703 (1997).
8. A. A. Tatarnikova, M. Rechkuba, L. M. Buson, *et al.*, Astron. Zh. **77**, 220 (2000) [Astron. Rep. **44**, 190 (2000)].
9. A. Pucinskas, Bull. Vilnius Astron. Observ. No. 27 (24).
10. J. Mikolajewska, S. J. Kenyon, and M. Mikolajewski, Astron. J. **98**, 1427 (1989).
11. B. Yudin and U. Munari, Astron. Astrophys. **270**, 165 (1993).
12. T. Shahbaz, M. Somers, B. Yudin, and T. Naylor, Mon. Not. R. Astron. Soc. **288**, 1027 (1997).
13. J. Mikolajewska, Astron. Soc. Pacif. Conf. Ser. **246**, 167 (2001).
14. T. A. Lee, Astrophys. J. **162**, 217 (1970).
15. D. M. Terndrup, J. A. Frogel, and A. E. Whitford, Astrophys. J. **357**, 453 (1990).
16. U. S. Kamath and N. M. Ashok, Astron. Astrophys., Suppl. Ser. **135**, 199 (1999).
17. S. J. Tjemkes, J. van Paradijs, and E. J. Zuiderwijk, Astron. Astrophys. **154**, 77 (1986).
18. W. Schmutz, H. Schild, U. Murset, and H. M. Schmid, Astron. Astrophys. **288**, 819 (1994).
19. A. Claret, Astron. Astrophys. **363**, 1081 (2000).
20. S. J. Kenyon and T. Fernandez-Castro, Astron. J. **93**, 938 (1987).
21. J. Mikolajewska, E. A. Kolotilov, S. Yu. Shugarov, and B. F. Yudin, Astron. Astrophys. **392**, 197 (2002).
22. E. A. Kolotilov, U. Munari, A. A. Popova, *et al.*, Pis'ma Astron. Zh. **24**, 39 (1998) [Astron. Lett. **24**, 34 (1998)].
23. J. Mikolajewska, E. A. Kolotilov, V. I. Shenavrin, and B. F. Yudin, Astron. Soc. Pacif. Conf. Ser. **261**, 645 (2002).

Translated by N. Samus'

Astronomy Reports, Vol. 49, No. 3, 2005, pp. 242–249. Translated from Astronomicheskiĭ Zhurnal, Vol. 82, No. 3, 2005, pp. 273–280.

Radio Emission from Two Anomalous X-ray Pulsars

V. M. Malofeev[1], O. I. Malov[1], D. A. Teplykh[1,2], S. A. Tyul'bashev[1], and G. E. Tyul'basheva[3]

[1] *Pushchino Radio Astronomy Observatory, Astro Space Center, Lebedev Physical Institute, Russian Academy of Sciences, Pushchino, Moscow oblast, 142290 Russia*

[2] *Pushchino State University, Pushchino, Moscow oblast, Russia*

[3] *Institute of Mathematical Problems of Biology, Institutskaya ul. 4, Pushchino, Moscow oblast, 142290 Russia*

Received May 7, 2004; in final form, September 20, 2004

Abstract—Observations of the anomalous X-ray pulsar (AXP) 1E 2259+586 and the AXP candidate 1RXS J1308.6+212708 at 111, 87, and 61 MHz are reported. The observations were carried out on two high-sensitivity radio telescopes of the Pushchino Radio Astronomy Observatory. Mean pulse profiles are presented, and the dispersion measures, distances, spectral indices, and integrated radio luminosities of both objects are estimated. Comparison with X-ray data shows large differences in the mean pulse widths and luminosities. The detection of radio emission from these two AXPs, together with other data, suggests the need to revise the radio-emission mechanisms in the magnetar model or the magnetar model itself.

1. INTRODUCTION

Recent space-based gamma-ray and X-ray observations have led to the discovery of two special groups of pulsars: anomalous X-ray pulsars (AXPs) [1] and soft gamma-ray repeaters (SGRs) [2]. It is now generally accepted that these neutron stars have different parameters than are typical of the larger group of "normal" radio pulsars and ordinary X-ray pulsars. Five AXPs and four AXP candidates have been identified, while the list of SGRs includes four objects and one candidate. A list of 13 pulsars in these two groups is presented in [3], together with the main differences of these objects from other known pulsars; another AXP candidate was detected quite recently [4]. Recall that these objects differ from normal radio pulsars in their long periods, which lie in the narrow range of 5–12 s, and large period derivatives, 10^{-11}–10^{-13} s/s. Despite their long rotational periods, they are thought to be young objects with characteristic ages of up to several hundred thousand years. All these objects are located close to the plane of the Galaxy, and nearly half are inside supernova remnants. AXPs and SGRs also differ from ordinary X-ray pulsars in the continuous decreasing of their periods and their more stable X-ray fluxes and lower X-ray luminosities, 10^{34}–10^{36} erg/s. Furthermore, AXPs and SGRs have softer spectra, which can frequently be described by a combination of a blackbody spectrum and a power-law segment with a steep spectral index (2.5–4.0). The most important difference between these objects and other X-ray pulsars is the absence of a detectable companion; i.e., they are single neutron stars. All these features are presented in the reviews and papers [1–8].

One of the most intriguing problems connected with these objects is the source of their energies, which sometimes imply luminosities that are two to three orders of magnitude higher than can be provided by the rotational kinetic-energy losses associated with rotational braking in "normal" pulsars. All the models proposed until recently to explain this new energy source encounter serious difficulties. These include the historically first model, which involves accretion of the surrounding plasma onto a neutron star (see, e.g., review [9]), the very interesting model of [10], with the gravitational collapse of a neutron star into a quark star, and the currently most popular magnetar model [5], which proposes that these objects are single neutron stars with superstrong magnetic fields, $\sim 10^{14}$–10^{15} G. These difficulties are considered in detail by Malov *et al.* [3]. One of the key arguments in favor of the magnetar model was the absence of radio emission from AXPs and SGRs: this could be naturally explained as a consequence of the impossibility of forming the electron–positron cascades that are responsible for radio emission in many models in the presence of such high fields [11, 12].

This was the situation until recently, when pulsed radio emission was detected from the SGR 1900+14 [13] and the AXP 1E 2259+586 [14] in 1999–2001. This led to searches for new mechanisms for the generation of radio emission in the

framework of the magnetar model [15], as well as completely new models, such as the action of drift waves at the periphery of the magnetosphere. This latter model can explain many features of AXPs and SGRs if these objects are neutron stars with periods of about 0.1 s, period derivatives of about 10^{-13} s/s, and "normal" surface magnetic fields of $\sim 10^{12}$ G [3].

The importance of searches for and studies of the radio emission of AXPs and SGRs is obvious. In this paper, we present new data on the radio emission of the first AXP, 1E 2259+586, and present parameters of the radio emission of the AXP candidate J1308.6+212708 for the first time.

The X-ray object 1E 2259+586 (G109.1−1.0) was detected in the direction toward the supernova remnant CTB 109 in 1980 by Gregory and Fahlman [16], who also detected pulsed emission (1E 2259+586), first with the period $P = 3.489$ s and then with $P = 6.9786$ s and $\dot{P} = 7 \times 10^{-14}$ s/s [17]. Subsequently, some groups measured and updated the coordinates, period, and period derivative (see, e.g., [17, 18]). The first paper concerning residual deviations of the pulse times of arrival reported the presence of an orbital period of 2300 s [17], which was not confirmed by later studies.

The second object, 1RXS J1308+21, was discovered in 2001 [19]. It has a period of $P = 5.16$ s and an uncertain period derivative, $\dot{P} = (0.7–2.0) \times 10^{-11}$ s/s. The rotational period for this pulsar was recently redetermined; as in the earlier case of the AXP 1E 2259+586, the period was doubled, i.e., $P = 10.32$ s [20]. Since the properties of this object are similar to those of AXPs, it is considered a candidate member of this group.

2. OBSERVATIONS

The observations of the AXP 1E 2259+586 began on March 7, 1999, and 19 measurements were obtained in the following two years. Regular 3-day to 15-day observations every one–two months began in February 2001. The second object, 1RXS J1308+21, has been observed in the same mode since December 21, 2001. We consider here data obtained for both pulsars up until April 2003. Most of the observations were obtained on the high-sensitivity Large Phased Array (LPA) of the Lebedev Physical Institute of the Russian Academy of Sciences at a frequency of 111 MHz. We also occasionally carried out simultaneous observations at 87 or 61 MHz on the East–West arm of the DKR-1000. Both radio telescopes are meridian-transit instruments; the durations of the observations on the LPA were 6.2 and 3.3 min for 1E 2259+586 and 1RXS J1308+21, respectively, and a factor of three longer for each pulsar on the DKR-1000.

A filter-bank spectrum analyzer with a bandwidth of 20 kHz and 64 channels at 111 MHz and 32 channels at 87 and 61 MHz was used. As a rule, the data-sampling interval was 25.6 or 51.0976 ms and the receiver time constant was 30 or 100 ms. These parameters were used in a mode designed for integrating a signal with a known period. In addition, we used a method to independently search for the pulsed radio emission [21], using 63 20-kHz channels and a sampling interval of 21.94 ms. To increase the certainty with which pulses were recorded in the integration mode, we carried out numerous observations of 1RXS J1308+21 and some observations of 1E 2259+586, including all the measurements at 87 and 61 MHz, applying double the period (i.e., $P = 10.314$ for 1RXS J1308+21, or $2P = 20.628$ s) using a technique that has been tested with observations of faint and millisecond pulsars [22], as well as the Geminga pulsar [23]. Some observations were calibrated using reference radio sources with known flux densities. The observational technique and processing of the data are described in detail in [22].

3. RESULTS

We detected weak periodic pulsed radio emission from the AXP 1E 2259+586 at the end of 2000, with the shape of the radio pulses differing strongly from that for the X-ray pulses. The mean flux density was 70 mJy. We estimate the dispersion measure to be 80 ± 5 pc/cm^3, which yields the first estimate of the distance to the pulsar (3.6 kpc). These results have been reported at several conferences, together with values for the period and period derivative (see, e.g., [14, 24]).

The observations of the AXP candidate 1RXS J1308+21 began in 2002, right after the publication of the study of Hambaryan *et al.* [19], who reported an accurate position, the period, and an estimate of the period derivative. After only one month of observations, we detected periodic pulsed radio emission from this object at 111 MHz. As in the case of the AXP 1E 2259+586, the radio pulse was considerably narrower than the X-ray pulse. Preliminary results on the period, period derivative, shape of the mean profile, flux, dispersion measure, and distance to the pulsar have been presented early in 2002 at a number of conferences [25, 26].

We report here new data, including our data for April 2003. In total, we had 321 days at 111 MHz, 33 days at 87 MHz, and 5 days at 61 MHz for the AXP 1E 2259+586 over the entire observational interval. About one-third of the observations were corrupted by strong interference, and the pulsar signal did not exceed 4σ on more than one-third of the days, however, 89 days at 111 MHz and 7 days at

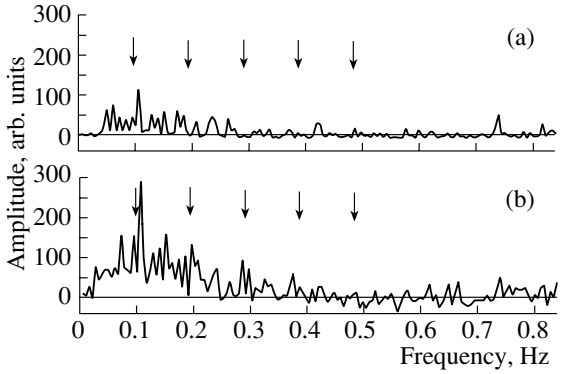

Fig. 1. Examples of Fourier-amplitude spectra of the AXP candidate 1RXS J1308+21 at 111.2 MHz: (a) spectrum for May 1, 2003, (b) total spectrum for five days of observations. The arrows mark the phases of the first five Fourier harmonics (for a period of 10.31 s).

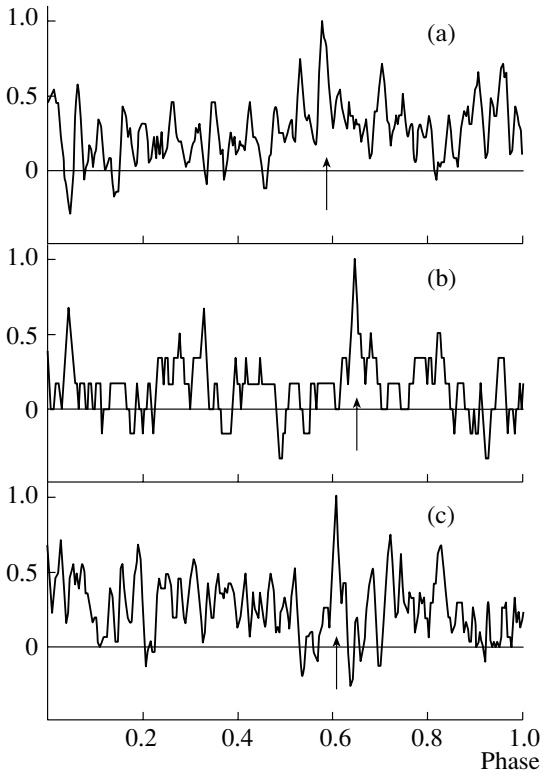

Fig. 2. Examples of integrated profiles of the AXP 1E 2259+586 at 111.2 MHz (in arbitrary units) obtained by summing (a) 53 periods on March 29, 2002, (b) 14 periods on September 6, 2002, and (c) 53 periods on January 11, 2003. The arrows mark the phases of pulse arrival.

87 MHz remained for further analysis. Unfortunately, the pulsar signal was not detected at 61 MHz, probably due to interference. We obtained 130, 20, and 8 records at 111, 87, and 61 MHz, respectively, for

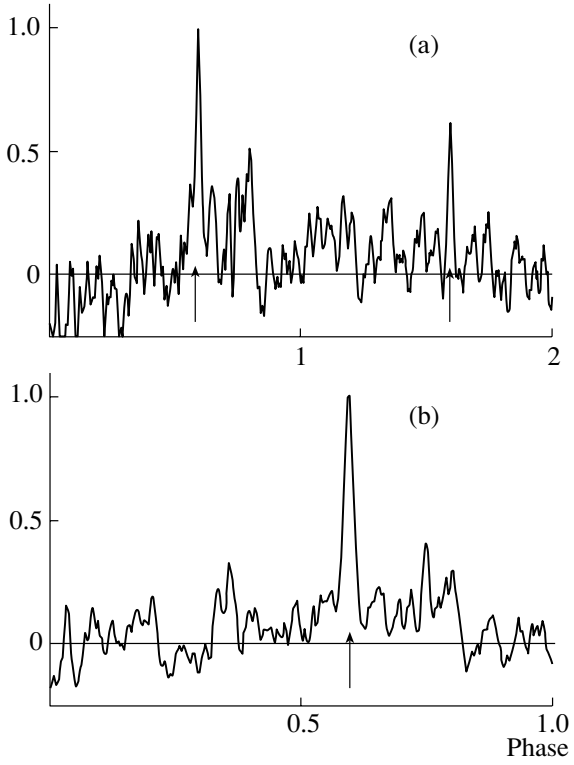

Fig. 3. (a) Integrated profile of the AXP 1E 2259+586 at 111.2 MHz (in arbitrary units) obtained by summing 12 days of observations and 312 doubled pulsar rotation periods, $P_H = 2P$; (b) convolution with the rotational period, i.e., the sum of 624 periods. The arrows mark the phases of pulse arrival.

1RXS J1308+21, with 76, 10, and 5 days being useful for analysis.

(a) Search Method

The first version of this method was tested in a search for pulsars in a sample of faint scintillating sources [21]. The method was updated at the end of 2001 as follows. We implemented normalization in all channels, so that the signal dispersion in each channel was unity (i.e., the gains were made the same in all channels), and took into account the probable signal dispersion measure via a cyclic shift in the corresponding channels. In the searches, we considered dispersion measures not exceeding 100 pc/cm^3, adding the signals in all channels for each dispersion measure. We plotted the power spectra for all possible dispersion measures, then summed harmonics and searched for those for which the signal-to-noise ratio exceeded a given level. Tests of this method using observations of known pulsars demonstrate that pulsars with fluxes $\geq$70 mJy can be confidently detected. Using the improved method, we observed both the target objects as part of a search for periodic pulsed

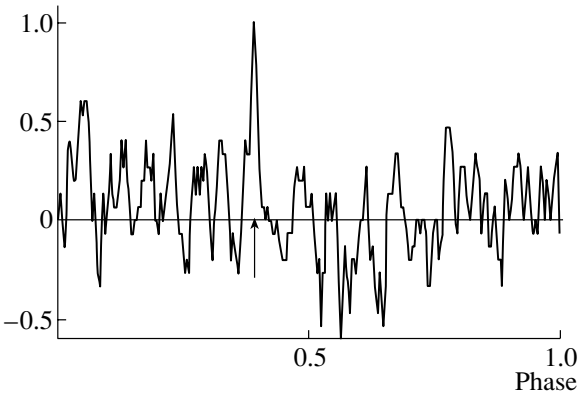

Fig. 4. Example of an integrated profile of the AXP 1E 2259+586 at 87.5 MHz (in arbitrary units), obtained on October 5, 2002 by integrating over 80 periods. The arrow shows the phase of the pulse arrival.

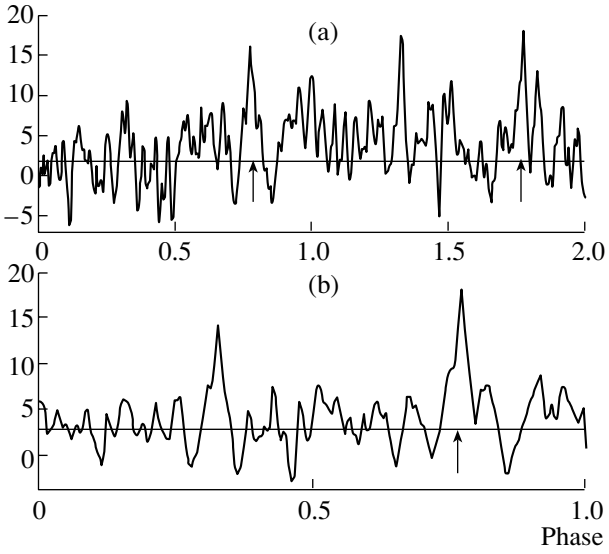

Fig. 5. (a) Integrated profile of the AXP candidate 1RXS J1308+21 at 111.2 MHz (in arbitrary units), obtained by summing four days of observations and 25 double pulsar rotational periods $P_H = 20.64$ s. (b) Convolution with the rotational period $P = 10.32$ s, i.e., the sum of 50 periods. The arrows show the pulse-arrival phases.

radio signals from more than 30 candidate objects at the centers of supernova remnants and toward AXPs, SGRs, steep-spectrum sources, etc. The search sensitivity was estimated using observations of strong and faint known pulsars.

We were able to obtain some good spectra for both AXPs, two of which were presented in [26]. We show here two more examples of Fourier-amplitude spectra for 1RXS J1308+21 (Fig. 1). While we see primarily the broad, strong first harmonic in 1E 2259+586 [26], several harmonics are observed in 1RXS J1308+21. In particular, after adding five spectra (Fig. 1b), the amplitude of the first harmonic in the total spectrum increases compared to the amplitude in Fig. 1a, and possible weak second and third harmonics begin to appear (Fig. 1b).

(b) Mean Profile

1E 2259+586. Since the integrations for individual days were carried out over only 53 pulses, the signal-to-noise ratio of the mean pulse rarely reached five (examples for three days of observations are presented in Fig. 2). Accordingly, we improved the signal-to-noise ratio by summing the data for a number of different days. Since we did not have precise timing for this pulsar, we summed days when the observations were carried out using the double period, and the pulses were aligned using visible pulses. In this case, we should observe two pulses separated by precisely one pulsar period in the summed profile, as is shown in Fig. 3a. Adding these two pulses using the pulsar period (Fig. 3b) yielded a very narrow profile with a mean duration of 120 ± 20 ms, or 1.7% of the period. This is one of the narrowest pulses observed for radio pulsars. Furthermore, in contrast to the X-ray profile, we observe no interpulse with an amplitude $\geq 20\%$ of the main pulse in the radio profile. We were also able to detect pulsed periodic emission from this pulsar at 87.5 MHz (Fig. 4). The low signal-to-noise ratio (~ 5) is due to the small number of accumulated periods (80).

1RXS J1308+21. We also observe a narrow pulse at 111 MHz in this pulsar, which has a duration of 140 ± 20 ms, or 1.35% of the period ($P = 10.32$ s). Figure 5 shows the mean pulse obtained by integrating 25 periods for four days using the same technique as for 1E 2259+586. We also detected the pulsar at 88 MHz (Fig. 6a) and 61.8 MHz (Fig. 6b). While the 88 MHz pulse is visible after integrating only 14 periods, we had to sum data for three days of observations and 100 periods at the lower frequency. In addition to a narrow pulse, this pulsar displays an interpulse at a longitude of $\sim 180°$, which is clearly visible in Figs. 5 and 6. This is probably why the second harmonic is clearly visible in the power spectrum in both the X-ray and radio [19, 26].

(c) Dispersion Measure

Determining dispersion measures is extremely important, since it makes it possible to obtain independent estimates of the distances to the pulsars.

1E 2259+586. We estimated the dispersion measure using the best data in the 111.24–110.60-MHz frequency band, which was covered by 64 receiver channels: $\mathrm{DM} = 79 \pm 4$ pc/cm^3. The signal-to-noise

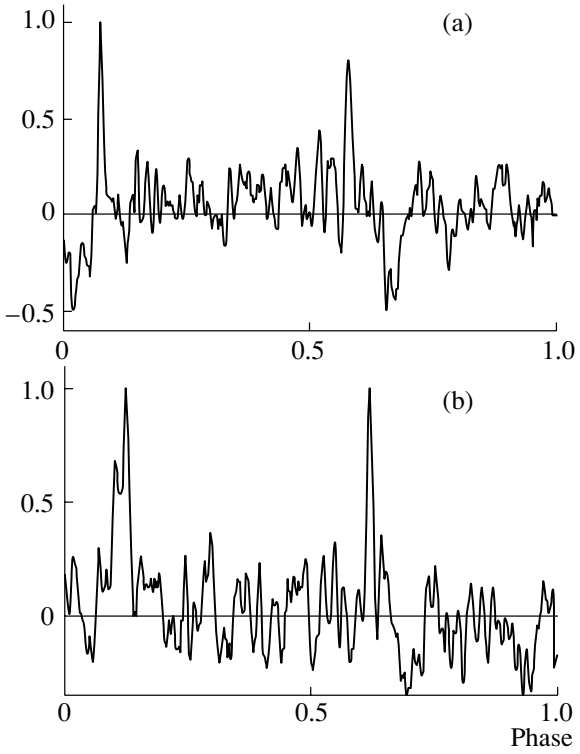

Fig. 6. Integrated profile of the AXP candidate 1RXS J1308+21 (in arbitrary units) at (a) 87.7 MHz, summed over two days and 14 periods and (b) 61.8 MHz, summed over three days and 100 periods.

ratio as a function of the dispersion measure for five days of observations is shown in Fig. 7a, and the dependence of the DM on the pulse duration at half-maximum is presented in Fig. 7b. We can see from Fig. 7 that the pulse has the highest signal-to-noise ratio for DM = 70–90 pc/cm^3.

Similar relationships are observed at 87 MHz. Unfortunately, we have not been able to obtain reliable simultaneous recordings of the pulses at 111 and 87 MHz to improve our estimate of the dispersion measure.

1RXS J1308+21. We performed a similar analysis to find the dispersion measure of this pulsar at all three frequencies: 111, 87, and 61 MHz. The most probable value of the dispersion measure is 5.7 ± 0.5 pc/cm^3; Figs. 7c, 7d show that this DM yields the pulse with the highest signal-to-noise ratio and the shortest duration, though the maximum and minimum are not as sharp as for 1E 2259+586.

(d) Flux Density

We measured the fluxes of both pulsars at 111 MHz via calibration and referencing to radio sources with known fluxes. The flux of 1E 2259+586 was measured on 30 days over 3.5 years, and that of 1RXS J1308+21 on 10 days over 1.5 years. Including observations in which the signal did not exceed 4σ, the mean flux densities are 35 ± 25 and 50 ± 20 mJy for 1E 2259+586 and 1RXS J1308+21, respectively (the 1σ rms dispersion of the flux density is given together with the mean). At the lower frequencies, we could estimate only upper limits for the flux densities of both pulsars: $S < 150$ mJy and $S < 200$ mJy at 87 MHz for 1E 2259+586 and 1RXS J1308+21, respectively.

We have already reported values for the period and period derivative of 1E 2259+586 and 1RXS J1308+21 derived for intervals of 1505 and 443 days, respectively, in [26]. We are currently accumulating data to refine these two parameters. We hope in the near future to determine the period and period derivative over a longer time interval and carry out a detailed analysis of the behavior of these two quantities in order to verify the presence of a period glitch, as was recently reported by Kaspi [27].

4. DISCUSSION

The table lists the main parameters of the radio emission from the two AXPs. Comparison with the X-ray data shows that the radio measurements both extend our knowledge about these objects and carry fundamentally new information. We have obtained more precise measurements of the period and period derivative for 1RXS J1308+21, detected strongly differing durations of the mean pulses, and derived independent estimates of the distances to both sources based on their dispersion measures. The existence of the radio emission itself represents a fundamentally new fact, which raises doubts about either the magnetar model or our understanding of radio emission in superstrong magnetic fields.

(a) Period and Period Derivative

The period and period derivative we have measured for the AXP 1E 2259+586 during MJD 51244–52749 [26] essentially coincide with the somewhat more precise X-ray values obtained during MJD 50356–52016: $P = 6.978948446(4)$ s and $\dot{P} = 4.8430(8) \times 10^{-13}$ s/s [18]. These measurements of the period and period derivative have been reduced to the same Julian date, MJD 51995.5827. Our estimates for 1RXS J1308+21 for MJD 52300–52743 are much more accurate ($P = 10.31431994$ s and $\dot{P} = 129.96$) than the data of Hambaryan *et al.* [19] obtained for MJD 50824–51719 and reduced to epoch MJD 51719.5.

(b) Distance and Luminosity

Distance estimates for the pulsar 1E 2259+586 (or rather for the supernova remnant CTB 109; the pulsar is almost at its center) in the literature are between 3.5 and 4.5 kpc (see, e.g., [16, 28]). Our measurements of the dispersion measure, 79 ± 4 pc/cm^3, yield a distance of 3.6 ± 0.7 kpc for the model electron density distribution in the Galaxy of [29]. It is interesting that the same distance to the remnant, 3.6 ± 0.4 kpc, was estimated in the first report of the detection of an X-ray source [16] toward the supernova remnant CTB 109, based on the surface brightness–angular size dependence at 408 MHz. Estimates of the distance to 1RXS J1308+21, or, more precisely, the star RBS 1223, obtained using several methods, lie in the broader interval from 0.1 to 1.5 kpc [19, 30]. Our dispersion measure (table) and the model for the Galaxy of [29] yield an estimated distance to the pulsar of $0.25^{+0.2}_{-0.1}$ kpc. This suggests that the pulsar is close to RBS 1223, as was also proposed by Reach *et al.* [30], who reported a distance estimate for the pulsar of 0.1–0.2 kpc.

The X-ray luminosity of 1E 2259+586 for a distance of 3.6 kpc ($\log L_x(\mathrm{erg/s}) = 34.9$ [3]) remains three orders of magnitude higher than the rate at which this star is losing rotational kinetic energy. The X-ray luminosity of 1RXS J1308+21 for a distance of 0.25 kpc is $L_x = 0.26 \times 10^{32}$ erg/s, rather than the value $L_x = 4.1 \times 10^{32}$ erg/s calculated for a distance of 1 kpc [19]. The rate of loss of rotational energy for this neutron star ($P = 10.32$ s and $\dot{P} = 130 \times 10^{-13}$ s/s) is $\dot{E} = 4.6 \times 10^{32}$ erg/s, which is close to the X-ray luminosity. Here, $\dot{E}$ is defined as

$$\dot{E} = \frac{4\pi^2 I \dot{P}}{P^3}, \qquad (1)$$

where I is the moment of inertia of the neutron star, which we have taken to be 10^{45} g cm^2.

To estimate the total radio luminosity, we must know the spectrum of the pulsar, or at least the spectral index. We can then use the formula [31]

$$L_R = \frac{\pi^3 l^3}{P} \int_0^\infty s(\nu) w(\nu) d\nu, \qquad (2)$$

where l is the distance to the pulsar, $s(\nu)$ is the flux density in a single pulse at frequency ν, and $W_{0.5}(\nu)$ is the pulse duration, which is taken to be constant. Using our flux-density measurement at 111 MHz, $S_{111} = 35$ mJy, and the upper limits at 600 MHz ($S_{600} < 2.3$ mJy [32]) and 1500 MHz ($S_{1500} < 0.05$ mJy [33]), we estimate the spectral index of 1E 2259+586 to be $\alpha > 2.5$.

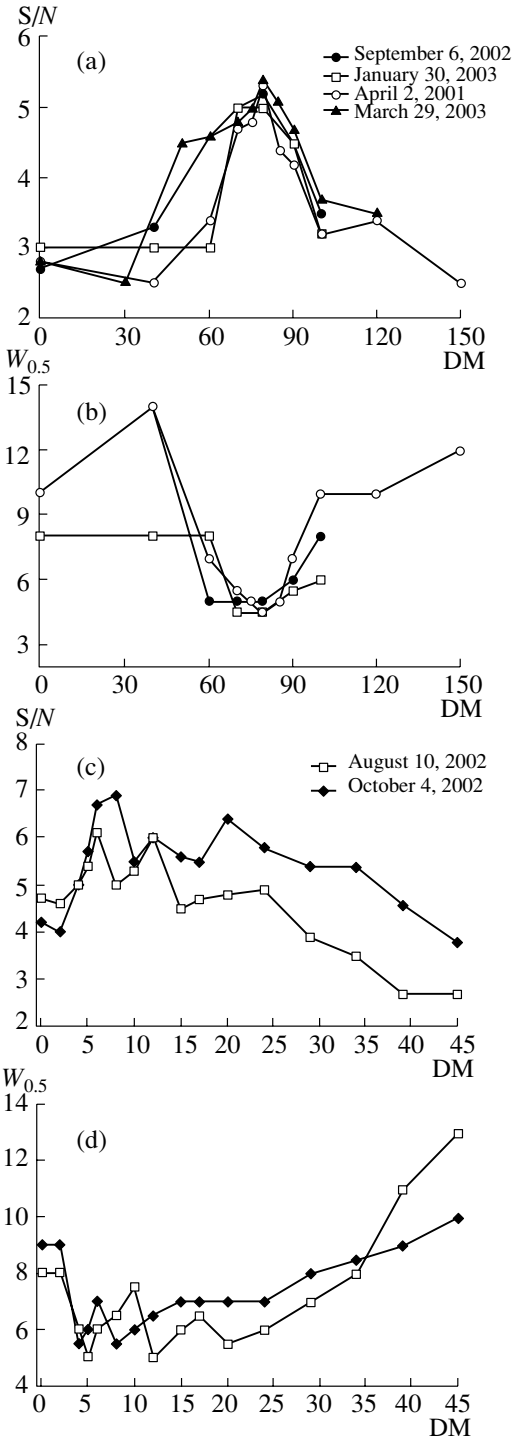

Fig. 7. Signal-to-noise ratio for the integrated pulse as a function of the dispersion measure (a, c); pulse duration at half-maximum $W_{0.5}$ (b, d) for the AXP 1E 2259+586 (a, b) and AXP candidate 1RXS J1308+21 (c, d).

There is only an upper limit for the flux density from the discrete source in 1RXS J1308+21 at 1.4 GHz $S_{1400} < 0.94$ mJy [34]; this yields the spectral index $\alpha > 1.7$ at 0.111–1.4 GHz. Given

Measured and calculated parameters of the two pulsars

Parameter	1E 2259+586	1RXS J1308+21
DM, pc/cm^3	79 ± 4	5.7 ± 0.5
S_{111}, mJy	35 ± 25	50 ± 20
w_{50} (111 MHz), ms	120 ± 20	140 ± 20
D, kpc	3.6 ± 0.2	0.25 ± 0.02
L_R, erg/s	$\sim 3 \times 10^{28}$	$\sim 3 \times 10^{26}$
L_x, erg/s	7.9×10^{34}	3×10^{31}
$\dot{E}$, erg/s	5.6×10^{31}	4.6×10^{32}
B, G	1.2×10^{14}	7.4×10^{14}
T, s	2.2×10^5	1.2×10^4

that the spectra of both pulsars are probably steep, we estimated the total radio luminosities of the two pulsars by adopting the value $\alpha = 2.5$; this yielded $L_R = 3 \times 10^{28}$ erg/s for 1E 2259+586 and $L_R = 3 \times 10^{26}$ erg/s for 1RXS J1308+21. Thus, these pulsars do not have extremely high luminosities in the radio. While 1E 2259+586 has a typical radio luminosity, 1RXS J1308+21 has one of the lowest radio luminosities, according to the luminosity distribution in [31].

Comparison of the radio and X-ray data suggests large differences in two observed parameters. First, the radio and X-ray pulse durations differ by a factor of 16–18, being 1.7 and 27% and 1.4 and 25% of the period durations at the pulse half-maxima for 1E 2259+586 and 1RXS J1308+21, respectively. Second, while an interpulse is observed in both the radio and X-ray for 1RXS J1308+21, 1E 2259+586 displays an interpulse only in the X-ray. In addition, the huge difference in the radio and X-ray luminosities is (five and six orders of magnitude) very important.

The table also lists the magnetic fields (B) and characteristic ages (T), calculated for a magnetodipole-radiation model:

$$B = \sqrt{\frac{3c^3 I P \dot{P}}{2\pi^2 R^6}} = 6.4 \times 10^{19} \sqrt{P\dot{P}}, \qquad (3)$$

where R is the radius of the neutron star, which we took to be 10^6 cm,

$$T = \frac{P}{(n-1)\dot{P}} \left[1 - \frac{P_0}{P}\right], \qquad (4)$$

where P_0 is the initial period of the pulsar rotation and n is the braking index. For $P_0 \ll P$ and $n = 3$, we obtain $T = P/2\dot{P}$. Note that the AXP candidate 1RXS J1308+21 has one of the largest magnetic fields and one of smallest characteristic ages among all pulsars, if the most commonly used magnetodipole-radiation model is applied.

5. CONCLUSIONS

(1) We have detected periodic pulsed emission from the AXP 1E 2259+586 and AXP candidate 1RXS J1308+211 in observations carried out on two radio telescopes of the Pushchino Radio Astronomy Observatory—the Large Phased Array (111 MHz) and the DKR-1000 (87 and 61 MHz). The pulsars' parameters are listed in the table.

(2) We have obtained independent estimates of the distances to both pulsars, which are within the intervals of distances determined using other methods.

(3) The main difference between the radio from the X-ray pulsed emission is that the integrated radio pulses of both objects are narrower. In addition, there is no appreciable radio interpulse for AXP 1E 2259+586.

(4) The presence of weak radio emission in two AXPs and one SGR [13], together with the recent detection of a radio pulsar (J1847–0130) with a long period ($P = 6.7$ s) and period derivative ($\dot{P} = 1.3 \times 10^{-12}$ s/s) [35], similar to those of AXPs, suggests the need to reexamine radio emission mechanisms in the magnetar model, or to devise other AXP and SGR models that do not involve superstrong magnetic fields.

ACKNOWLEDGMENTS

The authors are grateful to S.B. Popov for the suggestion to observe the AXP 1E 2259+586; to A.S. Aleksandrov, V.V. Ivanova, K.A. Lapaev and other employees of the Pushchino Radio Astronomy Observatory for help with the observations; to I.F. Malov and A.P. Glushak for useful discussions; and to L.B. Potapova for help with preparing the manuscript. This work was partially supported by the Russian Foundation for Basic Research (project nos. 03-02-16509 and 03-02-16522), the National Science Foundation (project no. 00-098685), INTAS (grant no. 00-00-849), the Program of the Presidium of the Russian Academy of Sciences "Nonstationary Processes in Astronomy," and the Federal Science and Technology Program in Astronomy.

REFERENCES

1. S. Mereghetti, *The Neutron Star – Black Hole Connection*, Ed. by C. Kouveliotou, J. Ventura, and E. van den Heuvel (Kluwer, Dordrecht, 2001), NATO Science Series C: Mathematical and Physical Sciences, Vol. 567, p. 351; astro-ph/9911252.

2. K. Hurley, AIP Conf. Proc. **526**, 763 (2000).
3. I. F. Malov, G. Z. Machabeli, and V. M. Malofeev, Astron. Zh. **80**, 258 (2003) [Astron. Rep. **47**, 232 (2003)].
4. A. I. Ibrahim, C. B. Markward, J. H. Swank, *et al.*, Astrophys. J. **609**, L21 (2004).
5. R. C. Duncan and C. Thompson, Astrophys. J. **392**, L9 (1992).
6. S. Mereghetti, in *Frontier Objects in Astrophysics and Particle Physics*, Ed. by F. Giovannelli and G. Mannocchi (Italian Physical Society, 2001), p. 531.
7. G. L. Israel, S. Covino, L. Stella, *et al.*, Astrophys. J. **518**, L107 (1999).
8. Ya. N. Istomin and B. V. Komberg, Astron. Zh. **77**, 852 (2000) [Astron. Rep. **44**, 754 (2000)].
9. D. Marsden, R. E. Lingenfelter, R. E. Rothschild, and J. C. Higdon, Astrophys. J. **550**, 397 (2001).
10. A. Dar and A. De Rujula, *Results and Perspectives in Particle Physics*, Ed. by M. Greco (2000), Vol. XVII, p. 13; astro-ph/0002014.
11. M. G. Baring and A. K. Harding, Astrophys. J. **547**, 929 (2001).
12. M. G. Baring and A. K. Harding, Astrophys. J. **507**, L55 (1998).
13. Yu. P. Shitov, V. D. Pugachev, and S. M. Kutuzov, Astron. Soc. Pac. Conf. Ser. **202**, 685 (2000).
14. V. M. Malofeev and O. I. Malov, astro-ph/0106435.
15. B. Zhang, Astrophys. J. **562**, L59 (2001).
16. P. C. Gregory and G. G. Fahlman, Nature **287**, 805 (1980).
17. G. G. Fahlman and P. C. Gregory, Nature **293**, 202 (1981).
18. F. P. Gavriil and V. M. Kaspi, Astrophys. J. **567**, 1067 (2002).
19. V. Hambaryan, G. Hasinger, A. D. Schwope, and N. S. Schulz, Astron. Astrophys. **381**, 98 (2002).
20. F. Haberl, A. D. Schwope, V. Hambaryan, *et al.*, Astron. Astrophys. **409**, L19 (2003).
21. S. A. Tyul'bashev and O. I. Malov, Astron. Zh. **77**, 737 (2000) [Astron. Rep. **44**, 654 (2000)].
22. V. M. Malofeev, O. I. Malov, and N. V. Shchegoleva, Astron. Zh. **77**, 499 (2000).
23. V. M. Malofeev and O. I. Malov, Nature **389**, 697 (1997).
24. V. M. Malofeev and O. I. Malov, *Conf. on Physics of Neutron Stars, St. Petersburg, 2001*, p. 31.
25. V. M. Malofeev and O. I. Malov, *Proc. of Conf. on Chemical and Dynamic Evolution of Stars and Galaxies, Odessa, Ukraine, 2002*, p. 8.
26. V. M. Malofeev, O. I. Malov, and D. A. Teplykh, *IAU Symp. No. 218: Young Neutron Stars and Their Environments*, Ed. by F. Camilo and B. M. Gaensler (Astron. Soc. Pacif., San Francisco, 2004), p. 261.
27. V. M. Kaspi, *IAU Symp. No. 218: Young Neutron Stars and Their Environments*, Ed. by F. Camilo and B. M. Gaensler (Astron. Soc. Pacif., San Francisco, 2004), p. 231.
28. V. A. Hughes, R. M. Harten, C. H. Costain, *et al.*, Astrophys. J. **283**, 147 (1984).
29. J. H. Taylor and J. M. Cordes, Astrophys. J. **411**, 674 (1993).
30. W. T. Reach, C. Helles, and B. Koo, Astrophys. J. **412**, 127 (1993).
31. O. I. Malov, V. M. Malofeev, and D. S. Sen'e, Astron. Zh. **71**, 762 (1994) [Astron. Rep. **38**, 677 (1994)].
32. D. R. Lorimer, A. G. Lyne, and F. Camilo, Astron. Astrophys. **331**, 1002 (1998).
33. M. J. Coe, Z. R. Jones, and H. Lehto, Mon. Not. R. Astron. Soc. **270**, 179 (1994).
34. R. L. White, R. H. Becker, D. J. Helfand, and M. D. Gregg, Astrophys. J. **475**, 479 (1997).
35. M. A. McLaughlin, I. H. Stairs, V. M. Kaspi, *et al.*, Astrophys. J. **591**, L135 (2003).

Translated by G. Rudnitskii

Astronomy Reports, Vol. 49, No. 3, 2005, pp. 250–257. Translated from Astronomicheskiĭ Zhurnal, Vol. 82, No. 3, 2005, pp. 281–288.

The Asymmetry Coefficient for Interstellar Scintillation of Extragalactic Radio Sources

V. I. Shishov, T. V. Smirnova, and S. A. Tyul'bashev

Pushchino Radio Astronomy Observatory, Astro Space Center, Lebedev Physical Institute, Pushchino, Russia

Received June 23, 2004; in final form, September 20, 2004

Abstract—Comparing the asymmetry coefficients γ and scintillation indices m for observed time variations of the intensity of the radiation of extragalactic sources and the predictions of theoretical models is a good test of the nature of the observed variations. Such comparisons can be used to determine whether flux density variations are due to scintillation in the interstellar medium or are intrinsic to the source. In the former case, they can be used to estimate the fraction of the total flux contributed by the compact component (core) whose flux density variations are caused by inhomogeneities in the interstellar plasma. Results for the radio sources PKS 0405−385, B0917+624, PKS 1257−336, and J1819+3845 demonstrate that the scintillating component in these objects makes up from 50 to 100% of the total flux, and that the intrinsic angular sizes of the sources at 5 GHz are 10−40 microarcseconds. The characteristics of the medium giving rise to the scintillations are presented. © *2005 Pleiades Publishing, Inc.*

1. INTRODUCTION

Two alternative hypotheses aimed at explaining the phenomenon of rapid variability of the fluxes of extragalactic sources at centimeter wavelengths on characteristic time scales of less than a day are discussed in the literature: (1) intrinsic variability associated with the source and (2) variability due to interstellar scintillation (see, for example, [1–4]). Since the velocity of the Earth relative to the interstellar medium displays seasonal variations with an amplitude of several tens of kilometers, we should expect variations in the variability time scale over the course of a year in the case of scintillations. Indeed, such seasonal variations have been observed for several sources, with the variation time scale increasing appreciably in the period from August to October [2, 5], in agreement with the decrease in the velocity of the Earth relative to the interstellar medium in this period. This demonstrates the interstellar origin of the variability of these sources.

However, for the majority of radio sources, there is no conclusive proof that fluctuations in their fluxes are due to interstellar scintillation. In addition, in the case of rapid intrinsic variability, the angular size of the source must be small enough that it should inevitably scintillate on inhomogeneities in the interstellar plasma at centimeter wavelengths. For example, if a source located at a distance of 10^{28} cm displays variability with a characteristic time scale of the order of $t = 1$ day, its linear size should be no larger than about $l = 3 \times 10^{15}$ cm, so that its angular size should be no larger than about $\varphi = 0.1$ microarcsecond (0.1 μas). This is appreciably smaller than the angular size of the first Fresnel zone for the interstellar medium. Consequently, the source will be pointlike from the point of view of interstellar scintillations, and should accordingly scintillate at centimeter wavelengths, as pulsars do. Therefore, it is more correct to consider the following alternatives: (1) intrinsic variability of the source combined with interstellar scintillation and (2) variability due only to interstellar scintillation. For sources in which the first scenario is realized, the problem of distinguishing intrinsic variations from variations due to interstellar scintillation is extremely important. We propose here a qualitative test to verify the nature of observed flux variations by measuring the asymmetry coefficient of the flux fluctuation distribution function.

2. THE ASYMMETRY COEFFICIENT

When analyzing scintillations of extragalactic radio sources on inhomogeneities of the interstellar plasma, the most important measured quantity is the scintillation index:

$$m^2 = \frac{\langle (I - \langle I \rangle)^2 \rangle}{\langle I \rangle^2}, \qquad (1)$$

where I is the measured flux and $\langle I \rangle$ is its mean value. However, extragalactic sources have complex structures, consisting of a compact scintillating component and a nonscintillating extended component. Only the compact component with angular size on

1063-7729/05/4903-0250$26.00

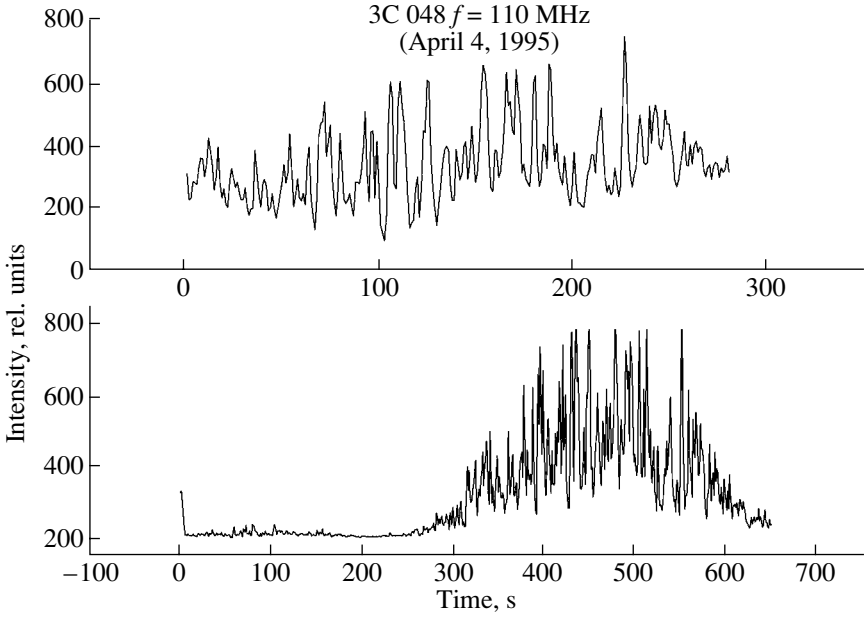

Fig. 1. Original recording of the intensity of the source 3C 48 as a function of time at 110 MHz (lower), and the same recording after eliminating the slow component (the initial data were averaged over 10 points) (upper).

the order of or smaller than the first Fresnel zone (the "core") will scintillate on inhomogeneities of the interstellar plasma. Consequently, without knowing the flux of the scintillating component I_0, it is not possible to determine the corresponding scintillation index:

$$m_0^2 = \frac{\langle (I - \langle I \rangle)^2 \rangle}{\langle I_0 \rangle^2}. \quad (2)$$

Only the quantity m_0 presents physical interest. In [6–9], it was proposed to overcome these difficulties associated with observations of scintillating radio sources using measurements of the asymmetry coefficient of the flux fluctuation distribution:

$$\gamma = \frac{\langle (I - \langle I \rangle)^3 \rangle}{[\langle (I - \langle I \rangle)^2 \rangle]^{3/2}} = \frac{M_3}{M_2^{3/2}}. \quad (3)$$

Here, M_3 and M_2 are the third and second central moments of the flux fluctuation distribution. Theoretical relations between γ and m_0 are known for a number of cases. For example, in the case of weak scintillations of a point source in the Fraunhofer zone relative to the outer scale of the turbulence (i.e., the characteristic size of the large-scale inhomogeneities), the flux fluctuation distribution follows a Rice–Nakagama law [10, 11], and the asymmetry coefficient is given by the relation

$$\gamma = \frac{3}{2} m_0. \quad (4)$$

In the case of weak scintillations of a point source in the Fresnel zone relative to the inner turbulence scale (i.e., the characteristic size of small inhomogeneities), this distribution follows a logarithmic normal law [12], and

$$\gamma = 3m_0. \quad (5)$$

In the case of a power-law spectrum, a linear dependence between γ and m_0 should be preserved:

$$\gamma = Am_0, \quad (6)$$

where the coefficient A depends on the form of the turbulence spectrum.

This suggestion is supported by the results of Hill *et al.* [13, 14], who carried out numerical computations of flux fluctuation distribution functions and determined the second and third moments of the flux fluctuations for the case of inhomogeneities in the refraction index with a Kolmogorov spectrum and various inner turbulence scales. These computations yield for a purely power-law spectrum $A = 2.78$, and for a Kolmogorov spectrum with inner turbulence scale l equal to the scale of the first Fresnel zone r_{Fr} ($l/r_{\mathrm{Fr}} = 1$) $A = 2.86$. Thus, the coefficient A increases and approaches the value three as the inner scale for the turbulence spectrum increases. We can see that, in the case of a Kolmogorov spectrum, A is close to three, and we can use relation (5) to describe the relation between γ and m_0. The computations indicate that (5) is valid up to values of m_0 approaching unity from the weak (unsaturated) scintillation regime.

We experimentally verified relation (6) using observations of refractive interstellar scintillations of

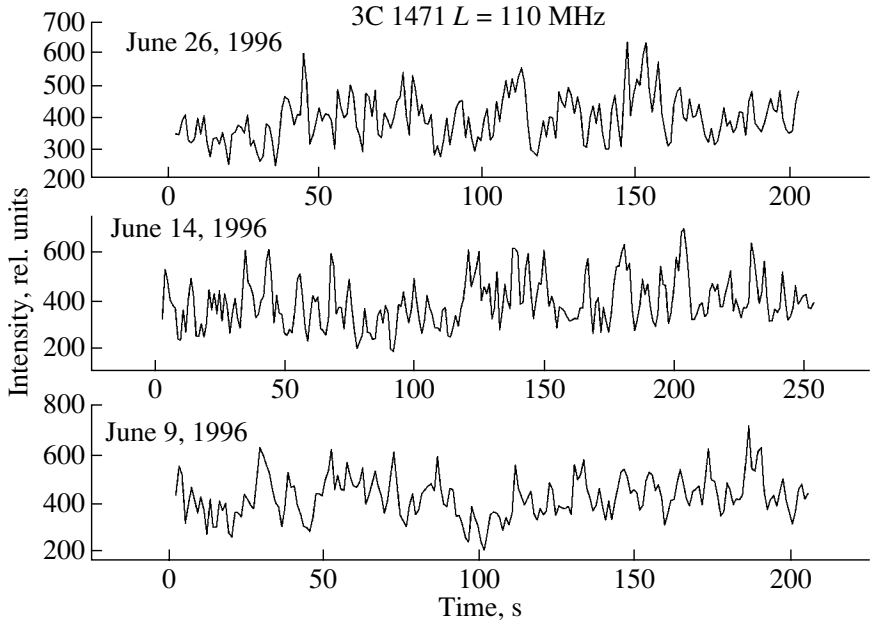

Fig. 2. Recording of interplanetary scintillations of 3C 147 at 110 MHz over three days of observations.

pulsars at 610 MHz [15], observations of weak scintillations of the pulsar 1642–03 at 5 GHz [16], and observations of interplanetary scintillations of the radio sources 3C 48, 3C 119, and 3C 147 carried out at 110 MHz using the Large Phased Array of the Pushchino Radio Astronomy Observatory. In the first set of observations, the intrinsic variations of the pulsar intensities, with time scales of several seconds, and variations due to diffractive scintillations, with time scales of several minutes, were removed by averaging the intensity over time intervals of about one hour.

Examples of our recordings of the flux variations observed for 3C 48 and 3C 147 due to interplanetary scintillations are shown in Figs. 1 and 2. We used a receiver with a bandwidth of 600 kHz and a time constant of 0.5 s for these observations. The data were recorded on disk for subsequent reduction at a rate of 10 Hz. Figure 1 shows an original recording for 3C 48 together with its noise level (lower), as well as the same recording after filtering out the slow component due to the antenna beam (upper). Rapid fluctuations of the flux are associated with the passage of the radiation through the turbulent interplanetary plasma. Figure 2 shows the flux variations for 3C 147 observed over three days.

Examples of recordings of flux variations of pulsars due to refractive scintillations at 610 MHz are presented in [15]. The results of using these observations to determine the asymmetry coefficient and scintillation index are shown in Fig. 3. Refractive interstellar scintillations of a pulsar can be considered to be weak scintillations of a source whose angular size is comparable to the scattering angle Θ_0, which is determined by scattering of the radiation on small-scale (diffractive) inhomogeneities. The effective size of the inhomogeneities responsible for the refractive scintillations is the radius of the scattering disk, $L\theta_0$, where L is the effective distance to the turbulent layer. This size is much larger than the first Fresnel zone r_{Fr}, so that, in this case, the asymmetry coefficient is described by relation (5). The scatter of the points corresponds to the real statistical errors of the measurements. The turbulence spectrum for the interplanetary plasma is a power law over a wide range of scales, and the spectral index for the three-dimensional spatial spectrum is close to that for a Kolmogorov spectrum, $n = 11/3$ [17].

In contrast to pulsars, which are point sources, the extragalactic objects we used in our analysis consist of a compact component (core) that scintillates on inhomogeneities in the interplanetary plasma and a large-scale halo that does not scintillate. Of course, extragalactic sources can have more complex, multi-component structures, but for our purposes it is only important that we divide the source into scintillating and nonscintillating components. To make the translation from m to m_0, we used ratios of the fluxes of compact and extended components presented in [18]: $m/m_0 = 0.7$ for 3C 48 and $m/m_0 = 0.5$ for 3C 119. We adopted the ratio $m/m_0 = 1$ for 3C 147. Figure 3 presents the values of m_0 that were used.

Figure 3 shows that the collected data obtained for various media and sources with various sizes are in good agreement with relation (5). The scatter of the

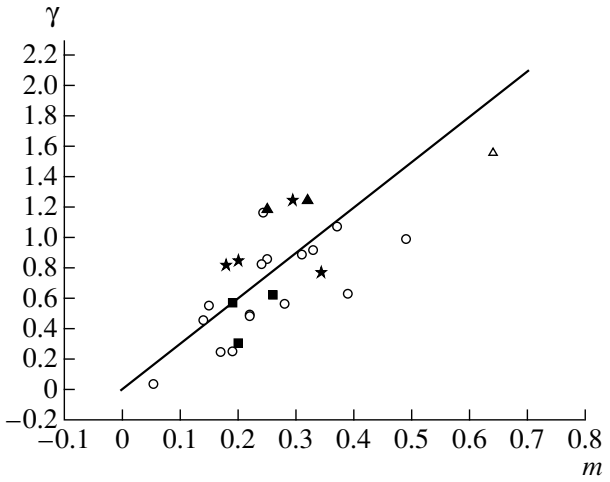

Fig. 3. Dependence of the asymmetry coefficient γ on the scintillation index m. The circles show the data derived from refractive scintillations of pulsars, the hollow triangle show data derived from variations of PSR 1642−03 at 5 GHz (weak scintillation). The stars, filled triangles and squares show the data derived from interplanetary scintillations of 3C 48, 3C 119, and 3C 147, respectively. The line corresponds to the theoretical relation $\gamma = 3m_0$.

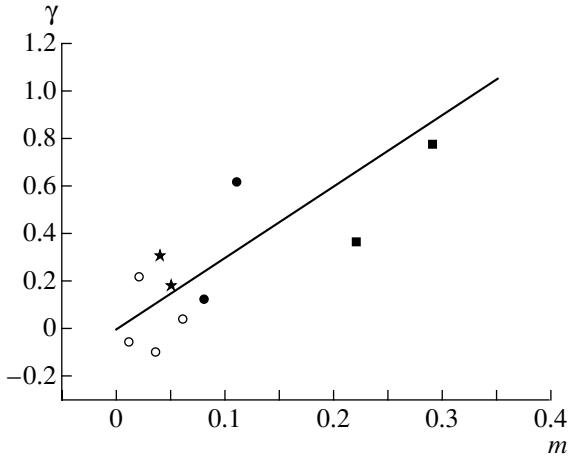

Fig. 4. Dependence of the asymmetry coeffient γ on the scintillation index m for variations of the extragalactic sources. Shown are the data for PKS 0405−385 (filled circles), B0917+624 (hollow circles), J1819+3845 (squares), and PKS 1257−326 (stars). The line corresponds to the theoretical relation $\gamma = 3m_0$ [Eq. (5)].

points about the theoretical curve is only 30%, and is primarily determined by the statistical errors in γ. Thus, γ is a measurable quantity that can be used to test the hypothesis that interstellar scintillations are the origin of rapid variations of extragalactic radio sources.

3. ASYMMETRY COEFFICIENTS OF A NUMBER OF RAPIDLY VARIABLE EXTRAGALACTIC RADIO SOURCES

We used the observed flux variations of the well-known compact radio sources PKS 0405−385, B0917+624, PKS 1257−326, and J1819+3845 to determine the scintillation indices m and asymmetry coefficients γ for these observations. The resulting values of γ are listed in the table, which also gives the scintillation indices m and characteristic scintillation times t_0, with references. The uncertainties in m are 10−20%. The characteristic scintillation time was defined as the radius of the autocorrelation function at the half-maximum level.

The dependence of the asymmetry coefficient γ on the scintillation index m is shown in Fig. 4, where the data for B0917+624 are shown by the hollow circles, for PKS 1257−326 by the stars, for PKS 0404−385 by the filled circles, and for J1819+3845 by the filled squares. The uncertainties in γ associated with the averaging are roughly $\delta\gamma \cong 0.2$. We can see that the collected points show a well-defined linear relation between γ and m, which corresponds to the theoretical relation (5) with $m = m_0$; i.e., the case when the flux of the scintillating component comprises a large fraction of the total flux of the source.

Before turning to a discussion of the data for each source, we will first present a number of expressions relating the parameters of the scintillations and those of the medium and source. Data for interstellar scintillations of pulsars and extragalactic sources shows that the scintillations are weak at centimeter wavelengths and, in the case of sources with small angular sizes, the main contribution to the scintillations is made by inhomogeneities with sizes comparable to the first Fresnel zone, and the spatial scale for the scintillations is comparable to the Fresnel scale:

$$b \cong r_{\mathrm{Fr}} = \left(\frac{k}{L}\right)^{-1/2}, \qquad (7)$$

where L is the effective distance from the observer to the turbulent layer that is responsible for the scintillations, $k = 2\pi/\lambda$, and λ is the wavelength of the observations. If the medium is statistically uniformly distributed between the source and observer, L corresponds to the distance between the source and observer, R. If the turbulent medium is concentrated in a fairly narrow layer with thickness $\Delta L \ll R$, then L is the smaller of the distance from the observer to the layer or the distance from the layer to the source. Accordingly, the characteristic scintillation time will be

$$t = \frac{b}{V} = \frac{r_{\mathrm{Fr}}}{V} = \left(\frac{L}{k}\right)^{1/2} \Big/ V, \qquad (8)$$

Flux variations for well-known compact radio sources

Source	Observing frequency, GHz	m	t_0, h	γ	Ref.
PKS 0405−385	8.64	0.08	0.41	+0.12	[19]
	4.8	0.11	0.55	+0.62	
	2.38	0.093	1.6		
	1.38	0.063	2.6		
B0917+624	15.0	0.01	3	−0.06	[3, 20]
	8.3	0.02	2.4	+0.22	
	5.0	0.035	7.2	−0.10	
	2.7	0.06	20	+0.04	
PKS 1257−326	8.6	0.05	0.27	+0.18	[5]
	4.8	0.04	0.33	+0.31	
J1819+3845	8.5	0.22	0.5	+0.38	[22]
	4.8	0.29	0.53	+0.78	[2, 21, 22]
	2.2	0.24			[22]
	1.3	0.13	3.5		[22]

where V is the velocity of the Earth relative to the interstellar medium.

The scintillation index for a point source should be

$$m_{0,0} = \left(\frac{f_{cr}}{f}\right)^{\beta}, \qquad \beta = \frac{n+2}{4}. \tag{9}$$

Here, n is the spectral index of the turbulence spectrum (for a Kolmogorov spectrum, $n = 11/3$ and $\beta = 1.4$) and $f_{cr} \approx 3$ GHz is the critical frequency for the transition from the weak to the strong scintillation regime [23].

Relations (8) and (9) determine the parameters of scintillations of a source with small angular size. If the angular size of the source φ_0 is larger than the Fresnel angle,

$$\varphi_0 > 2\varphi_{\rm Fr} = \frac{2}{kr_{\rm Fr}} = \left(\frac{2}{kL}\right)^{1/2}, \tag{10}$$

the scintillation index in the weak scintillation regime is given by the relation

$$m_0 \cong m_{0,0}\left(\frac{2\varphi_{\rm Fr}}{\varphi_0}\right)^{\alpha}, \qquad \alpha = \frac{6-n}{2} = \frac{7}{6}, \tag{11}$$

where $m_{0,0}$ is given by (9) and the characteristic scintillation time is given by

$$t_0 \cong \frac{L\varphi_0}{2V}. \tag{12}$$

When estimating the influence of the angular size of the source on the scintillation parameters, we should bear in mind that the characteristic spatial and time scales for the scintillations are determined by the correlation radius, and correspond to the characteristic radius of inhomogeneities in the spatial distribution of the intensity fluctuations, while the angular size of the source is determined by the source brightness distribution. This is the reason for the additional factor of two in relations (10)–(12).

Our estimates of $\varphi_{\rm Fr}$ depend appreciably on the effective distance L to the turbulent layer. Observations show that, at sufficiently high Galactic latitudes, scintillations of radio sources are determined by two components of the interstellar medium. The first (component A) is localized between the spiral arms, and is fairly uniformly distributed in a thin layer with a thickness of about 1 kpc [24]. The second (component C) forms a layer of turbulent plasma with an enhanced level of electron-density fluctuations located at a distance of about 10 pc from the Sun [1, 2, 4]. The relative contributions of these components can vary with direction and angular size of the source. If the main contribution to the scintillations is made by the first component, then $\varphi_{\rm Fr,1} \cong 3.5$ μas at 5 GHz if $L = 1$ kpc. If the main contribution is made by the second component, then $\varphi_{\rm Fr,2} \cong 35$ μas at 5 GHz if $L = 10$ pc. For example, observations of scintillations of pulsars, whose angular sizes are much smaller than $\varphi_{\rm Fr,1}$, show that the main effect is due to inhomogeneities of the first component of the interstellar medium. If the angular size of the source is much

larger than $\varphi_{\mathrm{Fr},1}$, the main effect will be due to inhomogeneities of the C component of the interstellar medium. We discuss the data for each source in detail below.

PKS 0405−385. The observed flux variations can be understood as scintillations on inhomogeneities of the local interstellar medium; i.e., component C. The values $m \cong 0.11$ and $\gamma \cong 0.62$ at 4.8 GHz suggest that the scintillating core contains roughly 50% of the total flux. The scintillation index for the scintillating component is $m_0 \cong \gamma/3 \cong 0.2$, so that the scintillations are weak. The characteristic scintillation time $t_0 \cong 30$ min at 4.8 GHz [19] corresponds to the size of the first Fresnel zone [Eq. (8)] for a distance $L \cong 10$ pc and a velocity of the observer of $V = 30$ km/s. The scintillation index decreases at 2.4 and 1.4 GHz, and the characteristic scintillation time grows rapidly with decreasing radio frequency. This dependence can be understood as being due to the increase in the apparent angular size of the source, which is roughly proportional to the square of the wavelength. In turn, the apparent angular size of the source could be the result of scattering on inhomogeneities of the interstellar plasma in a layer that is further from the observer. Studies of scattering of pulsars have shown that turbulent interstellar plasma with a characteristic thickness of about 1 kpc is observed in all directions from the Sun [24]. The characteristic scattering angle in the direction of PKS 0405−385 should be $\theta_0 \cong 90$ μas at 2.38 GHz.

B0917+624. A comparison of the values of m and γ at four frequencies indicates that the scintillating component comprises close to 100% of the total flux. The small value of the scintillation index is due, not to the flux of the scintillating component comprising a small fraction of the total, but to the large angular size of the source. With increasing wavelength λ, we observe an approximately linear growth in the scintillation index, $m \propto \lambda$, and in the scintillation time, $t_0 \propto \lambda$. These dependences can be understood only if the angular size of the source appreciably influences the scintillation parameters, with the apparent angular size of the source being roughly proportional to the wavelength: $\varphi_0 \propto \lambda$. This dependence excludes the interstellar medium as the origin of the apparent angular size of the source, so that this must be the intrinsic angular size. Estimates of this size depend on the distance to the effective center of the turbulent layer. We used observations of scintillations of the pulsar B0809+74, which is located close to B0917+624 in the sky, to estimate the parameters of the turbulent medium. This pulsar is located 433 pc from the Sun and has a velocity $V = 102$ km/s [25]. The scintillation parameters presented in [26] correspond to scintillation in a turbulent medium that is uniformly distributed between the source and observer. Using the scintillation parameters for B0809+74 obtained at 933 MHz, $m = 0.8$ and $t_0 = 2$ h, together with Eqs. (11) and (12), and using the fact that the turbulence spectrum is Kolmogorov, we obtain $m = 0.08$ and $t_0 = 50$ min at 4.8 GHz. Taking into account the fact that the pulsar scintillations correspond to the case of a spherical wave, while the scintillations of the extragalactic source correspond to the case of a plane wave, and also the fact that the velocity of the observer is roughly a factor of three lower than the velocity of the pulsar, we find for a pointlike extragalactic source $m = 0.11$ and $t_0 = 2.5$ h. The inferred scintillation parameters of B0917+624 at 5 GHz correspond to those for an extragalactic radio source with an angular size of $\varphi \cong 10$ μas (roughly a factor of three larger than the size of the first Fresnel zone).

PKS 1257−326. The characteristic time scale for the flux fluctuations shows seasonal variations, providing a direct demonstration that they have an interstellar origin [19]. The observed fluctuations can be understood as scintillations in the local interstellar medium. The values $m \cong 0.04$ and $\gamma \cong 0.31$ at 4.8 GHz suggest that the scintillating core contains about 40% of the total flux. The scintillation index for the scintillating component is $m_0 \cong \gamma/3 \cong 0.10$, so that the scintillations are weak. The characteristic scintillation time $t_0 \cong 20$ min [5], corresponds to the size of the first Fresnel zone for a distance of $L \cong 5$ pc and a velocity of the observer $V = 30$ km/s. The values $m \cong 0.05$ and $\gamma \cong 0.18$ indicate that the scintillating component comprises 100% of the total flux at 8.6 GHz, with the scintillation index being half that for the scintillating component at 4.8 GHz. This corresponds to (11) within the errors in the measured parameters [according to (11), the decrease in the scintillation index should be a factor of 2.3].

J1819+3845. The characteristic time scale for the fluctuations shows seasonal variations, providing a direct demonstration that they have an interstellar origin [2]. The fluctuations can be understood as scintillations on inhomogeneities of the local interstellar medium (component C). The values $m \cong 0.29$ and $\gamma \cong 0.78$ at 4.8 GHz suggest that the scintillating core contains roughly 90% of the total flux. The scintillation index for the compact component is $m_0 \cong \gamma/3 \cong 0.26$, so that the scintillations are weak. The characteristic scintillation time, $t_0 \cong 30$ min [2], corresponds to the size of the first Fresnel zone for a distance of $L \cong 10$ pc and a velocity of the observer $V = 30$ km/s. The values $m \cong 0.22$ and $\gamma \cong 0.38$ at 8.5 GHz can be understood as scintillations if the scintillating component contains about 60% of the total flux. The scintillation index begins to fall off at 2.2 and 1.3 GHz, and the characteristic

scintillation time rapidly grows with decreasing frequency. As for PKS 0405−385, this dependence can be understood as a consequence of an increase in the angular size roughly in proportion to the square of the wavelength. The angular size is probably due to scattering on inhomogeneities in the interstellar plasma in a layer with a thickness of about 1 kpc. The characteristic scattering angle in this medium in the direction of J1819+3845 should be $\theta_0 \cong 100$ μas at 2.2 GHz.

4. DISCUSSION

Thus, our test of the origin of flux variations of several rapidly variable extragalactic sources based on comparisons between the asymmetry coefficient γ and the values predicted by scintillation theory demonstrates that scintillation is the main mechanism giving rise to the flux variations at frequencies of 8.6 GHz and lower. Comparisons of the measured scintillation indices and asymmetry coefficients indicate that the scintillating components comprise from 50 to 100% of the total flux of the sources, so that the measured scintillation indices are close to those for a one-component compact source.

The scintillation parameters of the sources correspond to two types of media: medium I has a characteristic thickness of about 1 kpc, while medium II has a characteristic thickness of about 10 pc. The quasar B0917+624 scintillates in medium I, and indeed, this medium is responsible for most of the scintillation and scattering of the radio emission of pulsars [23]. The angular size of the source grows linearly with growth in the wavelength.

The scintillations of the remaining three sources occur in medium II, which is closer to the observer and has a characteristic thickness of 10 pc. The parameters of this medium have been estimated in [1, 2, 4, 5]. At 5 GHz and higher, the sources have angular sizes comparable to or smaller than the first Fresnel zone, $\varphi_0 \leq 40$ μas. The scintillation index at nearby low frequencies decreases with increasing wavelength, while the characteristic scintillation time grows roughly in proportion to the square of the wavelength. This can be understood if radiation that has been scattered in medium I is then incident on medium II; the characteristic scattering angle should be comparable to the angular size of the first Fresnel zone (medium II) at 5 GHz. In this case, scintillation in medium I should be suppressed by the angular size of the source, which is a factor of five to ten larger than the angular size of the first Fresnel zone for medium I. Overall, a crude estimate of the intrinsic angular sizes of the sources at 5 GHz is $10 \leq \varphi \leq 40$ μas. More accurate estimates of these angular sizes require analysis of the temporal structure of the intensity fluctuations near time shifts of 3−10 h.

We have shown that analyzing the variations of the fluxes of rapidly variable extragalactic sources incorporating calculations of the asymmetry coefficient provides an effective method for testing the nature of this variability and estimating the angular sizes of the sources. The variability in the four sources we have studied here can be explained as scintillations occurring in two media: a more extended medium with a thickness of about 1 kpc and the local interstellar medium near the Sun with a thickness of ∼10 pc. The scintillations occurring in the extended medium are relatively slow (with characteristic time scales of roughly several hours), and can be used to estimate the angular sizes of the sources with resolutions of about 3 μas. The scintillations occurring in the local interstellar medium are more rapid (with characteristic time scales of fractions of an hour), and can be used to estimate the angular sizes of sources with the poorer resolution of about 30 μas. In light of the results obtained, the observed variability of the sources studied can be explained without invoking their intrinsic variability.

ACKNOWLEDGMENTS

This work was supported by the Russian Foundation for Basic Research (project nos. 03-02-16509 and 03-02-16522), the INTAS Foundation (grant no. 00-849), the National Science Foundation (grant no. AST 0098685), the Federal Science and Technology Program in Astronomy, and the program of the Physical Sciences Branch of the Russian Academy of Sciences "Extended Objects in the Universe."

REFERENCES

1. D. L. Jauncey, L. Kedziora-Chudczer, J. E. J. Lovell, *et al.*, Astrophys. Space Sci. **278**, 93 (2001).
2. J. Dennett-Thorpe and A. G. de Bruyn, Astrophys. Space Sci. **278**, 101 (2001).
3. S. J. Qian, A. Kraus, T. P. Krichbaum, *et al.*, Astrophys. Space Sci. **278**, 119 (2001).
4. B. J. Rickett, Astrophys. Space Sci. **278**, 129 (2001).
5. H. E. Bignall, D. L. Jauncey, J. E. J. Lovell, *et al.*, Astrophys. J. **585**, 653 (2003).
6. G. Bourgois, Astron. Astrophys. **21**, 33 (1972).
7. G. Bourgois and G. Cheynet, Astron. Astrophys. **21**, 26 (1972).
8. J. W. Armstrong, W. A. Coles, and B. J. Rickett, J. Geophys. Res. **77**, 2739 (1972).
9. V. I. Shishov and A. V. Pynzar', Izv. Vyssh. Uchebn. Zaved., Radiofiz. **18**, 506 (1975).
10. M. Nakagami, *Statistical Methods in Radio Wave Propagation*, Ed. by W. C. Hoffman (Pergamon, New York, 1960), p. 3.
11. R. P. Mercier, Proc. Cambridge Philos. Soc. **58**, 382 (1962).

12. V. I. Tatarskiĭ, *The Effects of the Turbulent Atmosphere on Wave Propagation* (Nauka, Moscow, 1967; Israel Program for Scientific Translations, Jerusalem, 1971).
13. R. J. Hill, R. G. Frehlich, and W. D. Otto, NOAA Tech. Memo. ETL-274 (NOAA Enviromental Research Laboratories, Boulder, 1996).
14. R. J. Hill and R. G. Frehlich, J. Opt. Soc. Am. A **14**, 1530 (1997).
15. D. R. Stinebring, T. V. Smirnova, T. H. Hankins, *et al.*, Astrophys. J. **539**, 300 (2000).
16. T. V. Smirnova, V. I. Shishov, W. Sieber, *et al.*, Astron. Astrophys (submitted).
17. C.-Y. Tu and E. Marsh, Space Sci. Rev. **73**, 1 (1995).
18. S. A. Tyul'bashev and P. A. Chernikov, Astron. Astrophys. **373**, 381 (2001).
19. B. J. Rickett, L. Kedziora-Chudczer, and D. L. Jauncey, Astrophys. J. **581**, 103 (2002).
20. A. Quirrenbach, A. Kraus, A. Witzel, *et al.*, Astron. Astrophys., Suppl. Ser. **141**, 221 (2000).
21. A. G. de Bruyn and J. Dennett-Thorpe, Astrophys. Space Sci. **278**, 139 (2001).
22. J. Dennett-Thorpe and A. G. de Bruyn, Astrophys. J. Lett. **529**, L65 (2000).
23. T. V. Smirnova and V. I. Shishov, Astron. Zh. **77**, 483 (2000) [Astron. Rep. **44**, 421 (2000)].
24. A. V. Pynzar' and V. I. Shishov, Astron. Zh. **74**, 663 (1997) [Astron. Rep. **41**, 586 (1997)].
25. W. F. Brisken, J. M. Benson, W. M. Cross, and S. E. Torsett, Astrophys. J. **571**, 906 (2002).
26. B. J. Rickett, Wm. A. Coles, and J. Markkanen, Astrophys. J. **533**, 304 (2000).

Translated by D. Gabuzda